FINAL REPORT FOR NASA GRANT NAG-1-1503

CRACK GROWTH PREDICTION METHODOLOGY FOR MULTI-SITE DAMAGE: LAYERED ANALYSIS AND GROWTH DURING PLASTICITY

by

MARK ANTHONY JAMES

RESEARCH SUPERVISED BY:
Daniel V. Swenson

Department of Mechanical and Nuclear Engineering
College of Engineering

KANSAS STATE UNIVERSITY
Manhattan, Kansas 66506
USA

ABSTRACT

A finite element program has been developed to perform quasi-static, elastic-plastic crack growth simulations. The model provides a general framework for mixed-mode I/II elastic-plastic fracture analysis using small strain assumptions and plane stress, plane strain, and axisymmetric finite elements.

Cracks are modeled explicitly in the mesh. As the cracks propagate, automatic remeshing algorithms delete the mesh local to the crack tip, extend the crack, and build a new mesh around the new tip. State variable mapping algorithms transfer stresses and displacements from the old mesh to the new mesh. The von Mises material model is implemented in the context of a non-linear Newton solution scheme. The fracture criterion is the critical crack tip opening displacement, and crack direction is predicted by the maximum tensile stress criterion at the crack tip. The implementation can accommodate multiple curving and interacting cracks. An additional fracture algorithm based on nodal release can be used to simulate fracture along a horizontal plane of symmetry. A core of plane strain elements can be used with the nodal release algorithm to simulate the triaxial state of stress near the crack tip.

Verification and validation studies compare analysis results with experimental data and published three-dimensional analysis results. Fracture predictions using nodal release for compact tension, middle-crack tension, and multi-site damage test specimens produced accurate results for residual strength and link-up loads. Curving crack predictions using remeshing/mapping were compared with experimental data for an Arcan mixed-mode specimen. Loading angles from 0 degrees to 90 degrees were analyzed. The maximum tensile stress criterion was able to predict the crack direction and path for all loading angles in which the material failed in tension. Residual strength was also accurately predicted for these cases.

Table of Contents

List of Figures iv

List of Tables viii

List of Abbreviations ix

Acknowledgements x

1 Introduction 1
- 1.1 Background 1
- 1.2 NASA Analysis Methodology 2
- 1.3 FRANC2D/L - An Engineering Tool 3
- 1.4 Crack Growth Methodology 4
- 1.5 Crack Growth Model 4
- 1.6 Objectives and Scope 5

2 Fracture and Direction Criteria 8
- 2.1 Fracture Criteria 8
  - 2.1.1 J-Path Integral 9
  - 2.1.2 Other Resistance Curve Criteria 11
  - 2.1.3 Crack Tip Opening Displacement 12
- 2.2 Direction Criteria 14
- 2.3 Summary 17

3 Crack Propagation Algorithms 23
- 3.1 Background 23
- 3.2 Combined Remeshing/Nodal Release Algorithm 25
  - 3.2.1 Nodal Release 26
  - 3.2.2 Local Remeshing and Mapping 26
  - 3.2.3 Algorithm Description 27
  - 3.2.4 Nodal Release Implementation 29
- 3.3 Crack Tip Constraint Model 30
  - 3.3.1 Constraint and Residual Strength 31
  - 3.3.2 Constraint and the Remeshing Model 32
- 3.4 Simulating Multi-Site Damage 33

3.4.1 Nodal Release MSD Model 33
3.4.2 Remeshing-Mapping with Multiple Cracks 34
3.4.3 Load Relaxation 34
3.5 Summary 35

4 State Variable Mapping 40
4.1 Mesh Mapping 40
4.2 Inverse Isoparametric Mapping 41
4.3 Stress Mapping 42
4.4 Element Variables Mapped 42
4.5 Accuracy of the Mapped Data 43
4.6 Algorithm Efficiency 44
4.7 Summary 46

5 Fracture Analyses Using Nodal Release 49
5.1 Analysis Background 50
5.1.1 Analysis Material Parameters 50
5.1.2 Mesh Size Convergence Study for Tearing 50
5.1.3 Three-Dimensional Analyses 51
5.2 Constraint Model 51
5.2.1 Plane Strain Core Height 52
5.3 Geometry and Specimen Independence 52
5.4 Multiple-Site Damage 54
5.5 Effects of Material Thickness on Plane Strain Core Height 56
5.6 Summary and Conclusions 57

6 Fracture Analyses with Remeshing 70
6.1 Analysis Background 70
6.2 Mode-I Analyses 71
6.3 Mixed-Mode I/II Analyses 72
6.4 Summary 73

7 Summary 81
7.1 Chapter Summaries 81
7.2 Conclusions 83
7.3 Recommendations for Future Work 83

References 85

A Equilibrium Equations **91**

A.1 Incremental Equations of Equilibrium 94
  A.1.1 Newton-Raphson Scheme 94
A.2 Incremented Iterative Solution 95
A.3 Implementation 97

B Plasticity Rate Equations **99**

B.1 Integrating the Plasticity Rate Equations 101
B.2 Consistent Tangent Modulus 104

C Plasticity Verification **106**

D Elastic-Plastic Validation **109**

List of Figures

Figure 1.1: Conceptual Crack Growth Methodology: how the crack growth model fits within the analysis architecture (after Potyondy, 1993) 7

Figure 1.2: Crack Growth Model: sequence of steps to grow a crack 7

Figure 2.1: The three modes of loading that can be applied to a crack (Anderson, 1995). 19

Figure 2.2: Schematic of stress singularity zone (Anderson, 1995) 19

Figure 2.3: Large strain crack tip finite element results of McMeeking and Parks (1979). Blunting causes the stress to deviate from the HRR solution close to the crack tip (Anderson, 1995) 20

Figure 2.4: Typical experimental values of crack tip opening angle measured for 76.2 mm wide, 2.3 mm thick M(T) specimens, where B is the specimen thickness (Dawicke and Sutton, 1993). 20

Figure 2.5: Load vs. crack extension data shows the effect of the plane strain core for 2024-T3 aluminum (Dawicke and Sutton, 1993) 21

Figure 2.6: Schematic of the plane strain core 21

Figure 2.7: Experimental results for the initial crack extension angle in PMMA (Maccagno and Knott, 1989). 22

Figure 2.8: Competing fracture mechanisms at a crack tip (Dalle Donne and Döker, 1997). 22

Figure 3.1: Schematic showing lines of symmetry for a middle crack tension specimen. During elastic-plastic fracture, fixity maintain symmetry along the vertical edge, and special stiff springs maintain symmetry along the fracture surface. 36

Figure 3.2: Schematic showing crack face forces for a nodal release fracture simulation with the crack path predefined. Crack face forces are maintained by special stiff springs. 36

Figure 3.3: Schematic showing the variation of stress and strain along a three-dimensional crack front (Anderson, 1995) 37

Figure 3.4: Normalized out-of-plane stresses in front of a three-dimensional crack indicate the level of constraint in front of the crack (Anderson, 1995) 37

Figure 3.5: Plane strain core concept. 38

Figure 3.6: Crack tip coalescence for a symmetry model. Multi-site damage configuration with tips ready to merge when criterion at either tip reaches critical. 38

Figure 3.7: Schematic of Tip Approaching Tip. Circles represent minimum radius for automatic propagation to continue. 39

Figure 3.8: Schematic of Tip Approaching Boundary. Circles represent minimum radius for automatic propagation to continue. 39

Figure 4.1: Qualitative mapping error assessment. Component: Maximum principal stress. (a) just before crack propagation, (b) just after crack propagation, remeshing and mapping, but before equilibrium has been restored. 47

Figure 4.2: Qualitative mapping error assessment. Component: Effective (von Mises) stress. (a) just before crack propagation, (b) just after crack propagation, remeshing and mapping, but before equilibrium has been restored. 47

Figure 4.3: Qualitative mapping error assessment. Component: Shear stress. (a) just before crack propagation, (b) just after crack propagation, remeshing and mapping, but before equilibrium has been restored. 48

Figure 5.1: Schematic of a deformed middle-crack tension specimen showing how symmetry is exploited. 58

Figure 5.2: Schematic of a deformed compact tension specimen showing how symmetry is exploited. 59

Figure 5.3: Mesh convergence study results for the 3" M(T) specimen. The small strain, six-noded triangle implemented in FRANC2D/L performs well at each of the element discretizations. 59

Figure 5.4: Plane strain core concept. 60

Figure 5.5: Comparison of simulated load vs. crack extension with experimental data for 6.0 inch wide C(T) specimens. The plane strain core closely matches the 3D result, and provides a good approximation to the experimental results. 60

Figure 5.6: Comparison of simulated load vs. crack extension with experimental data for 24.0 inch wide M(T) specimens. The plane strain core provides a much better approximation to the experimental results than either plane stress or plane strain. 61

Figure 5.7: Predicted failure load vs. specimen width for C(T) specimens with constant thickness and a/W. 61

Figure 5.8: Predicted failure stress vs. specimen width for M(T) specimens with constant thickness and 2a/W....62

Figure 5.9: Predicted failure load vs. initial crack length for C(T) with constant thickness and width....62

Figure 5.10: Predicted failure stress vs. initial crack length for M(T) with constant thickness and width....63

Figure 5.11: Additional single crack and MSD configurations analyzed (all configurations are symmetric)....64

Figure 5.12: Impending crack growth at Tip 1 for MSD Configuration F. Color contours of von Mises stress (Ksi) on deformed body magnified x15....65

Figure 5.13: Remaining ligament between the lead crack and MSD crack ready to break. Color contours of von Mises stress (Ksi) on deformed body magnified x15....66

Figure 5.14: Lead crack and MSD crack have merged, leaving a single crack. Color contours of von Mises stress (Ksi) on deformed body magnified x15....67

Figure 5.15: Variation in failure load as a function of PSC height for a 6" C(T) specimen 68

Figure 5.16: Variation in failure load as a function of PSC height for a 12" M(T) specimen....68

Figure 5.17: Variation of plane strain core height with specimen thickness....69

Figure 6.1: Schematic of Arcan test specimen and fixture....74

Figure 6.2: Finite element mesh for C(T) analysis....74

Figure 6.3: Detail of mesh near crack tip for 6" wide C(T) specimen....75

Figure 6.4: Load crack extension curve for C(T) analysis....75

Figure 6.5: Finite element mesh for 12" wide M(T) analysis....76

Figure 6.6: Load crack extension curve for M(T) analysis....77

Figure 6.7: Finite element mesh for Arcan analyses (30 degree load angle)....77

Figure 6.8: Shaded region showing elements that have yielded after 10 mm of crack propagation (30 degree load angle)....78

Figure 6.9: Observed and predicted crack paths for Arcan specimen....79

Figure 6.10: Load crack extension curve for Arcan analyses....79

Figure 6.11: Comparison of plane stress and plane strain analyses for Arcan specimen with 30 degree load angle. 80

Figure A.1: A body in two-dimensions with prescribed displacements and tractions...... 91

Figure A.2: Schematic of (a) iterative and (b) incremental strain update (Crisfield, 1991). 98

Figure B.1: Elastic predictor, normal return with correction to the yield surface for plane stress. 103

Figure C.1: Loading path for the tension torsion example. 106

Figure C.2: Material properties for the tension torsion example 107

Figure C.3: Fixity and loading conditions. Shear loads and axial loads are in different load cases to facilitate non-proportional loading 107

Figure C.4: Comparison of selected FRANC2D/L results with exact results 108

Figure D.1: Schematic of blunt notch specimen (w = 10 in, h = 12 in, c = 1.875 in).... 110

Figure D.2: Finite element idealization of blunt notch specimen 110

Figure D.3: Contour plot of von Mises stress (ksi) 111

Figure D.4: Blunt notch configuration and results 112

List of Tables

Table 4.1: Comparison of Mapping Algorithm Times (Analysis time: 1:59)........................45

Table 5.1: Analysis Material Properties........................50

Table 5.2: Uniaxial stress-strain yielding curve........................51

Table 5.3: Comparison of FRANC2D/L failure and link-up stresses with test results......54

Table D.1: Analysis Material Properties........................109

Table D.2: Uniaxial stress-strain curve........................111

List of Abbreviations

2a/W	Crack length to width ratio for M(T)
a/W	Crack length to width ratio for C(T)
BC	Boundary condition
C(T)	Compact tension specimen
CST	Constant strain triangle
CTOA	Crack tip opening angle
CTOD	Crack tip opening displacement
DIC	Digital image correlation
DoD	Department of Defense
EPFM	Elastic-plastic fracture mechanics
FAA	Federal Aviation Administration
FEM	Finite element method
FRANC2D/L	Fracture Analysis Code-2D with Layers
HRR	Hutchinson, Rice, and Rosengren (typically referring to a theoretical stress field near a crack tip)
LEFM	Linear elastic fracture mechanics
M(T)	Middle-crack tension specimen
MSD	Multi-Site Damage
NASA	National Aeronautics and Space Administration
NASIP	NASA Airframe Structural Integrity Program
NDI	Non-destructive inspection
OM	Optical microscope
PMMA	Polymethylmethacrylate (a type of plexiglass)
PSC	Plane strain core
SIF	Stress-intensity factor
ZIP2D	Two-dimensional elastic-plastic fracture code (NASA Langley)
ZIP3D	Three-dimensional elastic-plastic fracture code (NASA Langley)

Acknowledgements

I wish to thank my supervisory committee and especially my adviser, Prof. Daniel Swenson. His patience with me and confidence in me provided me the strength to finish.

Near the beginning of this work I had the privilege to spend six months at NASA Langley Research Center. My experiences there put this work into context and helped develop my current understanding of fatigue and fracture. I am indebted to my colleagues at LaRC both for their technical expertise as well as their friendship. In particular, Drs. Jim Newman and David Dawicke answered what must have seemed like endless questions and provided numerous fruitful discussions. Dr. Dawicke provided the experimental data for the M(T) and C(T) specimens and three-dimensional finite element results presented in Chapters 5 and 6. In addition, this work was funded through the NASA Aircraft Structural Integrity Program, NAG1-1503.

Collaborations and discussions with Dr. Wash Wawrzynek and Prof. Tony Ingraffea at Cornell University and with Prof. Mike Sutton at the University of South Carolina were both stimulating and rewarding. Prof. Sutton provided the mixed-mode Arcan experimental data for comparisons in Chapter 6.

The other graduate students in the applied computations lab kept life lively at the office.

Introduction

Cracks don't always grow straight ahead; sometimes they turn. Researchers in the fracture field have known this since they started observing and working to understand the fracture behavior of engineering materials. But the means to predict the behavior of multiple turning cracks under complex loading situations in the presence of significant plasticity have not been previously available.

Ever since the implementation of the finite element method (FEM) on computers, engineers have applied the method to increasingly complex problems. Indeed, more than 25 years ago FEM was first used to simulate elastic-plastic fracture (Anderson, 1973). However, applications of FEM to elastic-plastic mixed-mode[†] fracture problems have been limited. There are three fundamental issues that need to be resolved: 1) a fracture criterion applicable under mixed-mode loading conditions; 2) a direction criterion to predict the direction of growth; 3) a means of representing a growing crack without knowing *a priori* where the crack will go. In the case of linear elastic fracture mechanics (LEFM), solutions to each of these issues have already been demonstrated. For elastic-plastic fracture mechanics (EPFM), until recently, solutions to the first two issues had not been experimentally verified and solutions to the third issue have not been addressed adequately. This work addresses the third issue: representation that allows curvilinear crack growth without the crack path known *a priori.*

1.1 Background

Implicit in any discussion of fracture is the assumed relation of fracture to failure. While in some cases fracture is planned (such as when the pull-top of a beverage can is activated), many times fracture is not desirable, and contingency plans are in place to prevent fracture. However, fracture and its relationship to failure will always exist, even though the details of the relationship will change over time as technology evolves.

[†] Unless explicitly noted, the term *mixed-mode* refers to Mode-I/II.

One guiding force for fracture research during the past decade has been the NASA Aircraft Structural Integrity Program (Harris, 1990), but in fracture terminology, the initiation event was a failure. In the spring of 1988 Aloha Airlines Flight 243 suffered major structural failure during flight over Hawaii. The pilot was able to land the plane safely with minimal loss of life or injury to the passengers and crew, but the incident caused great concern over the safety of the aging commercial aircraft fleet. This concern prompted the U. S. Government to fund research at both NASA and the FAA to investigate the issues involved with understanding the problem of airframe structural integrity, and to formulate a plan of action to transfer the knowledge gained to industry. The resulting NASA program, under which this research is funded, is the NASA Airframe Structural Integrity Program at NASA Langley Research Center (Harris, 1990).

1.2 NASA Analysis Methodology

The NASA Airframe Structural Integrity Program (NASIP) is designed to gain understanding of the structural integrity problem in many areas, which are broken down into two major elements: (a) Quantitative Nondestructive Inspection Technology and (b) Structural Integrity Analysis Methodology (Harris, 1996).

The overall goal of the Quantitative Nondestructive Inspection Technology (NDI) element of the program is to develop nondestructive inspection technology to detect disbonding, corrosion, and fatigue cracks in fuselage structure (Harris, 1996). The current research is not part of the NDI element of the NASIP program, so NDI will not be discussed further.

The overall goal of the Structural Integrity Analysis Methodology is defined from two different perspectives: that of materials characterization, whose goal is to develop fatigue crack growth and fracture criteria for thin-sheet riveted metallic structures, and that of structural analysis, whose goal is to develop and verify the structural analysis methodology for stiffened shells with damage (Harris, 1996). The current research is most closely tied to the structural analysis methodology, since our task is to develop software that will become part of the structural analysis methodology. However, the work is also closely tied to the materials characterization goals of the NASIP program, since the analysis methodology implemented must accurately represent the current understanding of how the materials actually behave, not only in the laboratory at the coupon and component levels, but also at the structural system level.

1.3 FRANC2D/L - An Engineering Tool

There are many deliverables that will result from the NASIP research project. One class of deliverables is to have a range of engineering tools in the form of computer codes available for engineers in research institutions and industry. Every computer code is not intended to solve all problems; each code is intended to focus on a specific range of problems. The current research effort at KSU is centered around the FRacture ANalysis Code–2D with Layers (FRANC2D/L) computer code. This software was originally developed at Cornell University (Wawrzynek and Ingraffea, 1987).

The Cornell version of FRANC solves two-dimensional linear elastic fracture mechanics problems using the finite element approximation. The FRANC code was created in response to a need to model the true evolutionary behavior of crack propagation using finite elements, while addressing the limitations of the then current approach to modeling such problems (Saouma and Ingraffea, 1981; Swenson, 1985; Gerstle, 1986). The author of the code took a novel approach to implementing the finite element database. Rather than save a traditional finite element database (simple nodal coordinates and element connectivity), an advanced topological database is used to save the relationships between all adjacent nodes, elements and element edges. The result is that during the crack propagation phase of an analysis, where new surface area is created in the finite element mesh, the topology of the mesh is well defined. This is true even for intermediate operations such as local mesh editing, where the mesh is deleted in the region around the crack tip, the tip is extended, and a new mesh is generated for the updated configuration. The result is that during crack propagation the geometry of the problem is preserved automatically, and local remeshing operations on the region around the crack face can operate directly on the data base (rather than searching for necessary data) since all of the topology of the problem is preserved.

The current FRANC2D/L version of the software is a direct extension of the Cornell version of the software and is the result of two recent research projects at KSU. Sudhir Gondhalekar extended the original two-dimensional code to model layered structures such as lap joints and adhesively bonded joints (Gondhalekar, 1992). The model was limited to in-plane loading and deformations only. Srinivas Krishnan subsequently extended the code to include out-of-plane loading and deformations through linear, small strain bending (Krishnan, 1994). The current version of the code retains all of the necessary pre- and post-processing functionality from the Cornell version, as well as all of the fundamental fracture mechanics functionality, in addition to the new functionality added by Gondhalekar and Krishnan.

1.4 Crack Growth Methodology

Figure 1.1 shows the conceptual crack growth methodology. This methodology is an augmented version of that presented by Potyondy (1993). In the current version pre- and post-procession are included for clarity, and the crack growth model will be elaborated upon in greater detail.

The general methodology starts with the pre-processing stage, where the geometry, mesh, material properties, and boundary conditions are specified. The result of preprocessing is the initial representation, R_i. In the case of the FRANC2D/L implementation, which uses a topological database, this representation for the analysis contains all of the necessary information to run an analysis, but organizes the data for efficient pre- and post-processing.

The Analysis Model Generation phase of the methodology extracts data from the database and converts the data into a form that is efficient for the analysis phase. This phase includes such steps as building a traditional node and connectivity list from the database, optimizing the equation numbering to minimize the stiffness matrix profile, and initializing all of the data structures necessary for the Solution Procedure.

The Solution Procedure is responsible for applying boundary conditions and satisfying the equilibrium equations. The solution procedure is nonlinear incremental-iterative. As the solution progresses, the Solution Procedure is also responsible for monitoring fracture parameters at appropriate times during the analysis, and responsible for initiating appropriate actions when fracture criteria are satisfied.

The output from the Solution Procedure phase is the Results Transfer phase. This step in the methodology transfers the equilibrium output from the solution procedure to the final representation appropriate for post-processing and the crack growth model.

1.5 Crack Growth Model

The final step, and the essence of the crack growth methodology, is the Crack Growth Model. Figure 1.2 focuses in more detail on the Crack Growth Model. The input to the model is R_f^k, the final representation, based on the current equilibrium state. The first step of the Crack Growth Model is to apply the fracture and direction criteria to determine the crack growth direction. In the case of linear elastic fracture mechanics the direction criteria may be dependent upon the fracture criterion (Erdogan and Sih, 1963), while in the case of elastic-plastic fracture mechanics the direction criterion is more likely to be dependant upon the stress or strain state local to the crack tip, and may or may not be tied to the fracture criterion in a theoretical sense.

The Crack Extension Algorithms grow the crack using the predicted direction and user specified crack growth increment. This step of the methodology first deletes the mesh in the region local to a crack tip, then extends the crack.

The Remeshing Algorithms place a rosette of elements around the crack tip, then rebuild the mesh around the crack tip. The crack extension and remeshing algorithms are essentially the same as for the original LEFM implementation, but modifications transparently manage elastic-plastic related data.

The fourth step of the Crack Growth Model is essential for elastic-plastic crack growth. The Mapping Algorithms are responsible for maintaining the plastic history and displacement solution across the mesh changes created by the crack extension and remeshing algorithms. The plastic history includes primarily nodal displacements and gauss point stresses, but also includes the stress work, radius of the yield surface, and flags that indicate yielding state.

The final step of the Crack Growth Model is to return the model to equilibrium, resulting in a new initial representation model, R_i^k, at the new geometric configuration. Conceptually, this step takes place as part of the crack growth model. For efficiency reasons, during automatic propagation equilibrium is re-established as the initial step of the solution procedure.

1.6 Objectives and Scope

The primary objective of this work is to develop a finite element model capable of modeling quasi-static, elastic-plastic, mixed-mode crack growth. A secondary objective is to implement the model in a relatively general way and in relatively user-friendly way, such that researchers and practicing engineers can apply the model to realistic problems. These objectives were met by extending an existing fracture simulation framework to include the necessary algorithms to model elastic-plastic fracture. The remainder of this work discusses the implementation of these algorithms.

This work is neither a treatise on fracture mechanics, nor a treatise on finite elements. Rather, it addresses the issues necessary to model curvilinear elastic-plastic crack growth: a means of representing a crack without knowing *a priori* where the crack will go. In the process, discussions of supporting fracture mechanics and finite elements principles are included to provide context for modeling assumptions necessary to model the temporal, evolutionary nature of the problem.

The Crack Growth Methodology illustrated in Figure 1.2 essentially serves as the outline for the remainder of this work. Chapter 2 discusses various possible fracture criteria and direction criteria. Limitations of criteria in the literature are addressed, with the primary focus remaining on criteria that can be implemented on a framework that allows multiple interacting cracks in a single structure. Chapter 3 discusses crack extension algorithms for elastic-plastic analysis. The original algorithms were modified to allow necessary underlying data structures to manage elastic-plastic data. In addition, new algorithms were introduced to allow elastic-plastic crack growth along an edge of symmetry to allow symmetry when the crack lies on an edge of symmetry in the specimen. Chapter 4 discusses the mapping algorithms. These algorithms preserve the plastic history as the mesh changes with crack growth. Chapter 5 presents analysis results for a number of Mode-I symmetry crack growth analyses and compares the results with experimental results from the literature. Chapter 6 presents analysis results for both Mode-I and mixed-mode crack growth using crack propagation with remeshing and mapping. The Mode-I results are compared with previous symmetry analysis results as well as experimental results. The mixed-mode analysis results are compared only with experimental results from the literature. Chapter 7 summarizes this work and makes recommendations for future work.

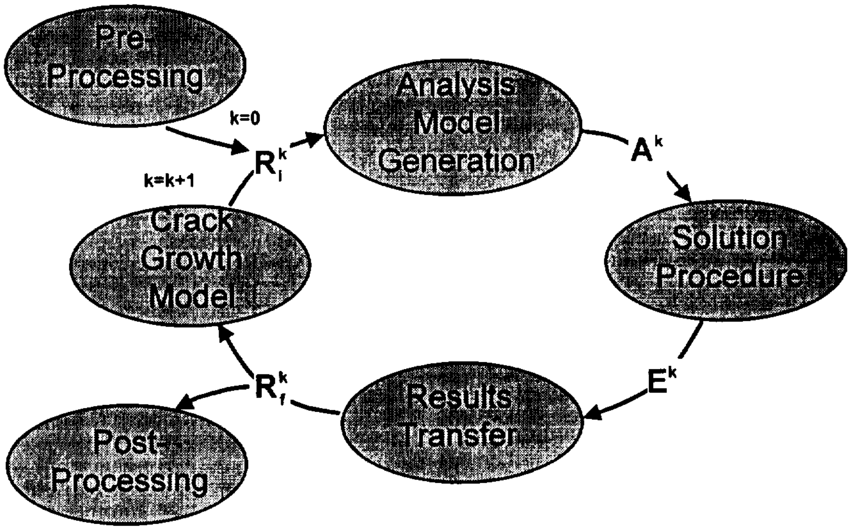

Figure 1.1: Conceptual Crack Growth Methodology: how the crack growth model fits within the analysis architecture (after Potyondy, 1993).

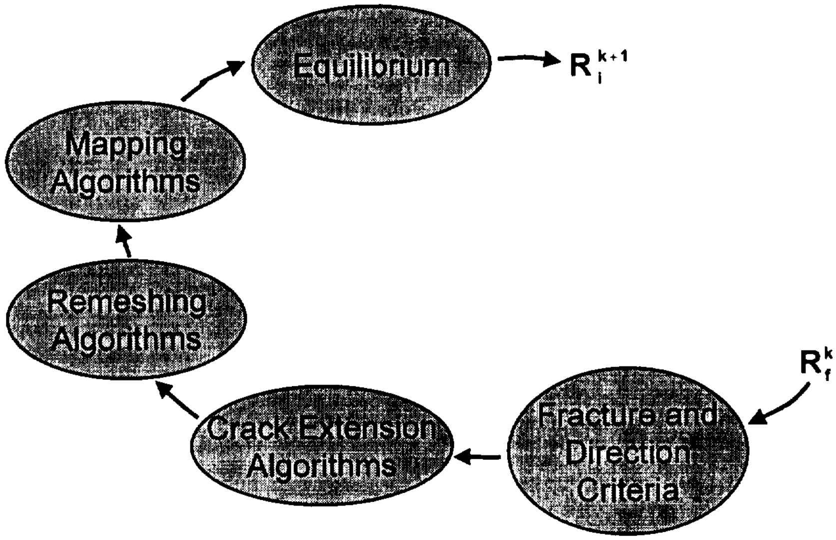

Figure 1.2: Crack Growth Model: sequence of steps to grow a crack.

Chapter 2

Fracture and Direction Criteria

Two essential components of a software framework to predict mixed-mode tearing are a fracture criterion and a direction criterion. This chapter discusses a number of alternatives for both fracture and direction criteria, from both an historical perspective and a materials perspective, to provide insight into the decisions made for the criteria implemented.

2.1 Fracture Criteria

Early work in fracture mechanics focused on both the energy release required to create new crack surface area (Inglis, 1913), as well as the stresses in the body assuming isotropic linear elastic material behavior (Westergaard, 1939; Sneddon, 1946; Irwin, 1957; Williams, (1957). A typical presentation of the result is that the stress in any linear elastic cracked body can be described by the following equation in polar coordinates with the origin at the crack tip

$$\sigma_{ij} = \left(\frac{k}{\sqrt{r}}\right) f_{ij}(\theta) + \sum_{m=0}^{\infty} A_m r^{m/2} g_{ij}^{m}(\theta) \tag{1}$$

where σ_{ij} is the stress tensor, r and θ define a point in polar coordinates relative to the crack tip, k is a constant, and f_{ij} and g_{ij} are functions of θ. The higher order terms depend on geometry, but the first term is proportional to $1/\sqrt{r}$. As r approaches zero, the first term approaches infinity, but the higher order terms remain finite or approach zero. The result is that the first term dominates as r approaches zero. The stress intensity factor, K, is a convenient measure of the amplitude of the stress near the crack tip, where $K = k\sqrt{2\pi}$. Figure 2.1 shows the three modes of loading that can be applied to a crack. In Mode-I loading the load is applied normal to the crack plane; in Mode-II the loading corresponds to in-plane shear, which slides the crack faces relative to one another in the crack plane; and for Mode-III the loading refers to out-of-plane shear. The components of the three modes can be superimposed for the total solution of the problem. For a plate with a horizontal crack and a uniform far field stress perpendicular to the crack only Mode I loading is present. In this case equation (1) reduces to

$$\sigma_{yy} = \frac{K_I}{\sqrt{2\pi r}}. \tag{2}$$

Figure 2.2 is a schematic plot of the stress normal to the crack plane due to the truncated form of Equation (1) compared to the stress due to the full expansion of the stress. The figure shows that for small values of r near the tip, the solutions match. This region where the solutions match is typically called the singularity dominated zone or the K dominated zone. In this region the stress-intensity factor completely defines the crack tip conditions. According to Anderson (1995), *this single parameter description of crack tip conditions turns out to be one of the most important concepts in fracture mechanics.*

For linear elastic fracture mechanics the stress intensity factor is well established as a fracture parameter; however, defining a single parameter to characterize elastic-plastic fracture mechanics has proven more difficult. For elastic-plastic problems two widely recognized and accepted approaches to characterizing fracture are the J-path integral and the crack-tip opening angle (CTOA), or equivalently, crack-tip opening displacement (CTOD). These criteria are representative of two classes of criteria: resistance curve criteria and constant critical parameter criteria. The remainder of this section first discusses the J-Integral as a fracture criterion because of its recent intense scrutiny and popularity. Then other resistance curve criteria are discussed. Finally, the crack tip opening displacement is discussed.

2.1.1 J-Path Integral

The J-integral was introduced by Rice (1968) and is defined as a path-independent line integral enclosing the crack tip:

$$J = \int_{\Gamma} \left(w n_x - T_i \frac{\partial u_i}{\partial x_1} \right) ds \tag{3}$$

where w is the strain energy density, T_i are components of the traction vector along the boundary of the contour, u_i are the displacement vector components, and ds is a length increment along the contour Γ. Rice defined the J-integral based on the deformation theory of plasticity, so the integral is strictly only defined for linear or nonlinear elastic solids. Rice showed that J is the energy release rate in a nonlinear elastic body that contains a crack. For stationary cracks and monotonically increasing loads, the deformation theory of plasticity will accurately model the plasticity behavior. However, for growing cracks a region of elastic unloading exists in the crack tip wake and nonproportional loading occurs in front of the crack tip.

Hutchinson (1968) and Rice and Rosengren (1968) (HRR) independently showed that J characterizes the crack tip conditions and that when the stresses and strains vary as $1/r$ near the crack tip J remains path independent. But the HRR singularity, as the $1/r$ singularity at the crack tip has come to be known, displays an anomaly; that is, it predicts infinite stresses as $r \to 0$.

Experimental results show that for many high fracture toughness materials, plastic deformation causes an initially sharp crack to show blunting (Wells, 1961). McMeeking and Parks (1979) performed finite element analyses of crack tip configurations that included large strain theory and finite geometry changes. They showed that the HRR singularity, which neither considers the effect of the blunting of the crack tip on the stress fields, nor takes into account the large strains present near the crack tip, is invalid in a small region near the crack tip. Figure 2.3 shows some results of McMeeking and Parks (1979). Note that the axes are nondimensionalized and are invariant as long as the plastic zone is small compared to specimen dimensions. The graph shows that the results of the large strain analysis peak for $x\sigma_o/J$ at approximately unity, and decreases as x approaches 0. The HRR singularity is invalid within this region near the tip, where the stresses are influenced by large strains and crack blunting.

Hutchinson and Paris (1979) showed that for fully yielded conditions, J-controlled crack growth is valid when:

$$\frac{b}{J_{Ic}}\frac{dJ}{da} = \omega >> 1, \qquad (4)$$

where b is the net section ligament of the specimen. Further, for J to be a useful fracture parameter, Anderson (1995) notes that steady state crack growth is necessary, and that even when J-controlled crack growth is obtained, steady state values of J are rarely reached. The conclusion is that under many, if not most, situations, the J-resistance curve is not independent of specimen configuration and so loses both generality and effectiveness as a fracture parameter.

2.1.2 Other Resistance Curve Criteria

Despite the theoretical limitations of the *J*-Integral as a fracture criterion, it continues to see wide spread use, primarily as a resistance curve approach to predicting fracture. However, a number of other fracture criteria have been reported in the literature and have been used with varying degrees of success.

Dawicke and Newman (1997) evaluated seven different fracture criteria for Mode-I fracture. They grouped the criteria into two categories: (1) constant critical parameters and (2) resistance curve parameters. The constant critical parameter approach assumes that an event such as fracture, growth, or link-up (depending on the criterion), will occur when the critical value is satisfied. The resistance curve approach assumes a unique relationship between the resistance curve fracture parameter and the amount of crack growth. The criteria evaluated were:

- Crack-tip opening angle (CTOA) (constant critical parameter)
- Plastic zone link-up model (constant critical parameter)
- Stress-intensity factor resistance curve (K_R)
- Effective Stress-intensity factor resistance curve (K_{Reff})
- *J*-integral resistance curve (J_R)
- Crack opening displacement resistance curve (δ_R)
- T^*-integral resistance curve

While the elastic-plastic resistance curve criteria could predict the Mode-I fracture behavior, they are limited in that adequate resistance curve data must be available, otherwise long crack simulations will require curve extrapolation. In addition, the resistance curves were not widely transferable between specimen types. The CTOA constant critical parameter criterion was able to accurately predict the behavior of all of the experiments, including single crack and multiple crack panel specimens.

Other criteria have been evaluated in the literature for mixed mode fracture. Two of the most recent are included here. Lee et al. (1996) used a linear relationship between plastic energy and crack size to predict fracture. However, it's not clear how to apply the criterion in the case of multiple cracks in the same body, especially if the crack tips are approaching for link-up. Similarly, Kuang and Chen (1997) used the plastic strain energy and showed that the energy required for initiation is relatively independent of mode mixity. Energy criteria such as these show promise as mixed-mode fracture parameters. But in addition to the limitations inherent as resistance curves, they also have limitations in multiple cracking scenarios. As long as the plastic zones for each of multiple tips are distinct, each has its own unique plastic energy fracture parameter. However, after the plastic zones for two tips link-up it is unclear whether the plastic energy for the two can be considered separately. Traditionally, a plastic zone link-up criterion would be used as a secondary criterion. Dalle Donne and Döker (1997) present δ_R mixed-mode experimental results which show that crack opening displacement resistance curves do not correspond with Mode-I results from either C(T) or M(T) specimens, so Mode-I test results may not apply for mixed-mode situations.

To summarize the discussion on the resistance curve approach to characterizing fracture, there are resistance curve parameters that will work for characterizing mixed-mode fracture for a single crack under specific conditions. However, all resistance curve parameters have a limitation on crack size, and it is not clear how to apply global energy approaches to multiple turning cracks. Resistance curves will continue to be used because of their ease of use, but they lack generality in that they are not widely transferable between specimen configurations or specimen types.

2.1.3 Crack Tip Opening Displacement

The crack tip opening displacement (CTOD), or its equivalent, the crack tip opening angle (CTOA) was identified as a possible measure of fracture toughness by Wells (1961) when he noticed, during testing of high toughness materials, that the degree of crack blunting increased in proportion to the toughness of the material. Typically CTOA and CTOD are defined in terms of each other as:

$$\psi = 2\tan^{-1}\left(\frac{\delta}{2d}\right) \tag{5}$$

where $\psi \geq \psi_c$ is the fracture criterion for CTOA and $\delta \geq \delta_c$ is the fracture criterion for CTOD, both defined a distance d behind the crack tip.

Dawicke and Sutton (1993) provide a summary of significant CTOA/CTOD work up through 1993 for 2024-T3 aluminum. Experimental data (Demofonti and Rizzi, 1991; Newman et al., 1992; Dawicke and Sutton, 1993) indicate that surface measured values of CTOA decrease to a constant value after a small amount of crack growth (approximately 1-2x the sheet thickness). Figure 2.4 shows experimental values of CTOA measured at various crack lengths using optical microscopy and digital image correlation methods (Dawicke and Sutton, 1993). The data clearly show the decrease in CTOA for short crack lengths in the range of 1-2x the thickness of the material. After the initial transient region, CTOA is essentially constant for the remaining crack growth. Recent three-dimensional residual strength analyses (Dawicke and Newman, 1998) have shown that for specimens of the same thickness, a single value of the critical fracture parameter can predict residual strength over a wide range of specimen sizes and configurations for both the M(T) and C(T) specimens.

Computational studies of local crack tip fields for stationary cracks in thin sheets (Hom and McMeeking, 1980; Newman et al., 1993a) have shown that substantial constraint develops in thin materials prior to crack growth, and that the constraint at mid-thickness is about twice the constraint that occurs at the surface. Other computational studies of local crack tip fields for moving cracks have shown that the local constraint stabilized after a small amount of crack growth (Sommer and Aurich, 1991). This is in accordance with the data in Figure 2.4.

Dawicke and Sutton (1993) have shown experimental results that correlate with the computational studies of constraint. They report that the tearing process is 3D, both during the initial transient, and after CTOA has stabilized. The crack front profile can be curved and shows tunneling effects (even for specimens as thin as 2.3 mm), or the fracture surface can be slanted through the thickness, depending on the crack orientation with respect to the material rolling direction. Both the results of Newman et al. (1993a) and Dawicke and Sutton (1993) show that displacements on the crack front near the free surface are higher than in the interior of the specimen. Both the experimental data and the analyses discussed here support the idea that even for thin-sheet materials, significant constraint develops around the crack tip. In addition, both indicate that the constraint stabilizes after a small amount of crack growth.

However, 2D simulations of tearing using CTOA as the fracture criterion continue to show good correlation with experimental data. Figure 2.5 is an example of load vs. crack extension from Dawicke and Sutton (1993) for 2024-T3 aluminum. The figure compares two computer simulations with the experimental data – the first is for a plane stress analysis and the second is for a plane stress analysis with a plane strain core in the finite element mesh to account for the higher constraint at the crack tip. Figure 2.6 shows a schematic of the plane strain core concept (Newman et al., 1988). Dawicke and Sutton (1993) tuned the height of the plane strain core to obtain numerical results that match experimental data. After accounting for the constraint at the crack tip, excellent agreement was obtained (see Figure 2.5).

Amstutz et al. (1995a, 1995b) used the crack tip opening displacement to characterize the *mixed-mode* fracture behavior of 2024-T3 and considered the opening and sliding displacements separately. They found that CTOD measured 1 mm behind the crack tip, after an initial transient region, approached a constant value for *all modes of loading*, indicating that CTOD can be used as a *mixed-mode* fracture criterion for 2024-T3. They also showed that the critical value of CTOD is a function of the material rolling direction, varying by about 25 percent for a crack growing against the rolling direction, compared to growing with the rolling direction.

In summary two different classes of failure criteria have been considered: resistance curves and constant critical parameters. Resistance curves have an inherent limitation on the maximum crack growth without extrapolation. In addition, is not clear how to apply most resistance curves for Mixed-Mode cracking. In one case, the resistance curve was not the same for Mixed-Mode as for Mode-I. When multiple cracks are involved, crack tip link-up may be problematic, since as two tips approach, energy based methods may prove difficult to evaluate. In contrast, the CTOD constant critical parameter has been shown experimentally to be constant over wide range of mode-mixity. Since CTOD is measured local to the crack tip, multiple crack interaction effects are expected to be negligible (in Mode I, link-up was accurately predicted). Finally, CTOD is relatively simple to implement compared to domain integral methods.

2.2 Direction Criteria

For linear elastic fracture mechanics, the fracture criterion can be intimately tied to the direction criterion. The conceptually simplest criterion is the $\sigma_{\theta\text{-max}}$ criterion, where the crack propagates in a direction perpendicular to the direction of maximum tensile stress (Erdogan and Sih, 1963). Stability and direction are determined based on well-known hypotheses of brittle fracture in the K_I/K_{II} plane. Linear elastic fracture mechanics predicts reasonably well the behavior of brittle materials, partly because these materials show a relatively consistent behavior from pure Mode-I loading to pure Mode-II loading (Erdogan and Sih, 1963). Under pure Mode-I the crack goes straight ahead. As increasing mode-II is introduced for an initial crack geometry, kinking at the crack tip is introduced and continually grows with increasing Mode-II. For example, Figure 2.7 shows experimental results for the initial crack extension angle in polymethylmethacrylate

(PMMA). Also included is the predicted angle based on the maximum tensile stress criterion. The theory matches well with the material behavior over the full range of mode-mixity.

In contrast, ductile materials do not always show this type of behavior because ductile materials have complex crack tip behavior at failure that is not easily characterized. Results by Maccagno and Knot (1992) on HY130 lightly tempered steel tested at room temperature showed a dramatic deviation from traditional LEFM behavior. Sharp cracks in Mode-I loading failed along planes of maximum shear, which leads to "zig-zag" fracture profiles that cannot be described by traditional LEFM fracture criteria. In effect, while remote loading was Mode-I with respect to the crack, the local failure was Mode-II. Interestingly, HY130 steel in the identical condition but tested at -196° C, can be described by the maximum tensile stress criterion under mixed-mode loading.

Recent studies by Amstutz et al. (1995b) on 2024-T3 aluminum and by Dalle Donne and Döker (1997) on 2024-T3 aluminum and on 550 structural steel show that for these materials there is a sharp transition from Mode-I type fracture to Mode-II type fracture. In Mode-II, a “shear crack” forms as a result of shear of localization at the crack tip. Dalle Donne and Döker (1997) described this behavior, based on experimental and numerical observations, in terms of two competing mechanisms acting at the crack tip for a ductile material under mixed-mode loading. Figure 2.8 depicts these two mechanisms schematically for an initially smooth notch tip. Under mixed-mode loading one side of the notch blunts from tensile stresses, and the other side sharpens from shear strains. Mode-I failure occurs when the tensile stresses in the blunt region dominate. Mode-II failure occurs when shear strains localize along the sharpened side of the notch. The competition between the mechanisms is resolved in the way that the material micro-structure responds to the applied stress and strain fields. The PMMA always fails due to tensile stresses at the crack tip. The HY130 steel always fails due to shear localization at the crack tip. Other materials, such as the 2024-T3 and 550 structural steel show a transition between tensile dominated and shear dominated failure.

Ghosal and Narasimhan (1994) provided finite element results that help explain these two failure mechanisms under mixed-mode loading. Their plane strain model assumed large strain, but small-scale yielding. A Gurson type constitutive model was used to account for micro-void nucleation, growth and coalescence. Their results also showed that a portion of the notch surface blunts and the remaining portion sharpens, and that the plastic shear strain localizes in the sharpened portion of the notch. The micro-void volume fraction was always nearer the blunted part of the deformed notch and independent of mode-mixity. The computer model did not include a means to explicitly represent material failure in the shear band (micro-voids cannot form in the shear band because of the lack of necessary stress triaxiality), but shear failure was simulated using an assumed maximum shear strain criterion. They considered a range of loading angles from pure Mode-I to pure Mode-II, using $\Psi = \tan^{-1} K_I/K_{II}$ to characterize the loading angle at the crack tip. Their results showed that for $30° \leq \Psi \leq 90°$, micro-void coalescence at the blunted portion of the notch is the dominant failure mechanism, and that for $0° \leq \Psi \leq 15°$ the material failed due to shear localization at the sharpened portion of the notch tip. For $15° \leq \Psi \leq 30°$ both of the mechanisms were active, and cause failure simultaneously.

These ranges of failure modes match reasonably well with the experimental results of Amstutz (1995b), and numerical results of Sutton et al. (1997). Posing their results in terms of mode-mixity, $\Psi = \tan^{-1} K_I/K_{II}$, where the stress-intensity factors are taken from Sutton et al. (1997) for each loading angle, micro-void coalescence dominates for $40° \leq \Psi \leq 90°$, and shear localization dominates for $0° \leq \Psi \leq 40°$.

Several different criteria have been discussed in the literature for predicting the direction of crack growth under elastic-plastic conditions. Mahanty and Maiti (1989) showed that the maximum tensile stress criterion will predict the crack growth direction for tensile dominated fracture. Maccagno and Knott (1992) indicate that it may be possible to obtain a relationship between the opening and sliding components of crack tip opening displacement at initiation to predict the transition between Mode-I and Mode-II growth. But to date, no such relationship exists. Kfouri and Brown (1995) and Kfouri (1996) present a direction criterion based on maximum energy release rates at the tip of a short kinked crack. They develop the theory for LEFM, but show that a transition from tensile to shear failure can exist dependent on material parameters. Lee et al. (1997) used the maximum tensile force at the crack tip node.

Sutton et al. (1997) analyzed the Amstutz (1995a, 1995b) data using small strain, small scale yielding, but with two terms in the theoretical asymptotic stress-intensity factor expansion. He also described this type of ductile material behavior in terms of void initiation and growth concepts for the aluminum alloy 2024-T3. Sutton found that the direction of propagation could be described in terms of a ratio of the mean stress σ_m, and the effective stress σ_e. When the ratio is greater than critical, the propagation angle corresponds to the direction where the ratio is maximum; if the ratio is less than critical, the propagation angle corresponds to the direction where the effective stress is maximum. The mean stress and effective stress are evaluated on a circle of small radius around the crack tip. When the ratio is large, a high level of stress triaxiality exists. This empirical approach is attractive, but implementation details would be problematic. Finding maximum values of σ_m and σ_e require "circle-plot" evaluations of these stress functions at small radii around the crack tip. Unfortunately, the maximum values are located on wide plateaus where very small numerical errors can lead to erroneous results.

Most recently, Chao and Liu (1998) considered a ratio of the maximum shear stress to maximum tensile stress, evaluated on a circle near the crack tip. They showed that a critical value of the ratio exists that predicts the transition from shear to tensile failure. If the ratio is less than critical, tensile failure exists. If the ratio is less than critical, shear failure exists. As with the Sutton et al. (1997) criterion, implementation may be problematic since results evaluated on a circle near the crack tip may be on wide plateaus where very small numerical errors can lead to erroneous results.

In summary, experimental evidence suggests that different materials have different dominant failure mechanisms. No clear theoretical basis as yet is available in the literature that explains the transition between tensile failure and shear failure. It is possible that an empirical transition based on experimental evidence, coupled with a dual failure mechanism, maximum tensile stress, and maximum shear stress could predict the direction, but such a criterion was not investigated. A wide range of materials have most of their behavior characterized by the maximum tensile stress criterion. In addition it is somewhat unusual (though not impossible) for cracks to initiate and grow under Mode-I loading, then be subjected to an extreme overload in Mode-II. That is to say, most cracks start and grow dominated by Mode-I, with curving to minimize Mode-II.

2.3 Summary

In summary, the fracture criterion and direction criterion are inextricably tied to the crack tip stress and strain state, but no convenient, unified theory exists that defines the fracture behavior for elastic plastic materials. The above referenced recent research indicates that a number of different fracture criteria and direction criteria can be used under certain circumstances. For the work presented here the fracture criterion is assumed to be the magnitude of the crack tip opening displacement vector, and the direction criterion is assumed to be maximum tensile stress at the crack tip. CTOD is largely unproven to be constant under mixed-mode loading for materials other than 2024-T3 Aluminum, so its applicability to other materials is somewhat in question. It's clear that the maximum tensile stress criterion will not correctly predict the fracture direction for all cases. However, the criterion is simple, requires no special materials parameters for implementation, and does perform well under a wide variety of circumstances for a wide variety of materials. More widely applicable criteria are an area for future research.

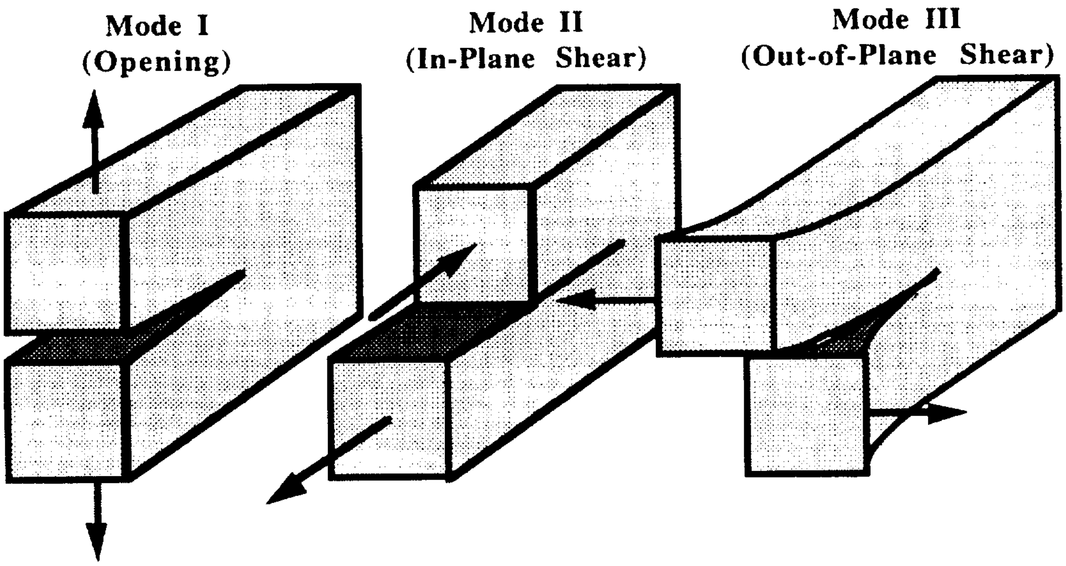

Figure 2.1: The three modes of loading that can be applied to a crack (Anderson, 1995).

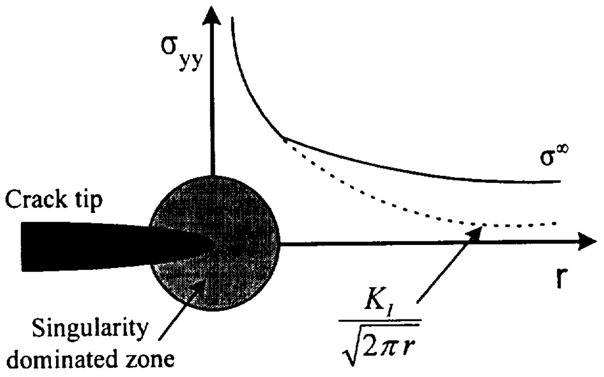

Figure 2.2: Schematic of stress singularity zone (Anderson, 1995).

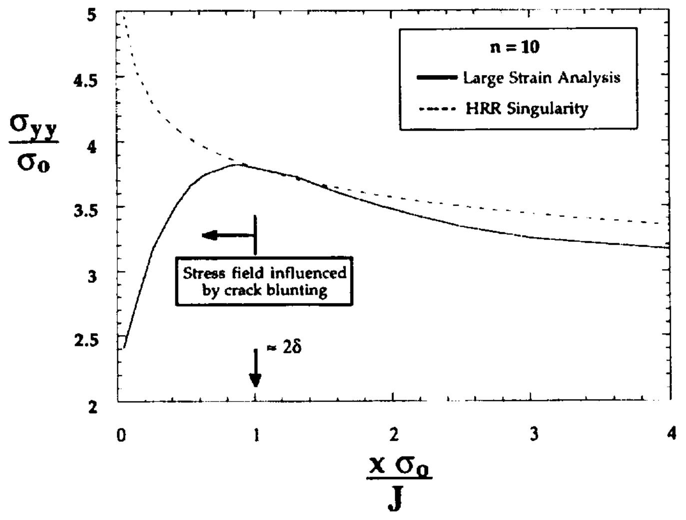

Figure 2.3: Large strain crack tip finite element results of McMeeking and Parks (1979). Blunting causes the stress to deviate from the HRR solution close to the crack tip (Anderson, 1995).

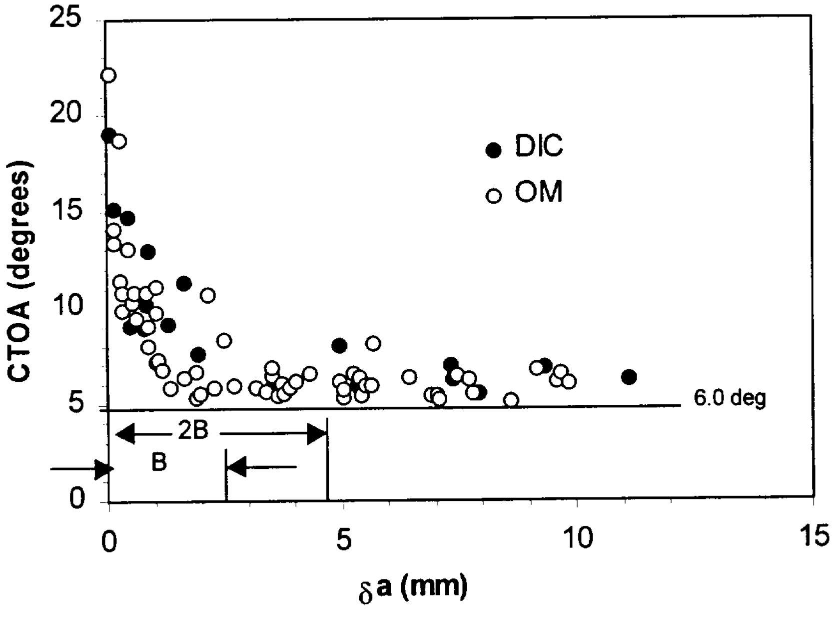

Figure 2.4: Typical experimental values of crack tip opening angle measured for 76.2 mm wide, 2.3 mm thick M(T) specimens, where B is the specimen thickness (Dawicke and Sutton, 1993).

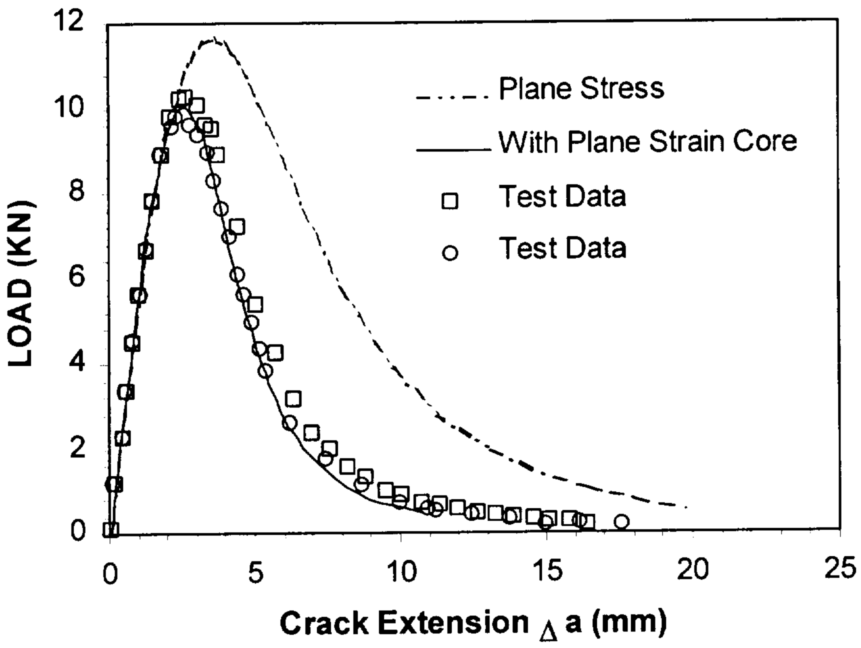

Figure 2.5: Load vs. crack extension data shows the effect of the plane strain core for 2024-T3 aluminum (Dawicke and Sutton, 1993).

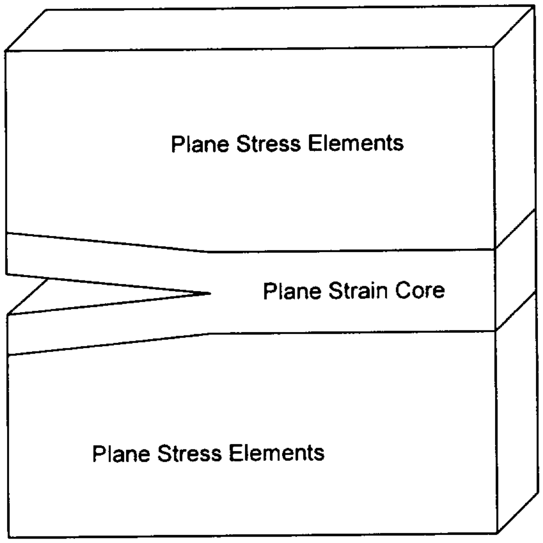

Figure 2.6: Schematic of the plane strain core.

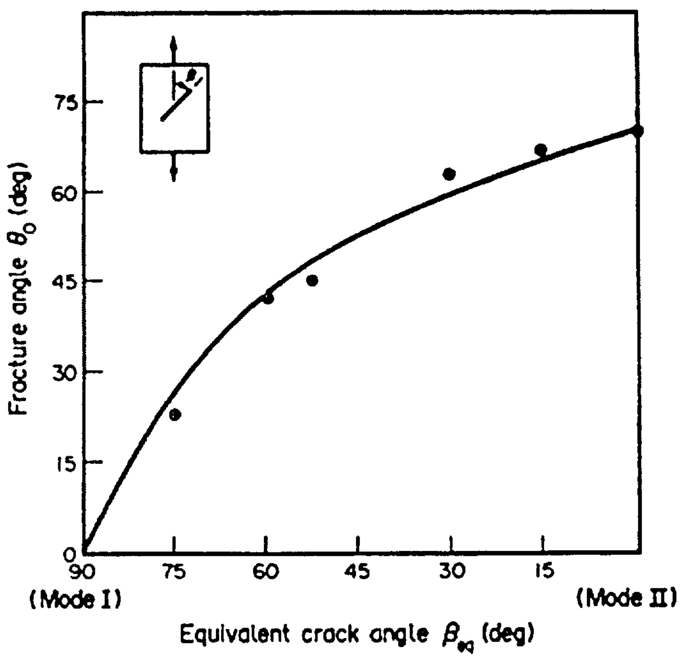

Figure 2.7: Experimental results for the initial crack extension angle in PMMA (Maccagno and Knott, 1989).

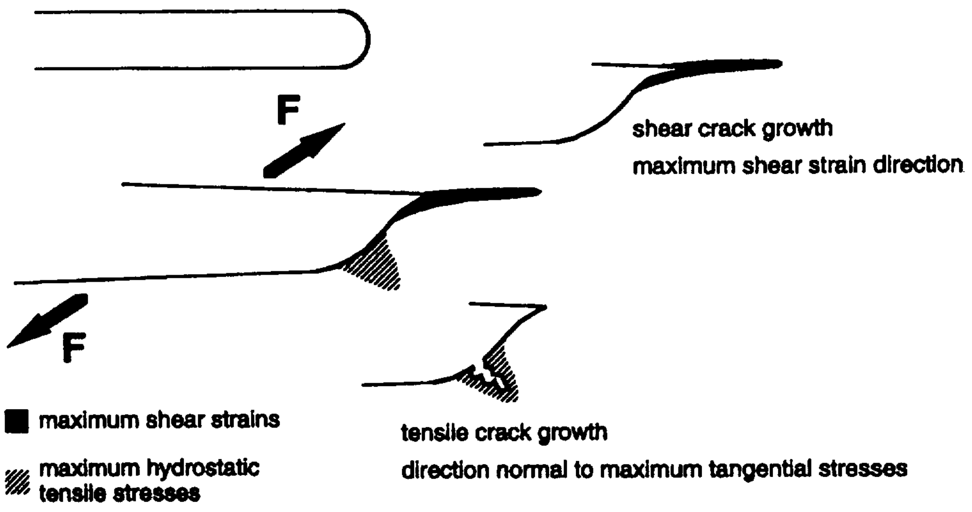

Figure 2.8: Competing fracture mechanisms at a crack tip (Dalle Donne and Döker, 1997).

Chapter 3

Crack Propagation Algorithms

For more than two decades special purpose finite element codes have been used to model crack growth in the presence of plasticity. This chapter describes many of these models and then outlines the implementation and capabilities of the algorithms implemented for this work.

3.1 Background

The earliest crack propagation algorithms were based on a nodal release technique, whereby the crack path is predefined in the finite element mesh (Anderson, 1973; de Koning, 1977; Newman, 1974). When the fracture criterion is satisfied or exceeded the forces imposed to hold two coincident nodes at a crack tip are released, thus creating new surface area for the crack and a new crack tip at the adjacent node. Typically, stiff spring elements are used to tie the coincident nodes together. This technique is still in use today in both two- and three-dimensional codes (Maiti and Mahanty, 1990; Roy et al., 1993; James, 1997; Dawicke and Newman, 1998). Nodal release is typically applied to Mode-I cracks, but can be applied to curving cracks with a predefined crack path.

A number of other approaches to modeling crack propogation have also been published in the literature, and representatives of these are included here. Nakagaki et al. (1979) analyzed Mode-I crack growth by deforming the crack tip elements such that the crack tip shifts ahead and employed a mapping procedure to transfer state variables to the modified mesh however remeshing was not included. Deng (1990) studied crack tip fields for dynamic fracture. His software assumed small-scale yielding at the crack tip, but included effects of the plasticity. An Eulerian formulation allowed the finite mesh to translate in steady state with the crack tip. The model included effects for only Mode-I loading. Lim (1992) modeled mixed-mode fracture using discrete cracks with automatic remeshing where there was plasticity in the crack wake, but the direction and fracture criterion were governed by LEFM. Mapping was used to transfer state variables for the remeshing region. However, since remeshing occurred only in the LEFM region in front of the growing crack, only displacements were mapped. The technique by Bakuckas et al.

(1993) does not require a predefined crack path, but requires the crack path to follow existing element boundaries in the mesh using a node splitting technique.

More recently, Marusich and Ortiz (1995), implemented a dynamic Lagrangian finite element program to predict fractures of high-speed machining processes. The model includes both a shear localization mechanism to initiate fracture and a traditional stress intensity based fracture criterion to propagate cracks. A continually updated mesh is maintained by automatic remeshing algorithms.

Camacho and Ortiz (1996) report on a similar dynamic Lagrangian finite element program applied to modeling impact damage in brittle materials. The fracture criteria are based on maximum shear and maximum tensile stress values. Cracks are restricted to propagating along existing element boundaries and use shear and tensile strain softening behavior.

Lee et al. (1997) recently published work that is the most directly related to this work. The authors modeled non-self-similar crack growth using finite elements and small strain plasticity. The fracture criterion is based on a global plastic work criterion, whereby the crack propagates according to a linear relationship between plastic work and crack extension. The direction criterion has the crack propagate perpendicular to the maximum tensile force at the crack tip node. The actual crack propagation algorithms used were not clearly specified. It appears that at each propagation step an external program is used to determine propagation direction. Then a separate external program somehow updates the mesh in the new configuration. Finally the analysis is resumed using load relaxation to relax crack face tractions before external loading resumes.

While this most recent approach is similar to the approach used here, some differences exist:

- In the current work a local fracture criterion is used, while Lee et al. (1997) use a global energy fracture criterion. The local approach makes possible multiple cracks, each following a different curving path in the model. The energy approach is untested for curving cracks, and is unlikely to work for multiple cracks, since only the global energy is considered, not the energy at each tip (currently the T^* integral shows promise as a local crack tip energy-based criterion (Dawicke and Newman, 1998)).

- The current implementation for this work can include multiple cracks in multiple layers and has fully automatic crack propagation without user intervention.

3.2 Combined Remeshing/Nodal Release Algorithm

No comprehensive algorithms are referenced in the literature that can handle multiple curving and interacting cracks in the presence of plasticity (non-small scale yielding conditions, net section yielding, etc.). The approach adopted for solving this class of elastic-plastic fracture problems is to extend the LEFM approach of Wawrzynek and Ingraffea (1987) to include the effects of plasticity. Their approach to fracture simulation uses an explicit representation for each crack. Crack growth is modeled using remeshing algorithms that update the mesh only locally to the propagating crack. For LEFM analyses, no history variables are necessary, and a new linear analysis is run at each propagation step. For elastic-plastic fracture mechanics (EPFM), the plastic history is important both for both the plasticity in front of the crack tip and the residual stresses in the wake; this history must be accurately preserved even as the mesh is continually changing with crack growth. State variable mapping is a typical approach to preserving the history as the mesh changes. Critical element and node quantities are saved before the remeshing process starts. After remeshing is complete, these quantities are mapped onto the new mesh elements and nodes using the shape functions of both the old and new mesh. State variable mapping has been used extensively for other applications such as metal forming and multi-grid finite difference analyses. The specifics of state variable mapping will be elaborated upon in a later section.

The local remeshing and state variable mapping approach to EPFM has been combined with the nodal release technique and implemented in the FRANC2D/L program to provide a powerful and flexible tool to model elastic plastic crack growth. The nodal release technique is implemented such that crack propagation along lines of symmetry can be modeled for optimum mesh efficiency, and the local remeshing algorithms have been augmented with state variable mapping algorithms to allow fully automatic elastic plastic tearing without user intervention. In addition, the two algorithms can be combined to allow the nodal release technique along a predefined curving crack path. As an added benefit for flexibility, the local remeshing technique can also be used in a step-by-step mode, where the crack path is user specified. The following sections briefly describe each of the four variations on how elastic-plastic fracture can be modeled before continuing on with a more detailed description of the algorithms.

3.2.1 Nodal Release

Symmetry Edge Many analyses of laboratory specimens will have natural lines of symmetry that can be exploited during the analysis to reduce the mesh size by half or more. This option allows crack propagation along the edge of symmetry that follows a horizontal axis. Figure 3.1 is a schematic showing how lines of symmetry reduce the model size of a middle crack tension specimen to ¼ of the full specimen size. Symmetry boundary conditions along the vertical centerline of the specimen model the side to side symmetry. Since there is no cracking along the vertical centerline, these boundary conditions will not change during the analysis. Symmetry boundary conditions also exist along the crack face. The part of the crack face that is fully closed is held by fixity conditions that can be efficiently released as crack propagation becomes necessary. This form of crack propagation is commonly called the nodal release algorithm. In the current implementation, multiple symmetry cracks can exist and need not lie on the X axis, but they must all lie on a horizontal edge of the model.

Predefined Path Under some circumstances, users may know the crack path in advance (e.g. from experiments) and want to force the analysis to use that path in the most efficient manner. For this case, the nodal release algorithm can be applied for a predefined curving crack path. Figure 3.2 is a schematic showing nodal release along a predefined path. The crack has coincident node pairs on each side of the crack from the crack mouth to the crack tip. Coincident nodes are efficiently tied together in a manner similar to the symmetry edge method.

3.2.2 Local Remeshing and Mapping

User Specified Path Under some circumstances, users may want to monitor the crack tip state manually at each propagation step to extract response data to implement a custom direction criterion. In this case, the user can explicitly specify the crack path. State variables are mapped at each remeshing step to insure a correct nonlinear history for the yielded material.

Fully Automatic Propagation This option provides the user with automatic propagation. At each propagation step the crack growth direction is determined from a direction criterion, and the step size is user specified. Automatic remeshing algorithms extend the crack and update the mesh at the new crack-tip location. State variables are mapped at each remeshing step.

3.2.3 Algorithm Description

The capabilities desired – modeling elastic-plastic fracture with the level of flexibility described previously – led to two basic criteria for the implementation: relative simplicity for the user to specify a problem, and flexibility and simplicity in the internal database structure of the underlying software. These criteria were met by designing a unified data structure for the implementation and by establishing automated procedures to maintain the data structures in a manner transparent to the user.

However, the resulting implementation is still rather complex. All propagation algorithms revolve around the nodal release algorithm, since that implementation is used to monitor CTOD and other crack tip fracture criteria during the analysis. In addition, the nodal release algorithm is embedded within the nonlinear Newton solution scheme, since an efficient implementation of nodal release is intimately tied to the Newton scheme. However the remeshing algorithms significantly modify the mesh, and require that the system tangent stiffness matrix be rebuilt from scratch. Listing 3.1 shows the conceptual model for the automatic tearing algorithm without regard to how these capabilities are implemented. The steps are numbered only for clarity as part of this discussion.

```
1.  Initialize
2.  Begin analysis using current state
3.  Increment load/displacement BCs
4.  Find equilibrium
5.  Check before tearing. If detected:
        If unzipping, untie crack face nodes
        If remeshing, prepare to return for remesh
6.  Until total load
7.  Performed remesh if require
    7a. None required-done with tearing analysis
    7b. Save state for full mesh
    7c. For each crack tip:
            Delete locally
            Extend crack
            Add new mesh
    7d. End loop
    7e. Map saved state to new mesh
    7f. Return to equilibrium
8.  Until tearing analysis done
```

Listing 3.1: Steps of the automatic tearing algorithm.

Step 1 of the algorithm is initialization. This includes not only general initialization steps such as boundary conditions and analysis control data for the non-linear solver, but also initialization specific to the tearing algorithm. For instance, internal cracks that tear with remeshing require different user input for initialization than edge symmetry cracks that tear with nodal release.

Step 2 is to begin an analysis using the current state. This is an important conceptual consideration. The current state may be and initial non-loaded model or a restart state. A restart state may be the result of restart from a file, the result of a user request to view results, or the result of mapping algorithms after a request to grow a crack. From the perspective of resuming an analysis, each of these is considered equivalent.

Step 3 is to increment the load and displacement boundary conditions (BC). The current algorithm for incrementing the BC's is quite simple. A total user defined load increment is broken down into a linear distribution of sub-increments (also user defined). Equilibrium is established at each sub-increment. If sub-increments are too large, either the plasticity algorithm will fail or the Newton scheme will fail. In either case an error message indicates the nature of the problem. Automatic load stepping schemes are available in the literature (c.f. Crisfield, 1991) but are not implemented here. One exception is a simple, but effective predictor algorithm to track the fracture criterion and predict the load step fraction that allows the fracture criterion to be met (within a tolerance).

Step 4 is to find equilibrium at the current loading condition. This entails using the tangent stiffness matrix in the modified Newton iterative scheme. Appendix A provides a more detailed description of the finite element derivation and implementation.

Step 5 is to check if any of the current crack tips have a fracture criterion within tolerance of critical, and if so, take the appropriate action. In the case of nodal release cracks, the release is handled locally so that the analysis can continue uninterrupted. In the case of a crack tip that requires remeshing, the analysis is interrupted, and automatic remeshing is invoked (see Step 7).

Step 6 is presented as looping until total load has been exhausted. This is true for simple plasticity analyses without cracking, but for tearing the termination criterion is the number of crack propagation steps.

Step 7 is to perform remeshing if required. This step is executed after exiting the loop over steps 3-6, where the exit condition could be any one of several conditions, including an error condition or a request that remeshing take place.

Step 7b is to save the state of the analysis for the full mesh. This step is part of the state variable mapping process.

Step 7c is the remeshing process, where for each crack tip the mesh is deleted locally to the crack tip, the tip is extended, and a new mesh is created and added around the tip.

Step 7e is to transfer the state saved in step 7b onto the new mesh using the state variable mapping routines.

Step 7f returns the newly mapped state to equilibrium. The state was mapped onto a new geometry that has new crack surface area. Consequently, the compliance of the structure will have changed. In addition, mapping errors are introduced as a result of approximations in the mapping process. Both of these effects are somewhat accounted for by returning the state to equilibrium before resuming the analysis. (Mapping errors are discussed in Chapter 4.)

Step 8 simply indicates that the analysis will continue until the tearing is complete. As indicated in *Step 6*, the user specified maximum number of propagation steps controls analysis termination.

3.2.4 Nodal Release Implementation

The nodal release mechanism uses stiff springs to efficiently model crack growth for cases where the crack is growing along a symmetry edge or along a predefined path. Figure 3.1 is a schematic that shows the conceptual model for the nodal release mechanism. Stiff springs provide forces to hold coincident nodes together (or to provide zero displacement, in the case of symmetry edge). When the crack tip fracture criterion is met, the stiff springs at the tip are removed from the problem and corresponding crack face forces can be relaxed, while holding all other boundary conditions constant.

Since the stiff springs are effectively part of the mesh, in the most general implementation the full stiffness would need to be re-formed and re-factored. However, an implementation by Newman (1974) can efficiently remove the springs from the stiffness matrix in its inverted form without re-factoring. The algorithm is based on a modified Cholesky algorithm and greatly enhances the efficiency of the nodal release algorithm.

The value of the spring stiffness constant is an important consideration. The effect of the stiff springs is to enforce a penalty function for the equations of the global system corresponding to the nodal displacements. The ideal effect would be to add the stiff spring before propagation and remove the stiff spring after propagation without effect on the global stiffness matrix. In practice, the value of the stiff spring needs to be large enough that the stiffness due to all other elements framing into the node is insignificant compared to the stiff spring value. However, when the stiff spring is subtracted out of the inverted stiffness matrix, the original global stiffness coefficients must be recovered. Since all operations are performed in double precision, there are about 15 significant digits available. For example, if a coefficient has a value of 1.0E4 and the stiff spring with a value of 1.0E10 is an added, then subtracted from the coefficient, about six significant digits will be lost and about 9 accurate significant digits will be retained. Ideally the springs stiffness would be determined as a function of the global stiffness matrix. In the current implementation a constant K_s=1.0E4 is used.

3.3 Crack Tip Constraint Model

Stress triaxiality is a significant issue at the tip of a crack, even for thin sheet material. This stress triaxiality, or constraint, has received much attention, but still few models exist to describe constraint in a two-dimensional analysis. Plane stress has no constraint, and plane strain allows the constraint to extend too far away from the crack tip.

Newman et al. (1993a) describes constraint as a buildup of stresses around a crack front due to the resistance against in-plane and out-of-plane deformation. In-plane constraint is mainly associated with the closeness of the crack front to external boundaries, and out-of-plane constraint is mainly influenced by plate thickness. While in-plane constraint is an important fracture issue, from the perspective of residual strength in-plane constraint is less of immediate concern, since in many cases, only a small amount of crack growth may be necessary before a structure experiences maximum load. In addition, by the time the crack is being significantly influenced by an external boundary, fracture may be controlled more by the stress-strain behavior of the material and net-section yielding in the remaining ligament. Out-of-plane constraint, on the other hand, can have significant effects on the fracture behavior and residual strength of structures very early in the tearing history, before the maximum load is reached.

Anderson (1995) describes out-of-plane constraint relative to an uncracked plate subjected to in-plane loading. With no crack, the plate is in a state of plane stress. If the plate has a small through-crack perpendicular to the load somewhere far from all boundaries, the material far from the crack is still in a state of plane stress. The stresses are elevated near the crack tip, and these elevated stresses cause a Poisson effect along the crack front, causing the material to contract; the surrounding material resists the contraction, resulting in out-of-plane stresses along the crack front. That is, the crack is in a triaxial state of stress, while the material far from the crack is in a biaxial state of stress.

Figure 3.3 shows a schematic of how the stresses and strains vary along the crack front. On the interior of the crack, the material sees effectively a state of plane strain. Where the crack intersects the free surface, the material is in a state of plane stress. A transition region exists near the free surface where the material is neither plane stress nor plane strain. As the material around a crack front yields, the stress state will vary along the crack front from plane stress at the free surface, to some amount of triaxial state at the mid-plane of the crack. Once the plastic zone size reaches approximately half of the material thickness, the stress state is predominantly plane stress in the yield region, except for very near the crack front.

There are a number of ways to characterize constraint (Newman et al., 1993a). One simple way is to look at the out-of-plane stress near the crack front. Figure 3.4 shows the normalized Z stress as a function of position in front of the crack at the mid-plane of the specimen. The figure shows that the Z stress, and thus constraint, decreases rapidly to zero in less than 1/2 of the thickness of the material.

Newman et al. (1993a) used three-dimensional elastic-plastic finite element analysis to investigate the constraint along a stationary crack front. Newman's results showed that even under large-scale plastic yielding, local constraint developed in the interior regions near the crack even for the thinnest material investigated (B = 1.25 mm).

3.3.1 Constraint and Residual Strength

Early attempts to simulate residual strength with plane stress or plane strain analyses were unsuccessful. Fracture parameter values "tuned" to match residual strength for a middle-crack tension specimen would not match analysis results for a compact tension specimen. The reason for the inconsistent analysis results was inability of either a fully plane stress or fully plane strain model to capture both the plane stress state away from the crack and triaxial stress state near the crack.

There are number of different ways to simulate out-of-plane crack tip constraint in a two-dimensional analysis. Shan et al. (1992) uses either three-dimensional analysis or experimental results as a baseline, and correlates plane stress and plane strain results to get a two-dimensional approximation to the three-dimensional problem. The correlation is performed by running both plane stress and plane strain analyses, then using a linear combination of the two, assuming that a fraction of the thickness B_s/B is in plane stress and that the remainder of the thickness is in plane strain $(1-B_s/B)$ (B_s is the thickness of the plane stress section, and B is the total thickness). The approach produces reasonable results, but requires two analyses, with superposition after the fact. Shan et al. (1994) showed that his approach is somewhat independent of specimen size; however, his work was for straight cracks. It is unclear how the work would translate to mixed-mode behavior and whether the approach is specimen independent.

Newman et al. (1988) introduced a mixed state of stress, commonly called the plane strain core, to capture the constraint at the crack tip. Figure 3.5 is a schematic of the plane strain core concept illustrating Newman's mixed state of stress. Plane stress elements are used for the entire model, except along the crack face and in front of the crack tip, which are modeled with plane strain elements. The plane strain core has been used to accurately predict residual strength for C(T) and M(T) specimens with the nodal release algorithm (Newman et al., 1988; James, 1997). FRANC2D/L has this plane strain core capability for nodal release fracture simulations.

Newman's plane strain core did not evolve as the crack grew because the core was fixed in front of the crack line. The predefined core works well for problems for which the crack path is known in advance. However, when the crack path is not known *a priori*, the region of high constraint must move with the crack tip. In the three-dimensional analysis the constraint develops naturally near the crack as part of the analysis.

3.3.2 Constraint and the Remeshing Model

When the nodal release mechanism is used to simulate fracture the mesh *does not* change during crack growth. As result, a constant height plane strain core can be "tuned" to model the constraint at the crack tip, and the core can be predefined in the mesh. When the remeshing-mapping crack growth mechanism is used to simulate fracture the mesh *does* change during crack growth. Since the crack path is not known in advance, the plane strain core cannot be predefined and must grow as the crack grows. Two sets of issues surround implementing a growing plane strain core: those related to representing the geometry of the core, and those related to the underlying continue mechanics. The implementation of a solution to these issues is not within the scope of this work.

3.4 Simulating Multi-Site Damage

One cracking phenomenon of particular concern to the aircraft industry is the residual strength of the structure in the presence of multi-site damage (MSD). MSD cracking involves two or more cracks that can ultimately interact to influence each other's behavior and the behavior of the overall structure. Two perspectives must be considered when simulating multi-site damage: the nodal release algorithm and the remeshing-mapping algorithm.

3.4.1 Nodal Release MSD Model

Multi-site damage in the context of the nodal release algorithm is conceptually simple. The nodal release approach ties nodes along an edge model. Figure 3.6 shows a schematic of an M(T) specimen with a main "lead" crack and MSD in front of the lead crack. All of the nodes along the bottom edge of the model were initially tied. Next, the lead crack was specified, which untied nodes from the middle of the specimen to the tip of the lead crack. Finally, nodes were untied at the specific locations of the MSD in front of the lead crack.

As the analysis progresses, all of the tips will be checked for the fracture criterion, and nodes released as appropriate to allow crack growth along the crack face. The criterion for merging two cracks, such as two MSD cracks, or the lead crack and MSD crack, is simply that when only one node remains between two cracks, that node is released automatically, and the cracks are merged. Figure 3.6 also shows schematically the case where two MSD cracks are ready to merge. Only two nodes remained tied. When either of the two tips reaches the critical fracture criterion, the node at that tip will be released, leaving only one node attached between the two MSD cracks. When only a single mode remains that node is released automatically.

3.4.2 Remeshing-Mapping with Multiple Cracks

When remeshing is used, the situation is somewhat different. Since the crack path is not predefined, the geometry ahead of each crack tip must be detected and handled robustly within the algorithms. Several possible situations are:

> ***Tip Approaching Tip.*** This fairly general situation has the previous M(T) example in Figure 3.6 as a special case. Figure 3.7 is a schematic of the situation for the remeshing analysis. In general the situation arises when two tips are close enough that the ligament between them fails.
>
> ***Tip Approaching Crack Face.*** In an analysis with curving cracks this situation is probably most likely. A classic example is the "football" formed by two fatigue cracks approaching, then repelling one another, then merging by intersecting the crack face. Figure 3.8 is a schematic of this type of crack coalescence.
>
> ***Tip Approaching Boundary.*** During some fracture scenarios, it may be possible for a crack to approach and intersect an outer boundary of the model before residual strength is reached. This condition is a concern because the current implementation does not allow multiple bodies (full fracture into two or more pieces).

In the current implementation each of these situations is handled uniformly and simply, but not automatically. The algorithm does detect automatically when a tip approaches the boundary. At that point control is returned to the user. Manual remeshing procedures can be used to extend crack tips manually, or to delete elements to manually coalesce cracks. Manual mapping procedures can be used to retain the plasticity state and allow restart of an analysis.

3.4.3 Load Relaxation

When simulating MSD problems there are multiple crack tips. Any of these crack tips is free to grow during an increment in the boundary conditions. Under some circumstances more than one may grow during this increment. When the remaining ligament between two tips is small, the two tips can grow together, breaking the ligament. Under these circumstances intermediate equilibrium states are recorded as the cracks are growing, preserving the plasticity history and extension state for each of the growing cracks. A load relaxation scheme is used, whereby the forces holding the crack closed before growth are slowly relaxed over ten steps, while holding the boundary conditions constant. If during the load relaxation process load redistribution causes additional crack tips to meet the fracture criterion, the crack face loads at those tips are also relaxed over ten steps. The equilibrium iterations for relaxation continue until all crack face loads are expended and no more tips meet the fracture criterion.

3.5 Summary

This chapter described two fundamentally different approaches to elastic-plastic crack propagation: nodal release and automatic remeshing with mapping. The two approaches have been implemented in the FRANC2D/L code. The algorithms have been implemented to model elastic-plastic fracture under a number of different circumstances. The nodal release algorithm is specialized to work for either of two different situations: cracking along an edge symmetry or cracking along a predefined curving crack path. The automatic remeshing algorithm can be used either in a step-by-step manual mode or in fully automatic mode. In fully automatic mode the direction is predicted from maximum tensile stress at the crack tip. Crack tip constraint can be modeled during nodal release using the plane strain core. Specialized algorithms allow multi-site damage during nodal release. Manual remeshing and mapping can be used to merge MSD crack tips when automatic propagation is interrupted by crack tips in close proximity to one another. The algorithms implemented are flexible and powerful and can be applied in a wide variety of situations.

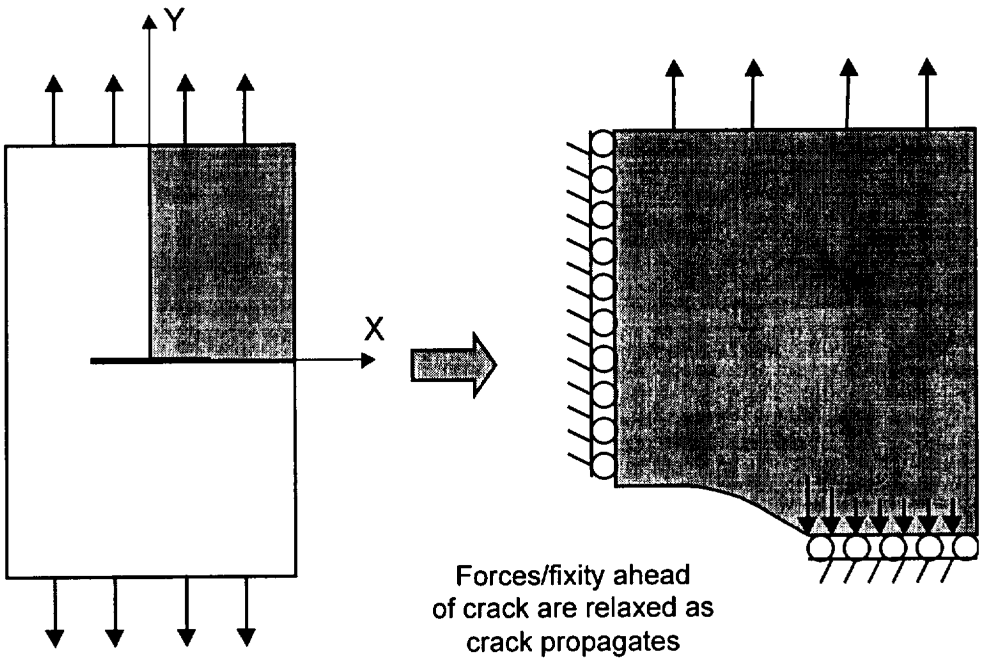

Figure 3.1: Schematic showing lines of symmetry for a middle crack tension specimen. During elastic-plastic fracture, fixity maintain symmetry along the vertical edge, and special stiff springs maintain symmetry along the fracture surface.

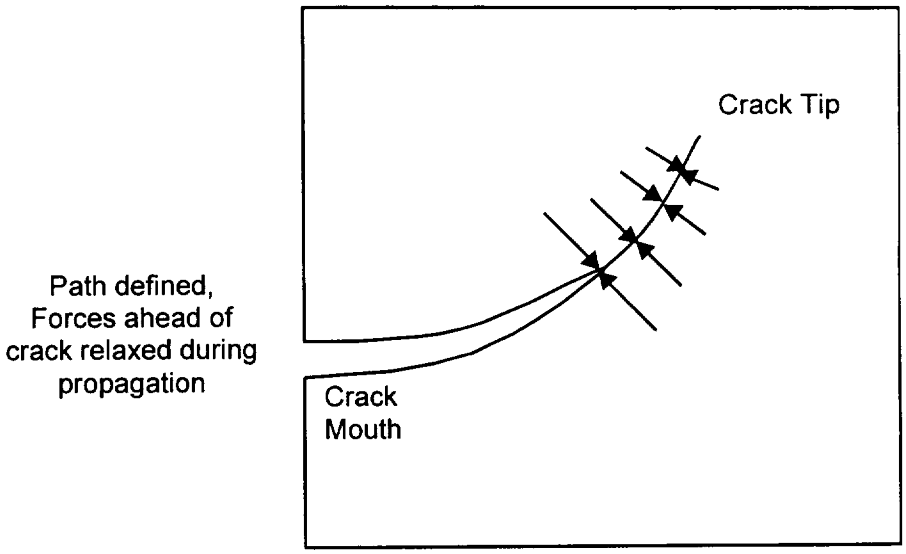

Figure 3.2: Schematic showing crack face forces for a nodal release fracture simulation with the crack path predefined. Crack face forces are maintained by special stiff springs.

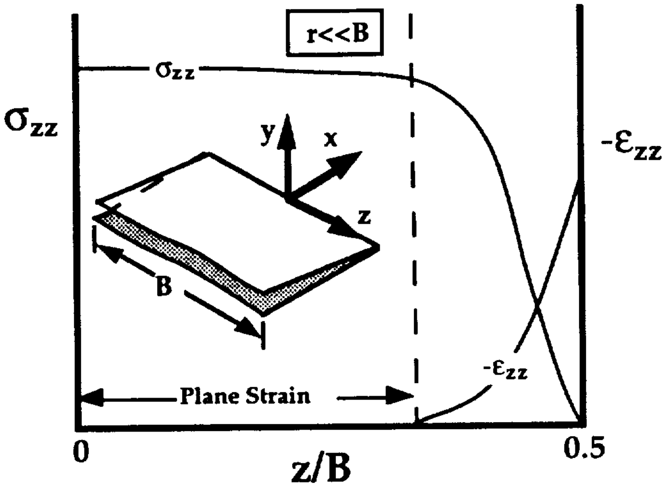

Figure 3.3: Schematic showing the variation of stress and strain along a three-dimensional crack front (Anderson, 1995).

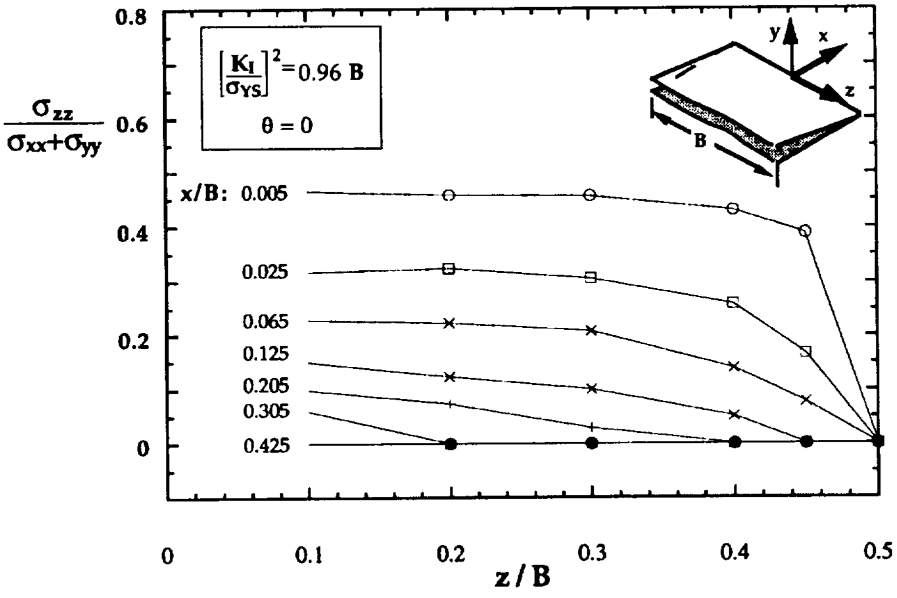

Figure 3.4: Normalized out-of-plane stresses in front of a three-dimensional crack indicate the level of constraint in front of the crack (Anderson, 1995).

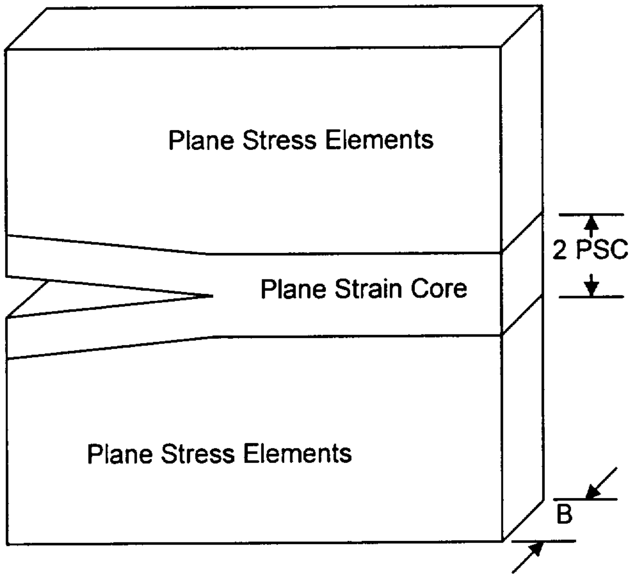

Figure 3.5: Plane strain core concept.

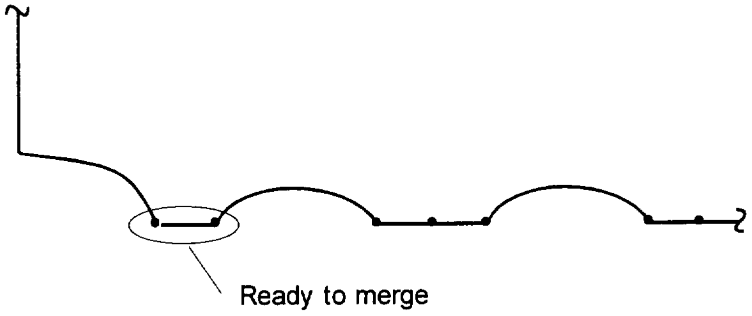

Figure 3.6: Crack tip coalescence for a symmetry model. Multi-site damage configuration with tips ready to merge when criterion at either tip reaches critical.

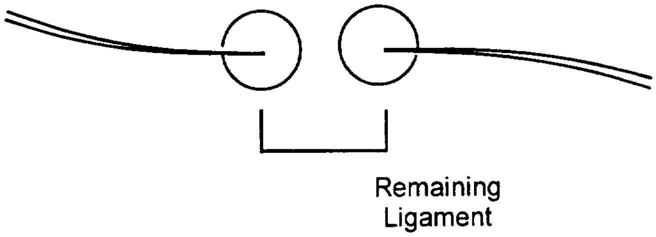

Figure 3.7: Schematic of Tip Approaching Tip. Circles represent minimum radius for automatic propagation to continue.

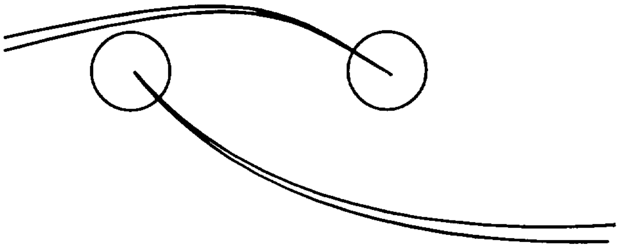

Figure 3.8: Schematic of Tip Approaching Boundary. Circles represent minimum radius for automatic propagation to continue.

Chapter 4

State Variable Mapping

The elastic-plastic constitutive equations are nonlinear and history dependent. For the finite element method, state variables are stored at the gauss points of each element to represent this history dependence. Typical state variables may include the stresses, hardening parameters, work variables, and yielding flags. After remeshing takes place, the state variables must be accurately transferred from the old mesh to the new mesh to retain the history information. In addition, nodal displacements must be transferred from the old node locations to the new node locations.

4.1 Mesh Mapping

This process of transferring state variables from one mesh to another is typically referred to as mesh mapping. Mesh mapping techniques are discussed in finite element literature for fracture simulations (Lim et al., 1992; Kato et al, 1993), as well as metal forming process simulations (Ponthot and Hogge, 1991; Sekhon and Chenot, 1993), welding processes (Brown and Song, 1993), and in more general settings (Chavez, 1983). Four references that address issues concerned with mapping large strain response data are Ponthot and Hogge (1991), Kato et al. (1993), Yamada (1993), and Espinosa et al. (1996). Kato et al. (1993) note that accuracy of the displacement mapping is especially important "when using the total Lagrangian formulation, since the initial geometry must be correctly recovered from the deformed geometry using the mapped displacements." Since this work is only concerned with small strain and small geometry changes, these large strain issues will not be addressed further.

The displacement mapping problem can be viewed as the process of transferring displacements from an old mesh on the current volume to a new mesh on the current volume:

$$U_o(V) \rightarrow U_n(V), \qquad (1)$$

where V is the current volume in time, and U_o and U_n are old and new displacements corresponding to the old and new mesh nodal coordinates, X_o and X_n. And so, the mapping problem can be summarized as:

Given U_o, X_o and X_n,

Find U_n.

By direct extension, the process can be applied to any nodal response variable.

Several methods of transferring state variables between old and new meshes are discussed in the literature. Lim (1992) summarizes the methods in three categories: smoothing techniques, triangulation, and inverse isoparametric mapping. The state variable mapping algorithm implemented for this work is the inverse isoparametric mapping method.

4.2 Inverse Isoparametric Mapping

Isoparametric elements use the same shape functions to interpolate the nodal coordinates and the nodal response data:

$$X_o = \sum_i N_i(r,s) \cdot X_o^i\,, \tag{2}$$

$$U_o = \sum_i N_i(r,s) \cdot U_o^i\,. \tag{3}$$

where N_i are the shape functions evaluated at the element natural coordinates (r,s), and X_o and U_o are nodal values of coordinates and displacements, respectively. For the inverse mapping problem, given the coordinates of a node in the new mesh, find the natural coordinates in the old element, such that interpolation in the old element gives the coordinates of the new node. That is: Given X_o and X_n, the nodal coordinates, find (r_n,s_n) such that

$$X_n = \sum_i N_i(r_n,s_n) \cdot X_o^i\,. \tag{4}$$

Then (r_n,s_n) can be used to interpolate the nodal response data from the old mesh into the new mesh:

$$U_n = \sum_i N_i(r_n, s_n) \cdot U_o^i \,. \tag{5}$$

Equation (4) is a nonlinear equation in (r,s) which cannot be solved directly.

To solve Equation (4), Lim (1992) uses a predefined line technique, where a line is drawn across the element through the point where the natural coordinates are desired and to one of the nodes on the element. The natural coordinates are found iteratively by using a resulting set of simultaneous equations. The solution is straight forward for straight sided elements, but for curved sided elements many special cases exist. But when correctly implemented, Lim (1992) reports that the algorithm is robust and efficient.

The current implementation uses the method of Kato et al. (1993), where the shape function derivatives are used in a simple Newton method iterative algorithm. For straight-sided elements the algorithm converges rapidly and is quite accurate, and no special provisions are necessary for curved elements, should they become necessary in the future. The Newton method has the added benefit that it was already implemented and well tested in FRANC2D/L (used primarily for post-processing purposes in line plots of response data).

4.3 Stress Mapping

As previously mentioned, the inverse isoparametric mapping algorithm can be used to map any nodal response variable. Stresses and other element based response data must be mapped from gauss points in the old mesh, to gauss points in the new mesh. To accomplish this several steps are necessary:

1. Gauss point global coordinates are evaluated and saved for gauss points in the new mesh using the gauss point natural coordinates.

2. Gauss point response data from the old mesh are extrapolated to the element nodes using a least squares fit of the gauss point data to a plane.

3. The inverse mapping procedure outlined above is then used to map extrapolated stresses from the old nodes to the new global gauss point locations saved in step (1).

4.4 Element Variables Mapped

In addition to the stresses (σ_{xx}, σ_{yy}, σ_{xy}, σ_{zz}), several other gauss point state variables are mapped after remeshing:

`YieldStress` - this value is the current radius of the von Mises yield surface.

`TotalWork` - this is a numerical evaluation of the work integral using the trapezoidal rule:

$$W_t = \int_0^{\varepsilon} \sigma d\varepsilon \tag{6}$$

`PlasticWork` - similarly, this is the plastic component of work:

$$W_p = \int_0^{\varepsilon_p} \sigma d\varepsilon_p \tag{7}$$

Two of the element gauss point variables are calculated rather than mapped. These are logical flags indicating yield state at the gauss point:

`EverYield` - indicates whether the gauss point has ever yielded as part of the analysis.

`IsYielding` - indicates whether the gauss point is currently yielding.

Since these two state variables have discrete, logical values, they cannot be mapped. At each gauss point they are reevaluated from the current mapped stress state, the current yield surface radius, and initial yield surface radius. Using the nomenclature from above:

```
EverYield = (YieldStress/YSinit) >= 1.02

IsYielding = (SigE/YieldStress) > 0.99
```

Where `YSinit` is the initial radius of the yield surface before hardening, and `SigE` is the von Mises stress evaluated at the current gauss point stress state.

4.5 Accuracy of the Mapped Data

There are a number of factors that influence the accuracy of the mapped data. The primary factor is the mesh quality. Element quantities are extrapolated to nodes, but element contributions at a node are not averaged. Thus, stress discontinuities across element boundaries may exist as a result of inadequate mesh density. Averaged nodal values might tend to average out local stress discontinuities; however, local stress gradients may be misrepresented. Given the importance of mesh quality on the overall solution, this is probably not a primary concern. That is, if the mesh is not fine enough to accurately capture stresses across element boundaries, errors in the mapping results are only contributing to a much larger problem.

Another possible error in the mapped data is the relationship between the stress state and the yield surface consistency condition for a gauss point that is currently yielding. The yielding flags are discrete values that cannot be interpolated, so it is not possible to determine if a point is yielding without assuming that the mapped stress state and yield surface radius are consistent. Since the `EverYield` and `IsYielding` flags are only used for displaying purposes, they are evaluated from the mapped state directly, assuming that the mapped state is consistent.

No special measures are taken to check for the consistency condition or for possible errors in the stress-strain compatibility other than to re-establish equilibrium in the new configuration after the mapping has completed. Typically, this new configuration will have new surface area after fracture propagation. Since equilibrium is always re-established at the current load and displacement level, this results in stress reduction and redistribution as a result of the compliance change in the structure, and a somewhat different stress state than before the mapping. Numerical experiments have shown that with a quality mesh, no problems occur. Habraken and Cescotto (1990) report similar findings.

Figure 4.1 through Figure 4.3 provide a qualitative assessment of the mapping errors by comparing color contours of stress. The (a) figure shows the stress component and deformed mesh just before crack propagation. The (b) figure shows the stress component and the same view of the mesh just after mapping, but before equilibrium has been restored. The differences in the stress are a direct result of the remeshing and mapping process. The figures show that overall quality of the mapped data is good. The largest differences appear to be in the vicinity of the original crack tip location (a).

4.6 Algorithm Efficiency

Other than solving the nonlinear equilibrium equations, the mapping algorithm is potentially the most computationally intensive algorithm. For simplicity sake, the initial implementation mapped the response for all nodes and elements. However, the efficiency suffered. For a typical tearing analysis slightly less than $^1/_3$ of the total analysis time was spent in the mapping algorithm.

Consequently, the algorithm was modified to only map for the new nodes and elements created during the remeshing process rather than for the entire mesh. Data for other nodes and elements is preserved exactly. Further, the algorithm was modified such that the search set in the old mesh was limited only to nodes and elements in the remesh region. The result is very good performance. For a problem with 6801 nodes and 3288 elements, the nonlinear solution time for the first crack propagation step is about 1:59 (mm:ss). Table 1 shows remeshing and mapping times for the original *Full* mapping algorithm, the *Intermediate* algorithm that mapped only for new nodes and elements, and the final *Optimized* algorithm that additionally limits the search set to the nodes and elements in the mapping region.

The number of nodes mapped in this example was 40, and the number of elements mapped was 58. It is clear that the algorithmic changes had a dramatic effect on the efficiency of the algorithm. Since the mapping time is now on the same order as the remeshing time and is a small fraction of the total analysis time, the algorithm is deemed efficient enough.

Table 4.1: Comparison of Mapping Algorithm Times (Analysis time: 1:59)

Algorithm	Mapping time	Mapping/Analysis
Full	1:51	93.3%
Intermediate	0:09	7.6%
Optimized	0:03	2.5%

A second order effect on algorithm run-time is the search algorithm for points contained in an element. When nodes are mapped from the old mesh to the new mesh, the first step is to locate the element in the old mesh that contains a point from the new mesh. A number of algorithms are available for solving this problem (Lim, 1992); however, the algorithm implemented is quite simple. First we search linearly through the list of elements and check whether the point lies within the bounding box of each element. For points within the bounding box of element, the scan line algorithm is used to determine if the point lies within the element itself.

One additional improvement that was not implemented may improve the mapping efficiency further. When mapping element gauss point data, each element in the new mesh contains several gauss points in close proximity. Rather than searching the entire old mesh for each of the gauss points in element from the new mesh, the search could be performed only for the first gauss point, then for subsequent gauss points local topology of the old mesh can be used for local search, rather than searching the entire mesh. This would exploit the fact that all of the gauss points for an element in the new mesh will probably lie within the boundaries of a single element in the old mesh, or possibly within a small group of elements in the old mesh.

4.7 Summary

State variable mapping provides a means for maintaining the plastic history of an elastic-plastic analysis as the mesh changes during crack propagation. The inverse isoparametric mapping algorithm has proven robust, accurate, and efficient.

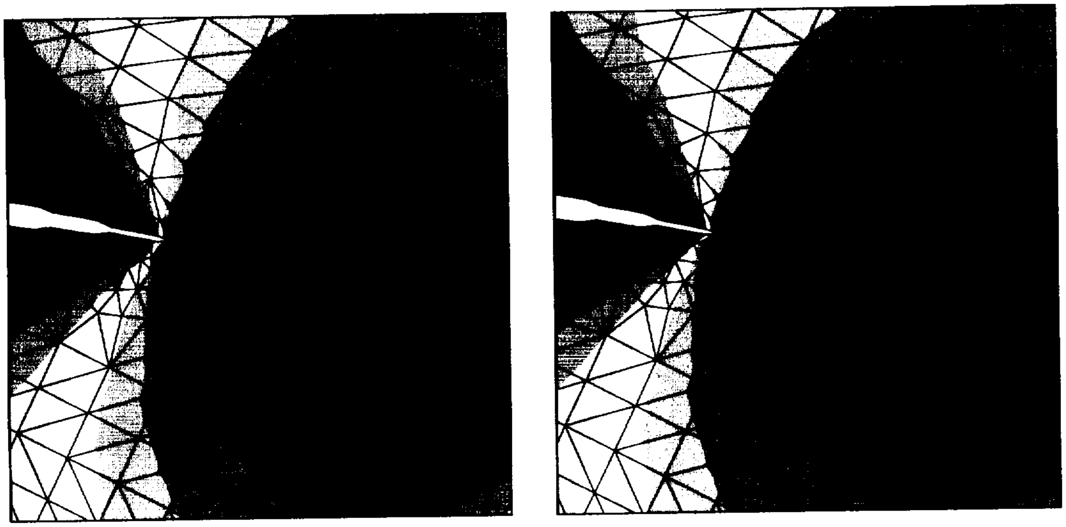

Figure 4.1: Qualitative mapping error assessment. Component: Maximum principal stress. (a) just before crack propagation, (b) just after crack propagation, remeshing and mapping, but before equilibrium has been restored.

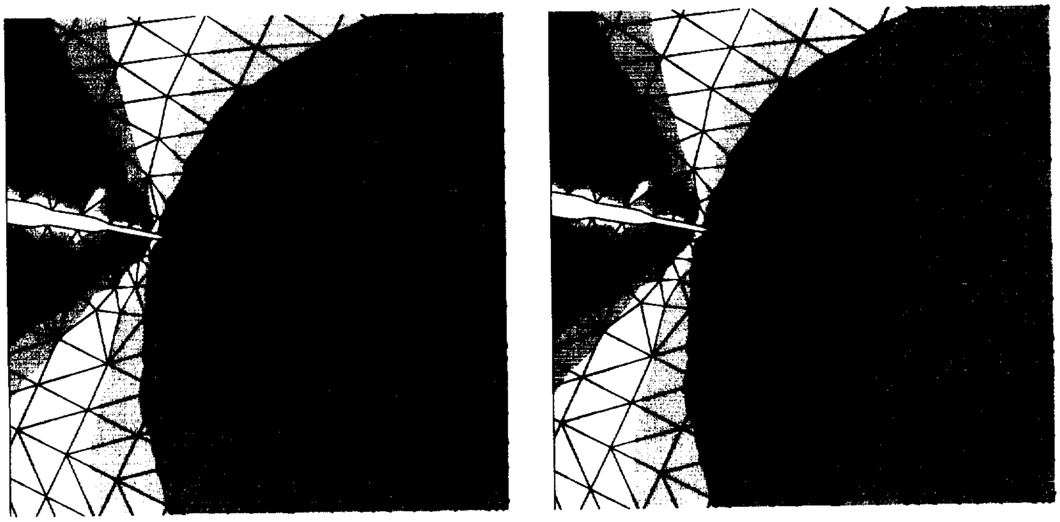

Figure 4.2: Qualitative mapping error assessment. Component: Effective (von Mises) stress. (a) just before crack propagation, (b) just after crack propagation, remeshing and mapping, but before equilibrium has been restored.

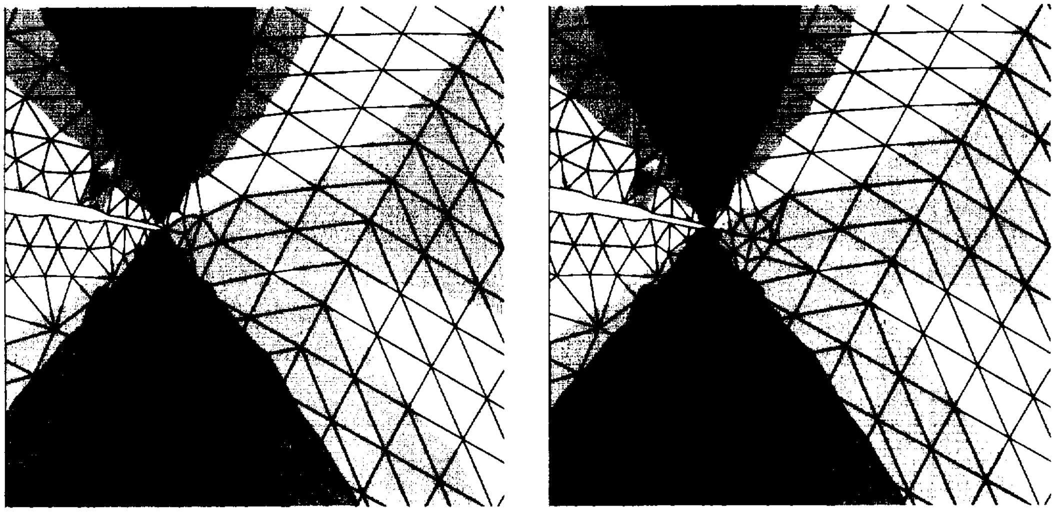

Figure 4.3: Qualitative mapping error assessment. Component: Shear stress. (a) just before crack propagation, (b) just after crack propagation, remeshing and mapping, but before equilibrium has been restored.

Chapter 5

Fracture Analyses Using Nodal Release

Two fundamentally different algorithms are available for elastic-plastic fracture simulations in FRANC2D/L: one is designed for efficiency when the fracture occurs along a plane of symmetry in the model, and the other is designed for generality when fracture is not on planes of symmetry and may involve curving cracks. This chapter presents analysis results for the former of these two and compares these results with experimental data and three-dimensional analysis results.

The first section of this chapter describes some background information for the analysis such as material data, a simple mesh convergence study, and information about how three-dimensional analysis is used as a baseline for comparison. The remainder of this chapter is devoted to residual strength analyses and their comparison with experimental data and three-dimensional analyses.

Two standard fracture specimens are considered: the M(T) (middle crack tension) and the C(T) (compact tension) specimens. These specimens were considered primarily because of availability of test data and past analysis experience. First, the plane strain core (PSC) height necessary for an accurate residual strength simulation of a 6.0 inch wide C(T) specimen is determined. Second, the PSC is verified by comparing analysis predictions with experimental data for a 24 inch wide M(T) specimen. This value of the plane strain core was then used in all subsequent analyses. Third, the software is used for analysis predictions of residual strength for both C(T) and M(T) specimens to show a degree of specimen independence, first for configurations with a constant crack-length to specimen-width, then for configurations with constant specimen width and different crack lengths. Next, a series of Multi-Site Damage (MSD) calculations demonstrate multiple growing cracks with linkup, and show the effects of MSD on residual strength. Finally, the effects of specimen thickness on core height is explored.

5.1 Analysis Background

The fracture analyses presented here use the CTOA fracture criterion. All of the simulations are Mode-I only; a direction criterion is not necessary because symmetry is exploited and the nodal release algorithm is used. Figure 5.1 is a schematic of the M(T) test specimen. Only ¼ of the specimen need be simulated (symmetry along the centerline and fracture surface). The fracture surface symmetry is maintained by the nodal release algorithm. Figure 5.2 is a schematic of the C(T) test specimen. Similar to the M(T) specimen, the nodal release algorithm maintains the fracture surface symmetry boundary condition.

5.1.1 Analysis Material Parameters

For all of the analyses in this chapter the material considered is 2024-T3 with cracks oriented in the LT direction (loading parallel to the rolling direction, cracking perpendicular to the rolling direction). Table 1 shows the analysis material properties for all analyses in this chapter (unless otherwise specified), and Table 2 shows the uniaxial stress-strain data for 2024-T3 used in the von Mises yielding algorithm. The critical CTOA value was determined by Dawicke and Newman (1997) by using three-dimensional finite element analysis and comparing failure analysis results with test results. This critical value is within the scatter band of experimental CTOA data for 2024-T3.

Table 5.1: Analysis Material Properties

Young's Modulus	10350 Ksi
Poisson's Ratio	0.3
Thickness	0.09 inch
Yield Stress	50 Ksi
$\mathrm{CTOA_c}$ @ 0.04"	5.25 deg

5.1.2 Mesh Size Convergence Study for Tearing

The CTOA algorithm implemented in FRANC2D/L allows the crack to advance one or more element lengths when the angle made by points on the upper and lower crack surfaces at a distance $d = 0.04$ inch behind the crack tip reached a critical value. The 0.04 inch distance was selected based on previous analysis experience (Newman et al., 1993b) and on mesh convergence studies (Dawicke, 1996). Figure 5.3 shows results of a simple FRANC2D/L convergence study, where the number of elements along the crack face was increased, while the critical CTOA was measured at a fixed distance behind the crack tip ($d = 0.04$ inch). The results are compared with similar results from a ZIP2D convergence study (Dawicke, 1996) (the FRANC2D/L results are for linear strain six-noded isoparametric elements (T6); the ZIP2D results are for constant strain triangles (CST)). The variation in FRANC2D/L results is less than 1% for all three-mesh densities, thus a minimum element size of 0.04 inch on the crack face is deemed acceptable.

Table 5.2: Uniaxial stress-strain yielding curve

Stress (Ksi)	Strain
0.0	0.0
50.0	0.00483
56.5	0.015
62.5	0.04
68.5	0.1
71.0	0.16
71.0	0.2

5.1.3 Three-Dimensional Analyses

While a wealth of 2024-T3 data is available for M(T) and C(T) specimens, most of this data is for only one thickness, and only for limited initial a/W crack ratios. Dawicke and Newman (1998) have shown that three-dimensional analysis is capable of accurately representing fracture behavior of thin-sheet material for a wide range of specimen sizes and for more than one specimen type. So in addition to experimental data, three-dimensional analyses are used as a baseline for comparison with the two-dimensional plane stress, plane strain, and plane strain core analyses produced with FRANC2D/L. The three-dimensional code is ZIP3D (Shivakumar and Newman, 1990), and Dr. David Dawicke at NASA Langley Research Center provided the three-dimensional results (Dawicke, 1997).

5.2 Constraint Model

Two advantages of two-dimensional analysis over full three-dimensional analysis are efficiency and simplicity. However, with simplicity comes the inability to capture certain behavior such as variable through-thickness stress triaxiality, which can be modeled using three-dimensional analyses. Stress triaxiality is a significant issue at the tip of a crack, even for thin sheet material. This stress triaxiality, or constraint, has received much attention, but still few models exist to describe constraint in a two-dimensional analysis. As previously discussed, plane stress has no constraint, and plane strain introduces too much constraint, allowing the plane strain triaxiality to extend too far away from the crack tip. Newman et al. (1988) modeled constraint as a simple mixed state of stress with plane strain elements near the tip and plane stress elements away from the tip. Figure 5.4

is a schematic of the plane strain core (PSC) concept illustrating Newman's mixed state of stress. Analyses in this chapter denoted PSC core use the mixed state of stress and include an indication of the core height.

5.2.1 Plane Strain Core Height

Different material thicknesses and different test specimens have different levels of constraint, and the height of the PSC can be adjusted to introduce an appropriate level of constraint for a given material, thickness and test specimen. For the purposes of this chapter, the PSC height was selected by matching the failure load of the two-dimensional PSC analysis with test results for 6.0 inch wide C(T) specimens (crack length of a/W = 0.4). Analyses were run for PSC heights of 0.02, 0.04 and 0.06 inches. Using linear interpolation, the core height that matched the test results was 0.042 inches. Figure 5.5 shows a comparison of plane stress, plane strain, and plane strain core results with the experimental and three-dimensional results for load against crack extension. The plane stress results over-estimated and plane strain results under-estimated the failure load. In addition, the crack extension at failure is over-estimated by plane stress and under-estimated by plane strain. The plane strain core results closely match the three-dimensional results, and represent a good approximation to the test results.

Similar analyses were run for 12.0 inch wide M(T) specimens with a crack length of 2a/W = 1/3 and plane strain core heights of 0.02 and 0.04 inches. Also using linear interpolation, the core height that matched the three-dimensional M(T) results was 0.034 inches.

5.3 Geometry and Specimen Independence

A necessary condition for a valid fracture criterion is that it be applicable independent of specimen type. The critical CTOA fracture criterion is relatively independent of test specimen configuration and crack configuration for constant thickness test specimens (Dawicke and Newman, 1998). Since the PSC is an analysis mechanism introduced to approximate crack-tip constraint, it too must be independent of specimen type and configuration to be widely applied as a valid analysis approximation. In this section, the PSC height determined for the 0.09" thick, 6" wide C(T) specimen is used to predict the behavior of other C(T) and M(T) configurations. All analyses were run using a plane strain core height of 0.04 inches for convenience. A single core height demonstrates that a core height tuned with one laboratory specimen, can be used to accurately predict the behavior of other specimen configuration and other specimen types.

Figure 5.6 shows a comparison of plane stress, plane strain, and plane strain core results with the experimental and three-dimensional results for load against crack extension for a 24.0 inch wide M(T) specimen. As with the 6.0 inch wide C(T) specimen, the plane stress results over-estimated and plane strain results under-estimated the failure load. The plane strain core results more accurately model the fracture behavior, over predicting the experimental average by about 7%.

A valid fracture criterion must be independent of specimen configuration. Figure 5.7 shows predictions of failure load against specimen width for two-dimensional PSC analyses compared to three-dimensional analysis results for C(T) specimens with constant thickness and a/W ratio. The plane strain core analyses accurately predicted the failure load for the three largest specimens. A 15% difference in the failure load was observed between the two-dimensional and three-dimensional analyses for the 2.0 inch wide C(T) specimen. Results indicate the failure of the two inch C(T) specimen is controlled by net section yielding, rather than controlled fracture.

Figure 5.8 shows failure stress against specimen width for M(T) specimens with constant thickness and a/W ratio. The results show that the plane strain core can predict failure with reasonable accuracy for these specimens as well. For the smallest specimen width, the PSC results under-predict the three-dimensional analysis results by about 3%, and for the largest specimen width they over-predict by about 3%.

Figure 5.9 shows predicted failure load against initial crack length for C(T) specimens with constant thickness and width. The PSC results agree with the three-dimensional calculations for all crack lengths. Of the three a/W ratios considered, the PSC results for a/W = 0.3 over-estimate the three-dimensional results by 3%; however, for the other two ratios the PSC results are nearly identical with the three-dimensional results. Figure 5.10 shows the failure stress against initial crack length for 24.0 inch wide M(T) specimens with constant thickness and width. Again, the results are nearly identical with the three-dimensional results.

These results indicate that the PSC concept can be used to accurately model the fracture behavior of both C(T) and M(T) specimens over a range of specimen sizes and initial crack lengths. The largest errors in predicted failure load occurred for the 2.0 inch wide C(T) specimen. The FRANC2D/L PSC predictions for the M(T) specimen were within 2.5% of the ZIP3D predictions of failure stress. As shown in Figure 5.8, the PSC predictions were lower than the three-dimensional predictions for the smaller specimen widths. Conversely, for larger specimen widths the PSC predictions were higher than the three-dimensional predictions.

5.4 Multiple-Site Damage

Multiple-site damage (MSD) cracking involves two or more cracks that can ultimately interact to influence each other's behavior and the behavior of the overall structure. MSD can significantly reduce the residual strength of a structure. The ability of software to predict residual strength in the presence of MSD is particularly important. Figure 5.11 is a schematic of the idealized geometry for eight different cracking configurations (Dawicke and Newman, 1998). The specimen was a standard 12.0 inch wide M(T) configuration, but with different cracking configurations. The actual crack configurations of the specimens were not exactly symmetric, so the ligament lengths and crack lengths were averaged between the two sides to obtain these symmetric configurations for the analysis. The first three configurations have single center cracks with 2a/W ratios of 4/12, 5/12 and 6/12, respectively. The subsequent configurations are multiple crack configurations. The material was 0.09 inch thick 2024-T3, and all cracks were fatigue precracked at low stress levels.

The same material data used in previous analyses was used for each of the analyses of the eight configurations. As before the plane strain core height was 0.04 inch and the critical CTOA was 5.25°. The analyses were run under displacement control with symmetry boundary conditions for both the specimen load center-line and for the crack face.

Table 3 summarizes the comparison of experimental link-up and failure loads with the predicted FRANC2D/L results. FRANC2D/L predicts the failure load within 6%, and predicts link-up load within 2.4% for all of the cases. Configurations G and H failed at link-up. For these cases, FRANC2D/L correctly predicted link-up before failure.

Table 5.3: Comparison of FRANC2D/L failure and link-up stresses with test results.

Cfg	Exp Failure (ksi)	FRANC2D/L Failure (ksi)	Failure Error	Exp Link-Up (ksi)	FRANC2D/L Link-Up (ksi)	Link-Up Error
A	31.3	30.6	-2.3%			

B	27.7	26.7	-2.4%			
C	23.3	22.4	-4.0%			
D	30.3	30.6	+1.0%	13.2	13.1	-1.0%
E	28.2	28.1	-0.4%	21.6	21.1	-2.4%
F	23.0	22.4	-2.7%	19.7	19.8	+0.5%
G	37.5	36.9	-1.6%	At Failure	19.6	
H	23.4	24.8	+6.0%	At Failure	22.1 & 17.2	

Several interesting observations can be made through comparisons of the various configurations. First, by comparing configurations A and D, we can see that the remaining ligament of the two-crack configuration has little effect on the residual strength, reducing the strength only slightly. Comparing configuration A with configurations F and H, we see that in both cases the small damage in front of the main crack significantly reduces the strength of the specimen. Comparing configuration C with F we see that F behaves more like a single 6" crack, rather than a 4" crack with damage. That is, the damage makes the effective length look like the total of the main crack plus damage. Configuration G, which had the highest strength, shows that damage in front of a main crack will not always reduce the strength to the level of the total length including the damage. However, assuming the reduction occurs will be conservative.

Figure 5.12 through Figure 5.14show the crack tip link up process for Configuration F, which has a 4 inch lead crack with a single pair of MSD cracks in front of the lead crack. The MSD cracks are each about 0.56" long and the remaining ligament between each MSD crack and the lead crack is about 0.48" long. The figures all show color contours of the von Mises stress using the same stress range and deformed geometry magnified x15. Figure 5.12 shows the condition just before Tip 1 is ready to propagate. The fracture criterion at Tips 2 and 3 is slightly below critical. Figure 5.13 shows the condition where the remaining ligament between Tips 1 and 2 is ready to break. Tip 2 is at the fracture criterion. As the crack face forces are relaxed for Tip 2, load redistribution causes Tip 1 to exceed the fracture criterion. Crack face forces are subsequently relaxed for both Tip 1 and Tip 2. The resulting load redistribution causes Tip 3 to meet the fracture criterion, and crack face load relaxation ensues at Tip 3. Each node along the crack face has a count of the number of steps required for load relaxation. Only after all nodes along the crack face are finish relaxing does the far field boundary condition start increment again. Essentially, all cracks must be stable before the boundary condition increments will resume. Figure 5.14 shows the next sable condition after Tips 1 and 2 have merge, breaking the ligament between the lead crack and the MSD crack. The model now contains a single crack. Figure 5.14 shows clearly residual stresses in the wake of the ligament, and the effect of the residual stresses on the deformed shape.

5.5 Effects of Material Thickness on Plane Strain Core Height

The fact that material thickness affects constraint has been understood for some time. ASTM standards specify requirements that must be met for plane strain fracture toughness to determine a K_{Ic} critical stress-intensity factor. These standards are, in effect, establishing that enough constraint must exist to consider the test sufficiently close to plane strain conditions. Thickness will have a similar effect for elastic-plastic fracture. This section presents elastic-plastic results used to explore how plane strain core height varies with the thickness of a specimen.

Just as the critical stress-intensity factor varies with thickness, the critical CTOA varies with thickness. However, no significant studies exist to characterize CTOA as a function of thickness for 2024-T3. As a result, for the purposes of this study, CTOA is assumed constant at 5.25° for all thicknesses analyzed.

Figure 5.15 and Figure 5.16 show the variation in failure load as a function of PSC height for a 6" C(T) specimen and 12" M(T) specimen, respectively. Three-dimensional analysis results were used to find the "correct" core height to predict failure for the respective specimen and thickness. This same process was repeated for both the 6" C(T) and 12" M(T) specimens over a range of thicknesses from 0.025" to 0.25". The experimentally verified critical CTOA for the B=0.09" thick specimen was used for the full range of specimens for the study. While in reality the critical CTOA will almost certainly vary with thickness for these specimens, the qualitative results are important. Figure 5.17 shows how the PSC height varies with specimen thickness. The graph shows that the relationship between core height and thickness is not linear. For all thicknesses below about 0.18" the C(T) core height is larger than the M(T) core height. A transition occurs at about 0.018" after which the M(T) core height is larger then the C(T) core height. The general trend in the curves for both specimens is about the same.

The implication of the plateau for the smaller thicknesses may be that even for very thin specimens, some level of stress traxiality exists at the crack tip, resulting in constraint that must be modeled for the most accurate residual strength analyses.

5.6 Summary and Conclusions

This chapter presented analysis results for plane stress, plane strain, and plane strain core approximations. Three-dimensional analyses were used in conjunction with experimental data as a basis for comparison. Plane stress and plane strain results do not capture the variable constraint that exists throughout the specimen during fracture. The plane strain core was able to characterize constraint and produced more accurate residual strength analyses. The plane strain core proved effective for two different standard laboratory specimen types (M(T) and C(T)), for a variety of specimen sizes, and for a variety of initial crack-length to width ratios as well as MSD cracking configurations.

The conclusions are:

- The plasticity implementation in FRANC2D/L is accurate and effective for Mises type materials.
- The plane strain core concept can approximate the three-dimensional constraint effects present during fracture of thin-sheet aluminum.
- A single value of CTOA determined from tests on a C(T) laboratory specimen were used to predict failure for other C(T) geometries and for M(T) specimen geometries, including variations in both specimen size and initial crack length.
- The plane strain core concept can be used to accurately simulate fracture and link-up for MSD cracking configurations.
- The relationship between material thickness and plane strain core height is not linear.
- Even the thinnest specimen considered (0.025") required a PSC to best model the reference three-dimensional results.

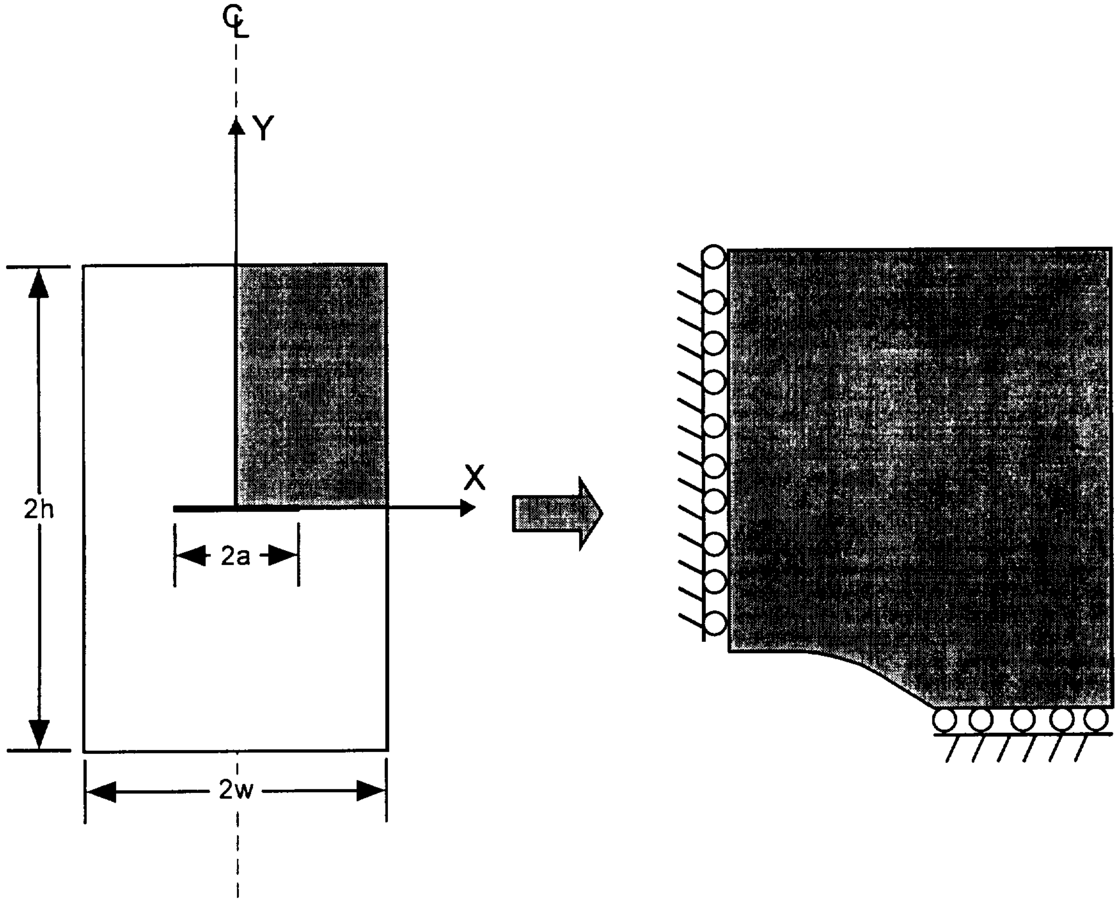

Figure 5.1: Schematic of a deformed middle-crack tension specimen showing how symmetry is exploited.

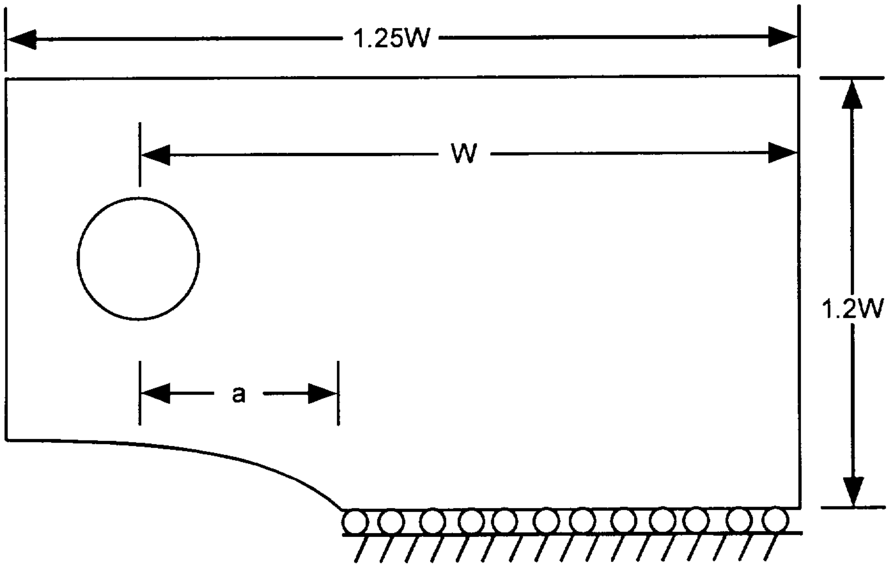

Figure 5.2: Schematic of a deformed compact tension specimen showing how symmetry is exploited.

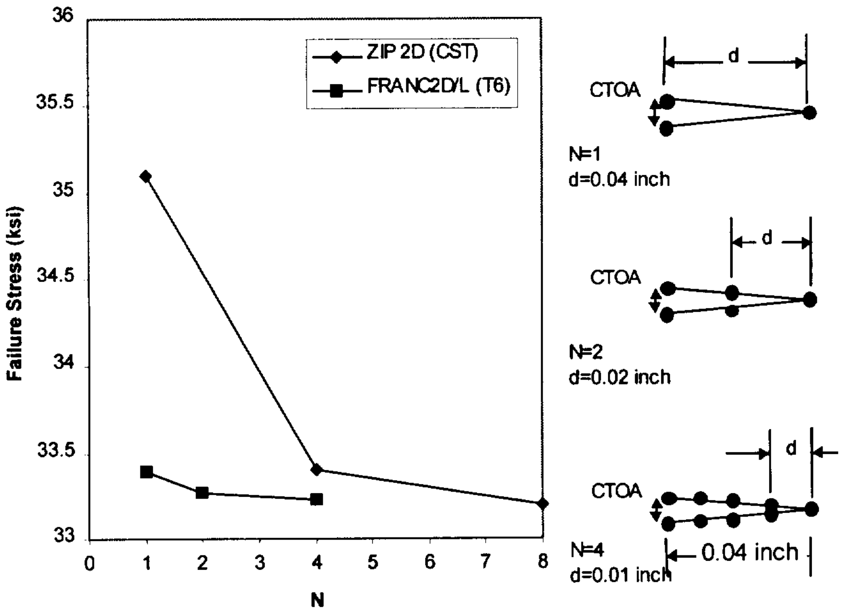

Figure 5.3: Mesh convergence study results for the 3" M(T) specimen. The small strain, six-noded triangle implemented in FRANC2D/L performs well at each of the element discretizations.

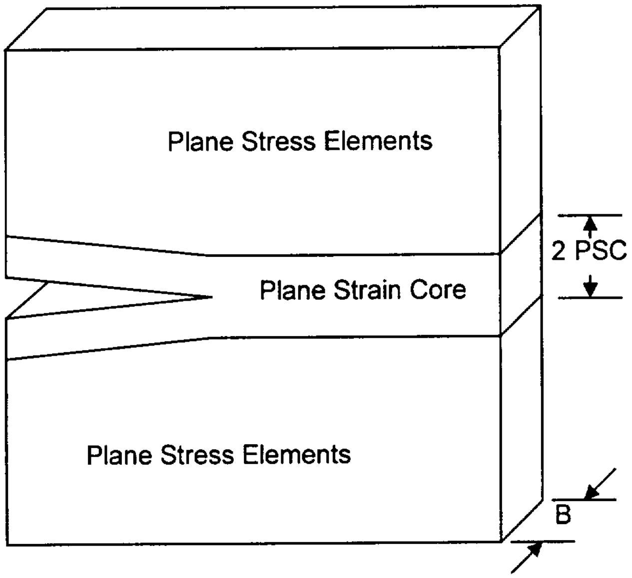

Figure 5.4: Plane strain core concept.

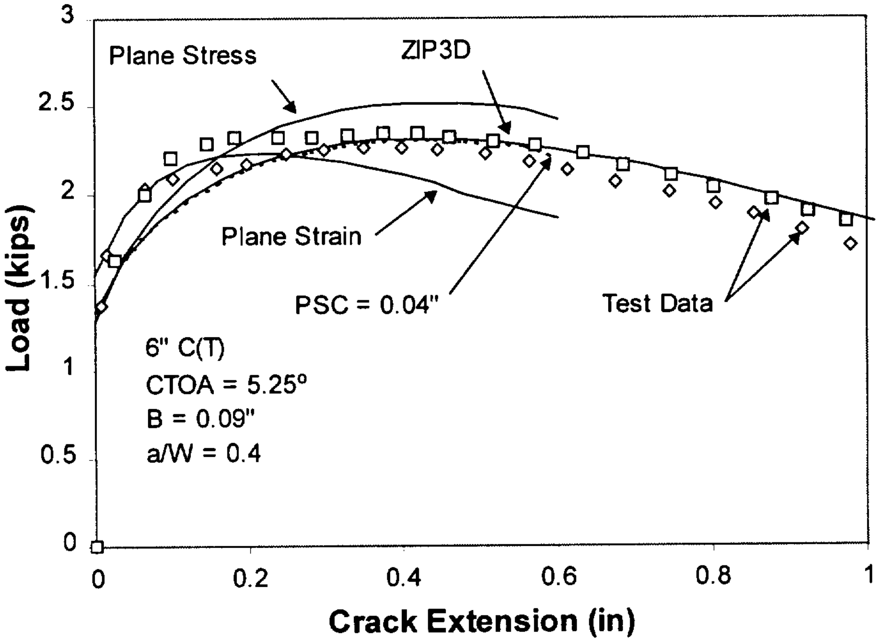

Figure 5.5: Comparison of simulated load vs. crack extension with experimental data for 6.0 inch wide C(T) specimens. The plane strain core closely matches the 3D result, and provides a good approximation to the experimental results.

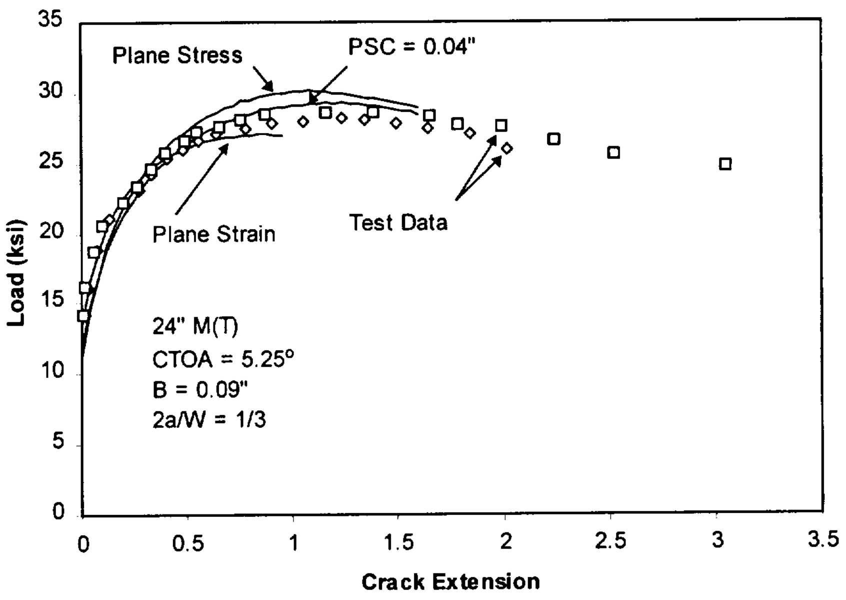

Figure 5.6: Comparison of simulated load vs. crack extension with experimental data for 24.0 inch wide M(T) specimens. The plane strain core provides a much better approximation to the experimental results than either plane stress or plane strain.

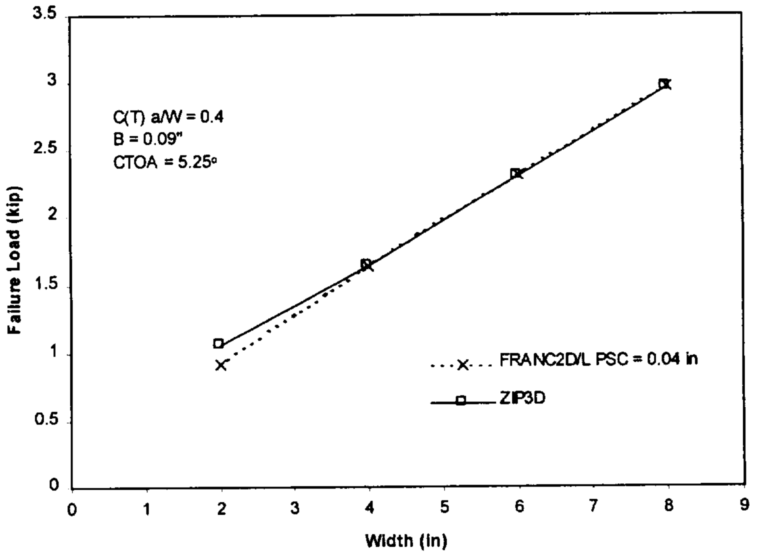

Figure 5.7: Predicted failure load vs. specimen width for C(T) specimens with constant thickness and a/W.

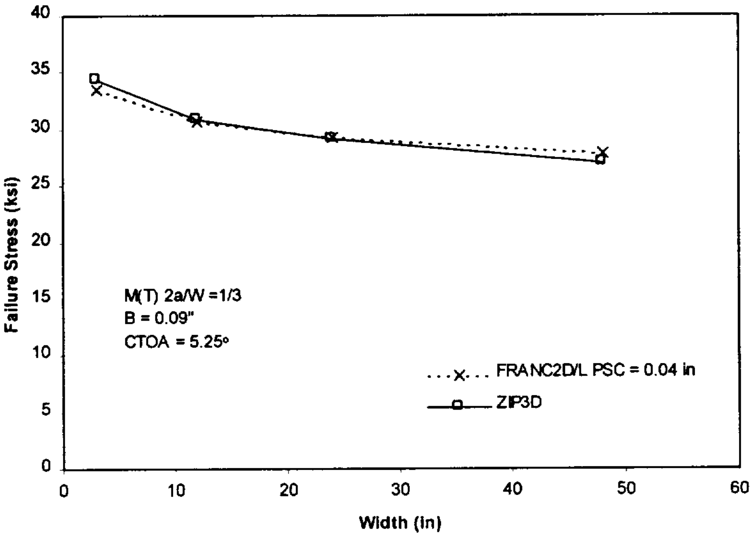

Figure 5.8: Predicted failure stress vs. specimen width for M(T) specimens with constant thickness and 2a/W.

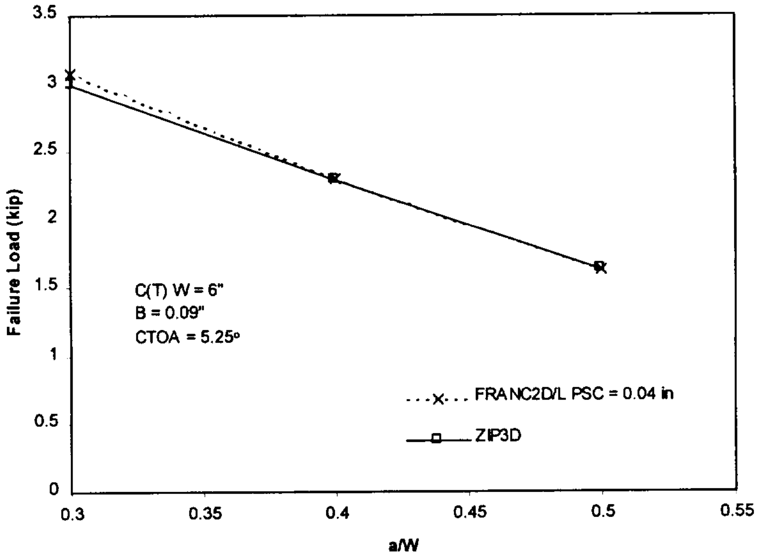

Figure 5.9: Predicted failure load vs. initial crack length for C(T) with constant thickness and width.

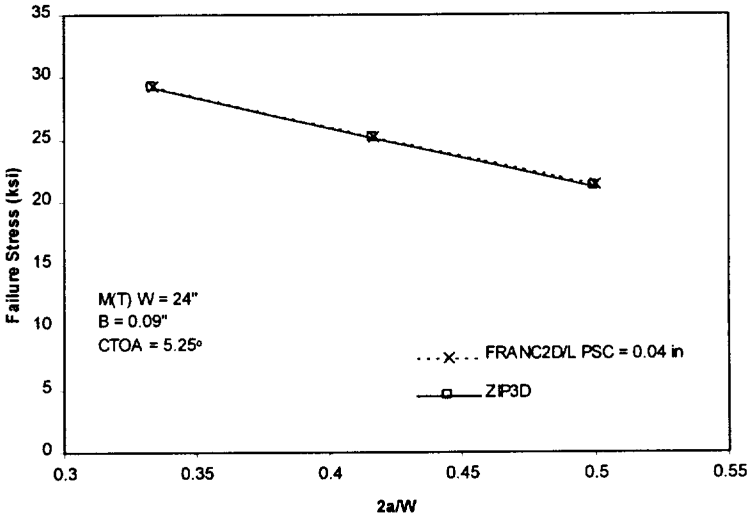

Figure 5.10: Predicted failure stress vs. initial crack length for M(T) with constant thickness and width.

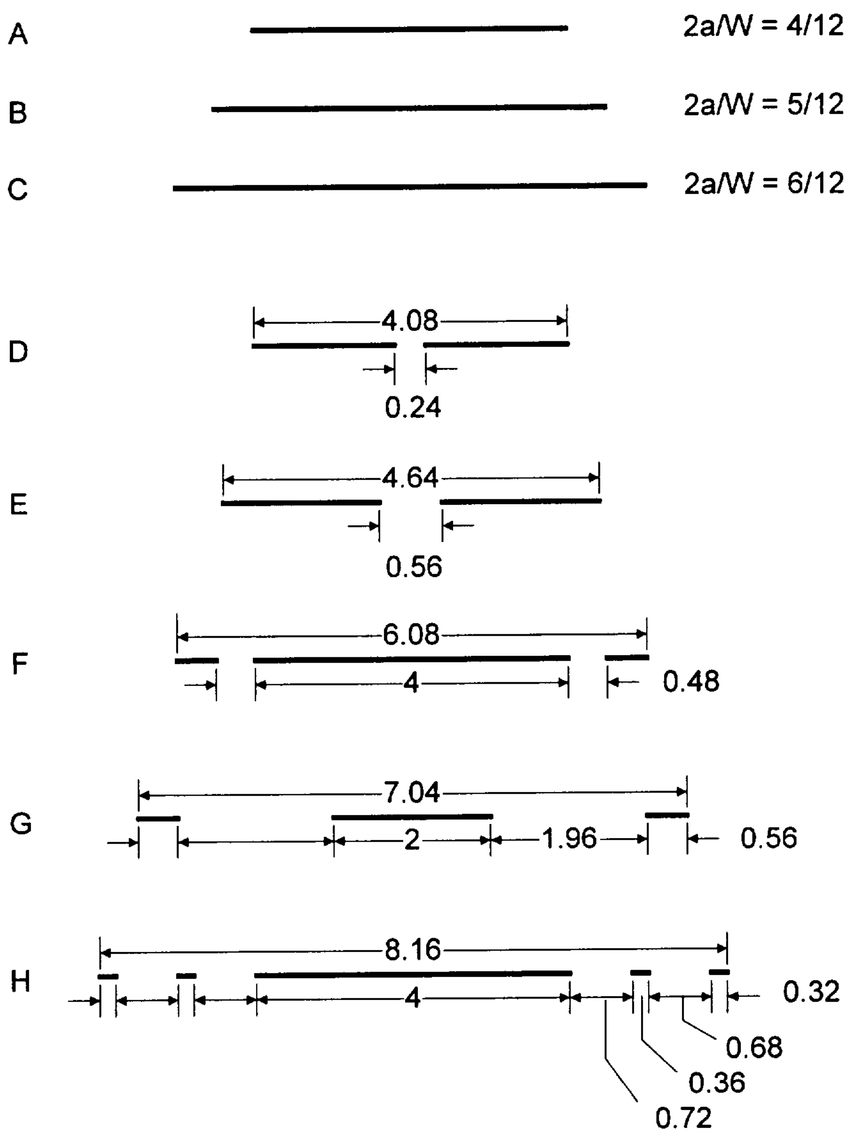

Figure 5.11: Additional single crack and MSD configurations analyzed (all configurations are symmetric).

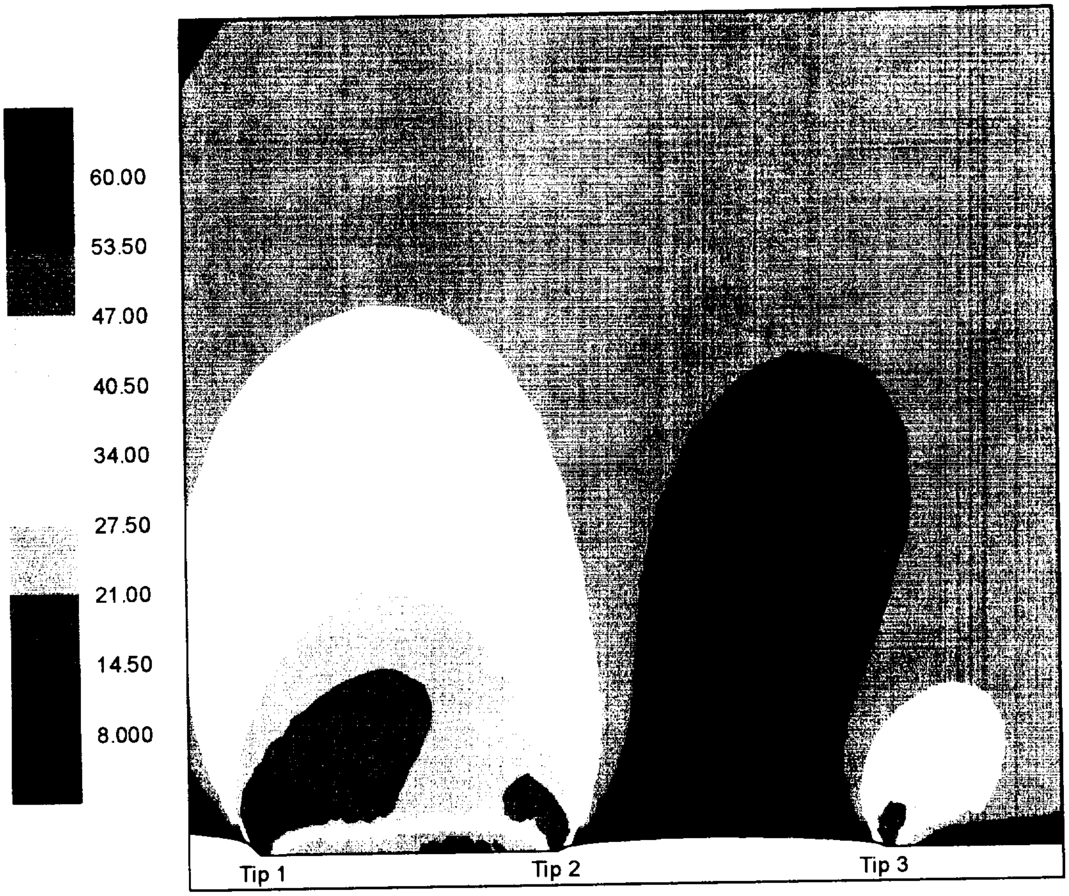

Figure 5.12: Impending crack growth at Tip 1 for MSD Configuration F. Color contours of von Mises stress (Ksi) on deformed body magnified x15.

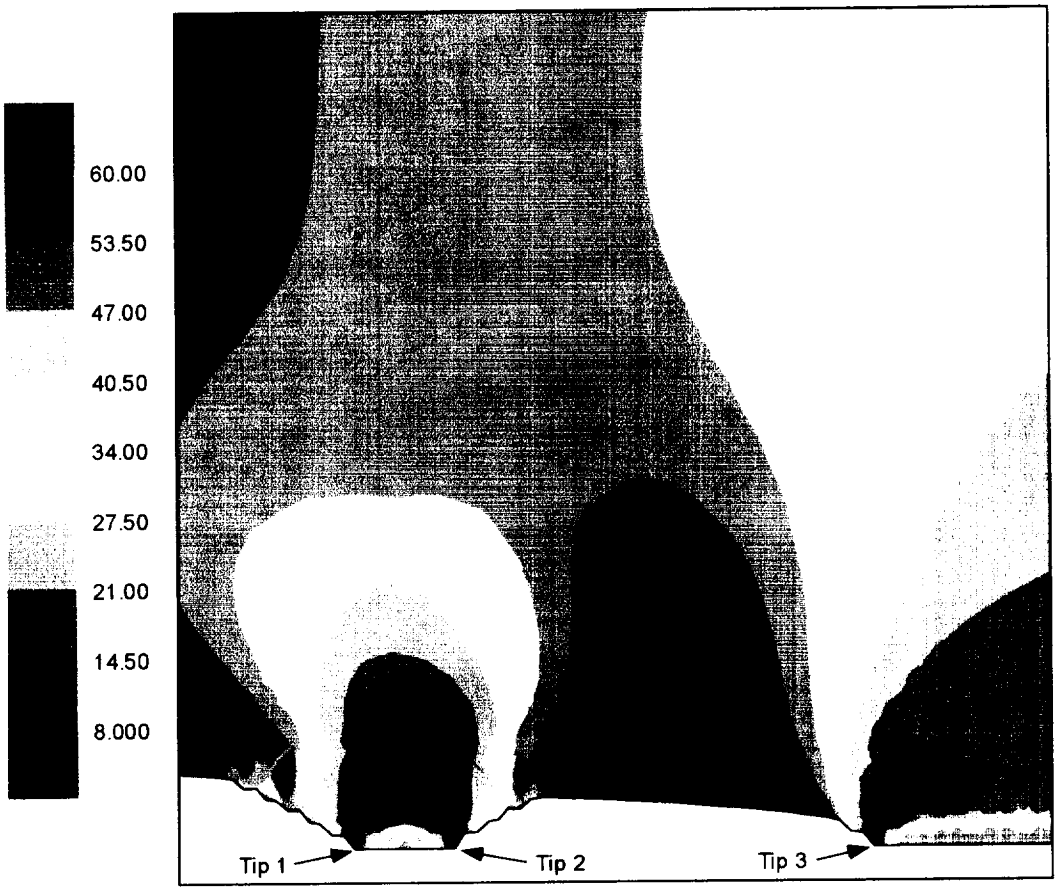

Figure 5.13: Remaining ligament between the lead crack and MSD crack ready to break. Color contours of von Mises stress (Ksi) on deformed body magnified x15.

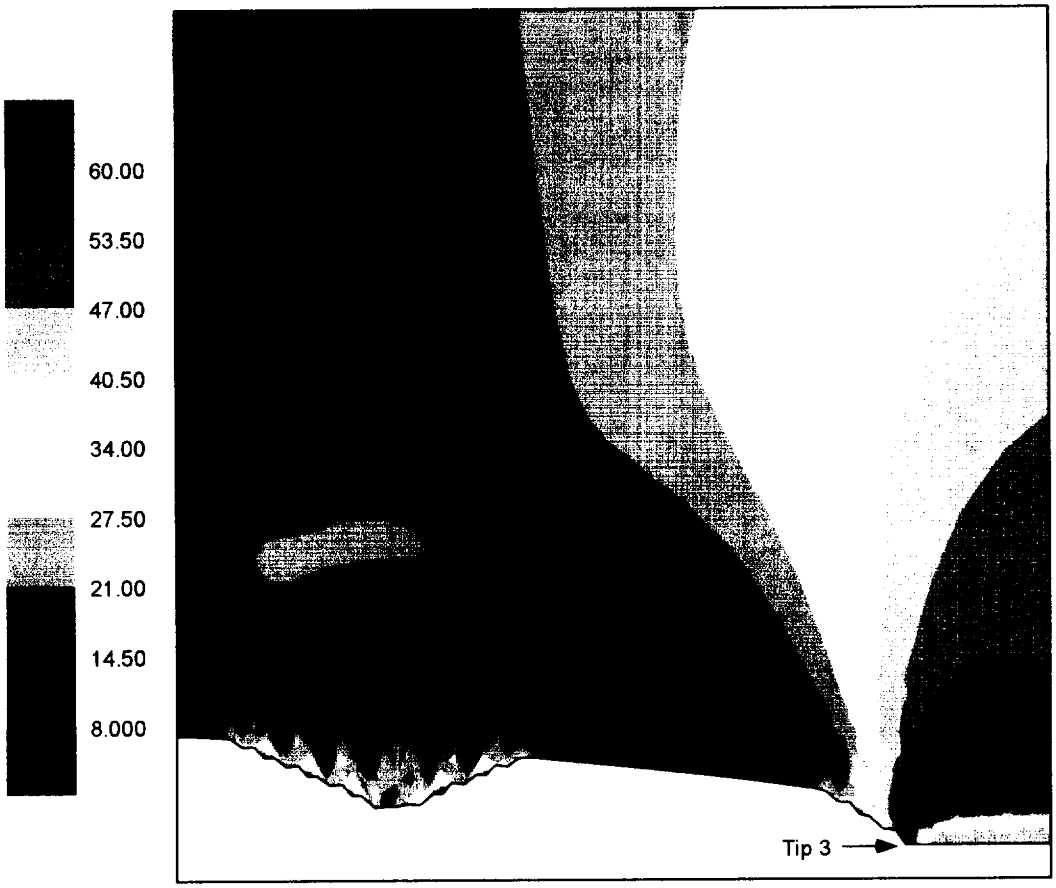

Figure 5.14: Lead crack and MSD crack have merged, leaving a single crack. Color contours of von Mises stress (Ksi) on deformed body magnified x15.

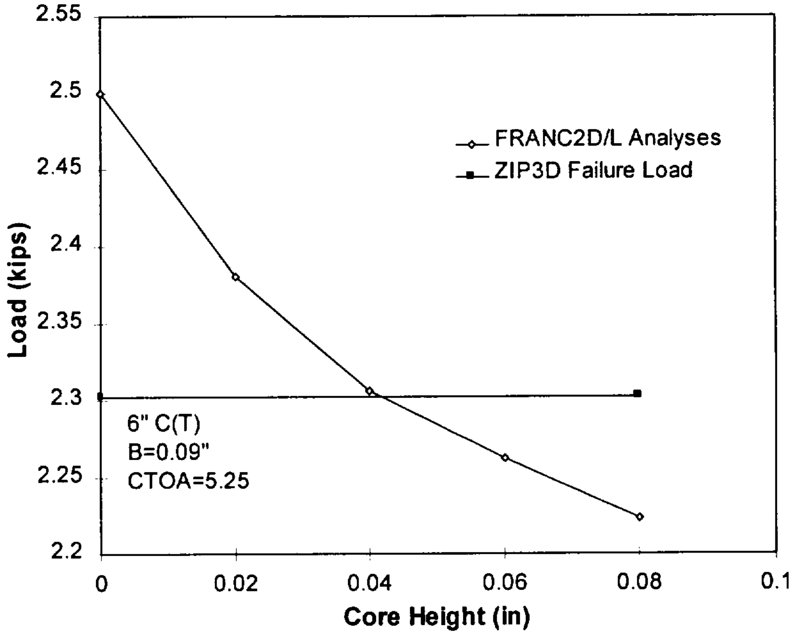

Figure 5.15: Variation in failure load as a function of PSC height for a 6" C(T) specimen .

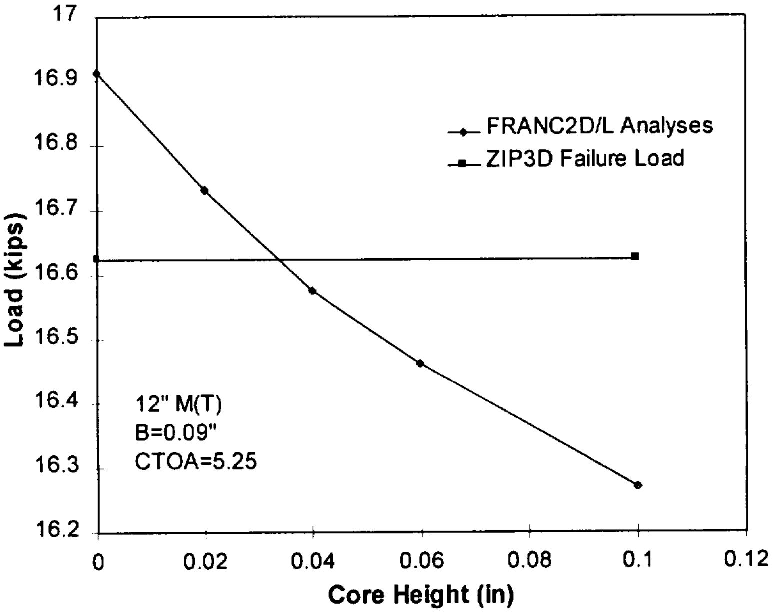

Figure 5.16: Variation in failure load as a function of PSC height for a 12" M(T) specimen.

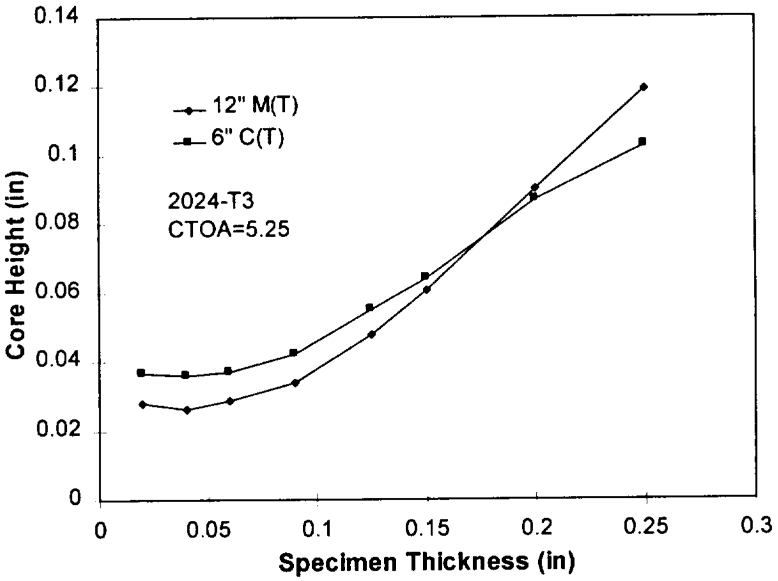

Figure 5.17: Variation of plane strain core height with specimen thickness.

Chapter 6

Fracture Analyses with Remeshing

Modeling curvilinear crack growth without knowing the crack path in advance requires mechanisms to predict and represent an evolving crack geometry. In this chapter we present a series of analyses to demonstrate the remeshing approach to elastic-plastic crack growth. First, analyses that use the remeshing approach will be compared to analyses using the nodal release approach. These analyses are Mode-I only. Next, comparisons are made with experimental data for curving cracks.

6.1 Analysis Background

Some of the fracture analyses presented here are Mode-I and some are Mode-I/II. However, all of the analyses were generated using the remeshing and mapping algorithms and the direction and fracture criteria discussed in previous chapters. The fracture criterion used is the magnitude of the CTOD vector, and the direction criterion used is the maximum tensile stress evaluated at the crack tip node.

Three different specimens were used for the analyses in this chapter: 6" C(T), 12" M(T) and a mixed-mode I/II Arcan specimen. The C(T) and M(T) specimens are Mode-I only test specimens. Numerical results from Chapter 5 for the specimens are used for comparison with the results from the remeshing-mapping approach. Tables 5.1 and 5.2 give material properties for 2024-T3 aluminum used for the Mode-I comparisons.

The mixed-mode analyses are simulations of experiments conducted by Amstutz et al. (1995a, 1995b). Figure 6.1 is a schematic of the Arcan specimen used by Amstutz for the mixed-mode testing. The specimen allows a full range of loading from Mode-I to Mode-II. The Amstutz et al. (1995a, 1995b) results are also for 2024-T3 aluminum, so Tables 5.1 and 5.2 described the material properties for the mixed-mode analyses (same thickness as for the C(T) and M(T) tests). As for the M(T) and C(T) specimens, all Arcan specimens were fatigue pre-cracked at low stress levels in the LT orientation, and all tests were conducted under displacement control.

The value of critical CTOD used for the mixed-mode analyses deserves special mention. As discussed previously, CTOD for 2024-T3 varies with the rolling direction of the material by about 25% (Amstutz et al., 1995b). Dawicke (1996) found CTOA at 0.04” behind the crack tip to be 5.25 degrees. The equivalent CTOD is 0.00366". This value of CTOD falls in the midrange of the experimental data measured by Amstutz et al. (1995b). The most accurate simulation would account for the variation in CTOD as a function of crack tip orientation with respect to material rolling direction. However, for this analysis only the single value of CTOD based on Dawicke’s result is used.

6.2 Mode-I Analyses

The results of this section serve mainly as verification that the remeshing-mapping approach gives the same results as the nodal release approach. Two standard test specimen configurations are used for comparisons in this section: compact tension specimens and middle crack tension specimens. The results from Chapter 5 for FRANC2D/L where C(T) and M(T) specimens were analyzed using nodal release are included for comparisons with the results from this chapter. Two specimen configurations are considered: a 6” wide C(T) specimen with a/W = 0.4, and a 12” wide M(T) specimen with 2a/W = 1/3.

Figure 6.2 shows the mesh for the C(T) specimen, and Figure 6.3 shows the mesh near the crack tip. The crack tip element size is 0.02”, and the mesh into which the crack propagates is uniform with a characteristic element size of about 0.02”. Since CTOD is measured at 0.04" behind the crack tip, there are two elements along the crack face behind the tip to the measurement point.

Figure 6.4 shows the load-crack extension curves for the 6” wide C(T) specimen. The solid lines show results for automatic remeshing and dashed lines show results for nodal release from Chapter 5. Also included in Figure 6.4 are test data from Dawicke and Newman (1998). As expected, although the nodal release and automatic remeshing algorithms are completely different, the results match well.

Figure 6.5 shows the mesh for the 12” wide M(T) specimen. The crack tip element size is 0.02”, and the mesh into which the crack propagates has a characteristic element size of about 0.04”. Figure 6.6 shows the load-crack extension curves for the 12”wide M(T) specimen. The solid lines show results for automatic remeshing and dashed lines show results for nodal release from Chapter 5. Also included in Figure 6.6 are test data from Dawicke and Newman (1998). The results from the current analysis using automatic propagation with remeshing are indicated by the dashed lines from a plane stress case. Again, the results match well.

6.3 Mixed-Mode I/II Analyses

Figure 6.1 is a schematic showing the definition of loading angle and specimen dimensions for the Arcan specimen and fixture tested by Amstutz et al. (1995a, 1995b). Single point bolt loads can be applied on opposite sides of the fixture to create loading that is pure Mode-I, pure Mode-II, or one of five intermediate values. Figure 6.7 shows a mesh of the Arcan specimen for a 30° loading angle. To simplify post processing, the mesh was rotated for each loading angle and loading always applied vertically. The crack tip element size is 0.02" and the surrounding element size is about 0.04". Loading angles from 0° to 90° in 15° increments were analyzed.

The analyses were performed by loading the specimen vertically under displacement control. When the CTOD reached the critical value, the crack propagated in the direction of maximum tensile stress. As shown in Figure 6.8, significant plasticity occurs in the specimen. Thus, propagation is occurring through material that has experienced significant yielding.

Figure 6.9 compares the crack path recorded during experiments and the crack path predicted during the FRANC2D/L analysis for loading angles of 0, 30, and 60 degrees. The maximum tensile stress and CTOD fracture criterion predict the crack path well. The FRANC2D/L analyses tend to under-predict the initial kinking angle and then slightly over-predict the later propagation angle. For loading angles greater than 60° the material fails in shear. As discussed in Chapter 3, the maximum tensile stress criterion cannot predict shear failure, so these analyses are not included.

The analyses also predict the residual strength of the specimen for the different loading angles. Figure 6.10 compares the experimental load-crack extension with the FRANC2D/L results for 0 and 60 degree loading angles. In general terms, the FRANC2D/L analyses predict the trend of lower strength for the 60 degree case, compared to the 0 degree case. In addition, the analyses predict the cross-over in load-crack extension curves displayed by the experimental data. More specifically, the FRANC2D/L result over predicts the experimental results by 9% for the zero degree case and over predicts by 6% for the 60 degree case.

Figure 6.11 compares the experimental load-crack extension with the FRANC2D/L results using plane stress and plane strain assumptions for the 30 degree loading angle. The plane stress analysis over-predicts by 10%, while the plane strain analysis significantly over-predicts the experimental result. The character of the plane strain result is similar to that for the previous M(T) analysis, in that the plane strain curve does not cross the plane stress curve. For the previous C(T) result, the curves do cross.

Results are not presented for the 75 and 90 degree analyses. As previously discussed, these loading cases fail in Mode-II dominated propagation. The maximum tensile stress criterion is not valid for those cases.

6.4 Summary

The results presented show that use of an elastic-plastic material model with a CTOD fracture criterion and maximum tensile stress direction criterion can predict the residual strength and crack path for test specimens with significantly different fracture behavior. The Arcan test results show significant crack curving. The analyses capture this behavior, even in the presence of significant plasticity. The analyses also predict residual strength within an error of approximately 10%. Because the value of critical CTOD used in these analyses was obtained independently and not adjusted in these analyses, the results demonstrate predictive capability for elastic-plastic fracture.

Reliable analysis relies on accurate plasticity states for the material into which the crack is propagating as well as capturing the residual stresses along the crack face. For the model presented here, stresses and the nodal displacements (and hence, strains) are mapped from one mesh to another during propagation. Ensuring a quality mesh and enforcing equilibrium after each propagation step was adequate to obtain reasonable fracture predictions. Similarly, the results show that reasonable fracture predictions can be obtained using a well refined mesh, without resorting to special elements at the crack tip.

It is clear from the results that a plane strain core model to capture crack tip constraint improves the accuracy of the predicted failure loads for the M(T) and C(T) specimens. It is not clear how well this approach will work for a Mixed-Mode growing crack. Equally important is the unknown effect of a constraint model on the criterion used for direction prediction. These topics are areas for future research.

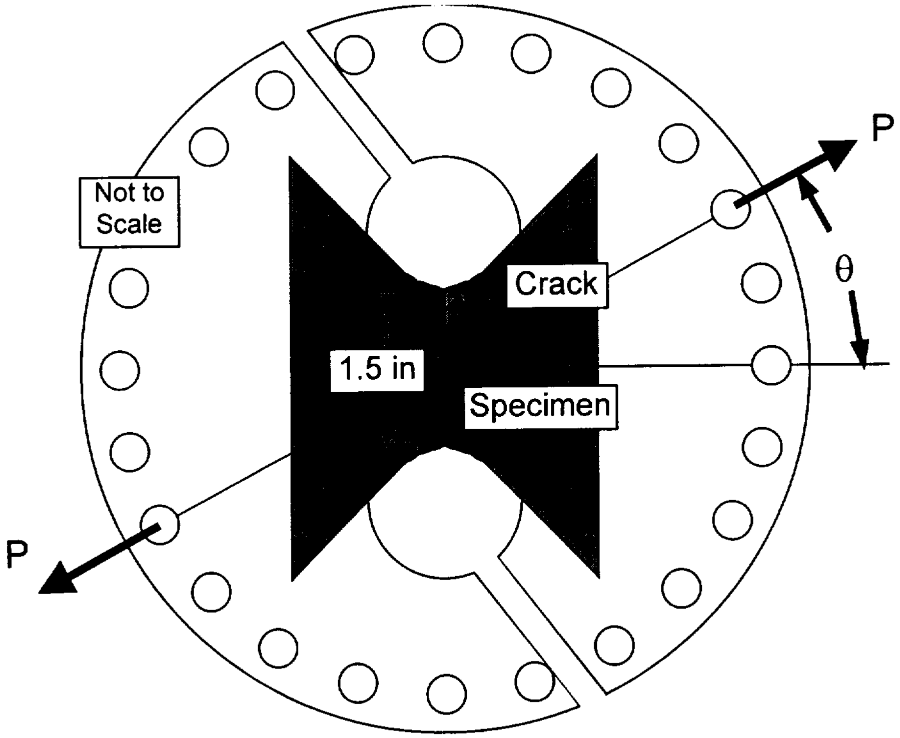

Figure 6.1: Schematic of Arcan test specimen and fixture.

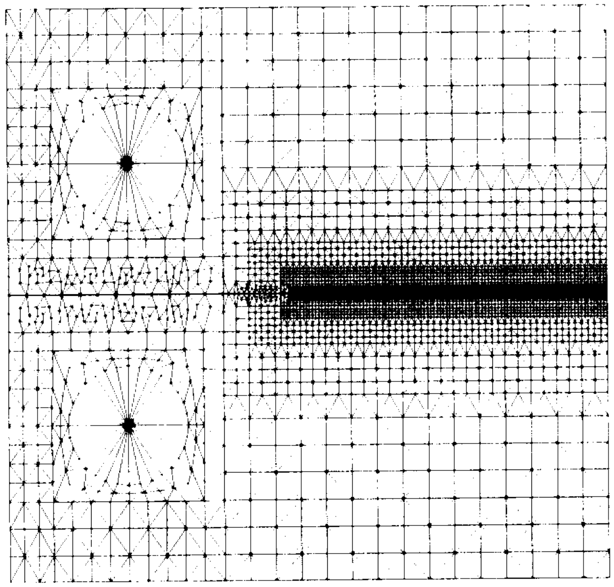

Figure 6.2: Finite element mesh for C(T) analysis.

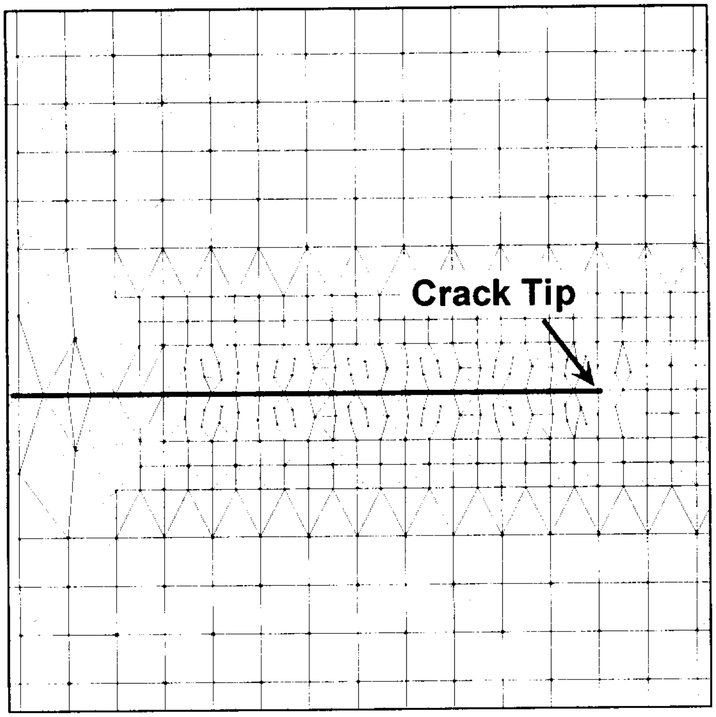

Figure 6.3: Detail of mesh near crack tip for 6" wide C(T) specimen.

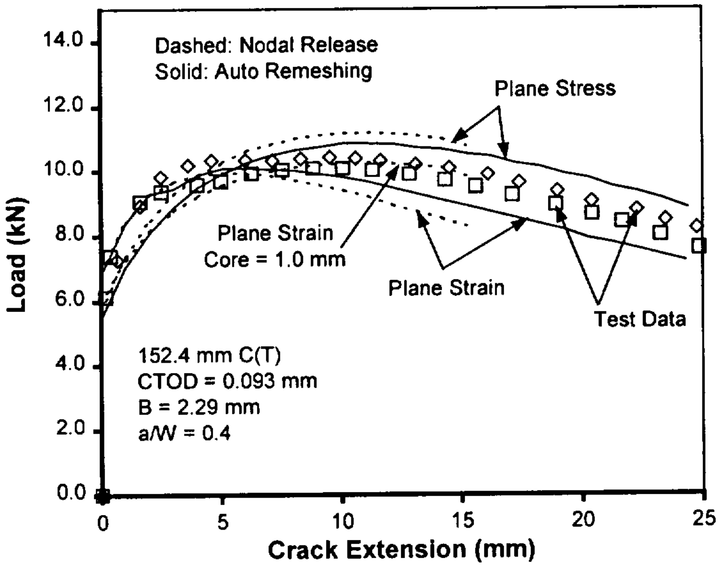

Figure 6.4: Load crack extension curve for C(T) analysis.

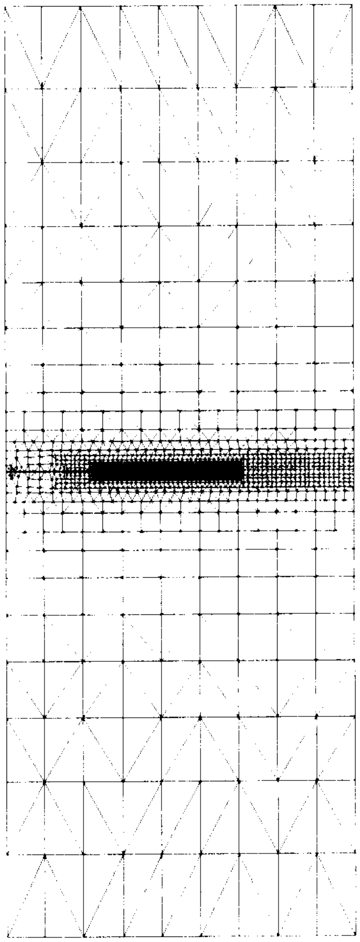

Figure 6.5: Finite element mesh for 12" wide M(T) analysis.

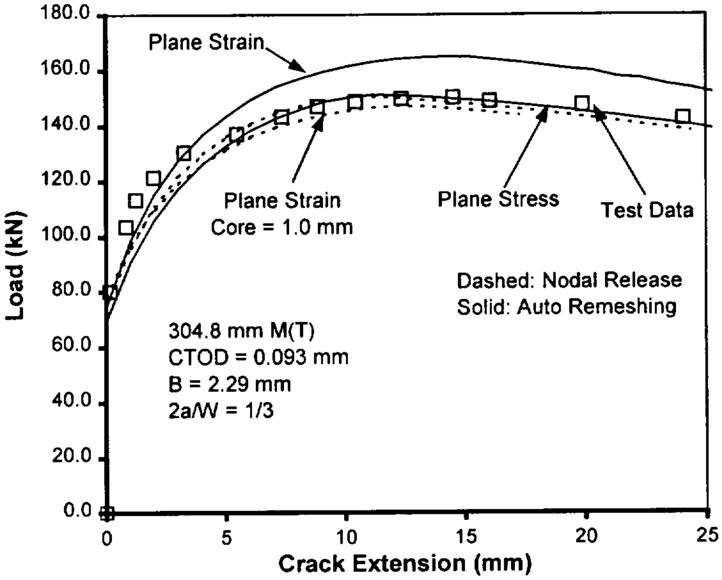

Figure 6.6: Load crack extension curve for M(T) analysis.

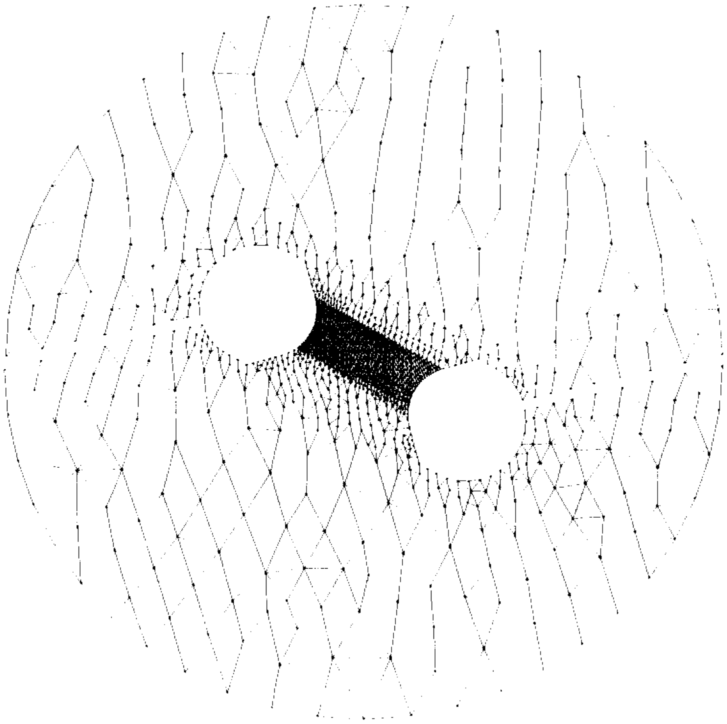

Figure 6.7: Finite element mesh for Arcan analyses (30 degree load angle).

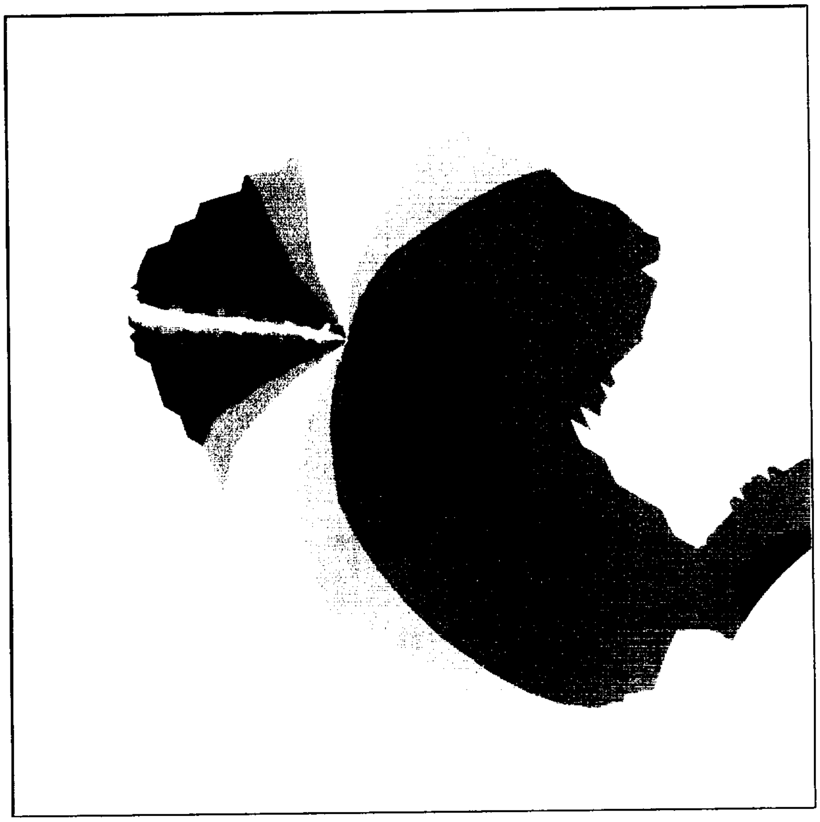

Figure 6.8: Shaded region showing elements that have yielded after 10 mm of crack propagation (30 degree load angle).

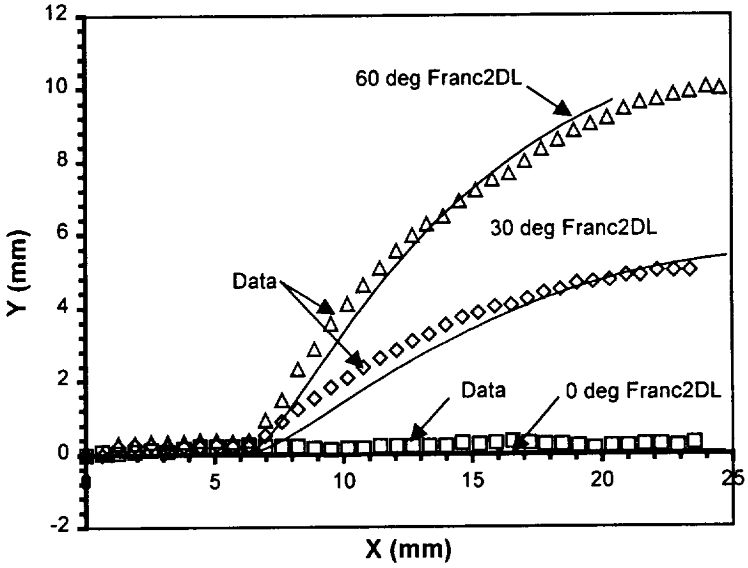

Figure 6.9: Observed and predicted crack paths for Arcan specimen.

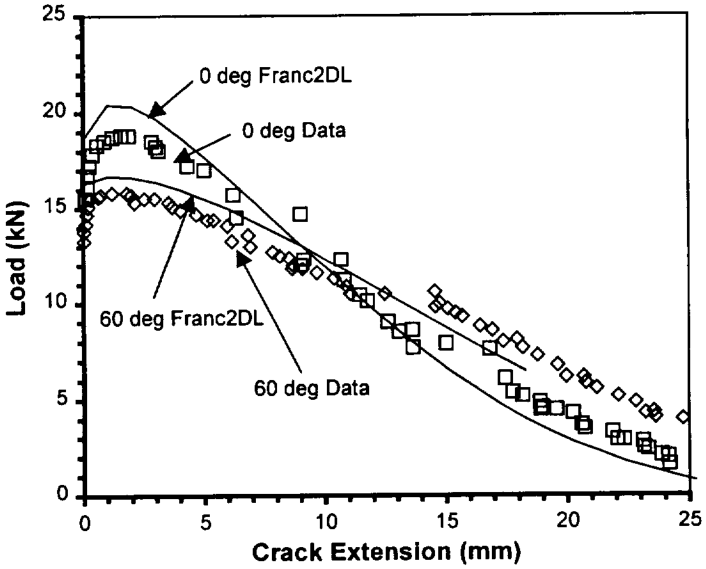

Figure 6.10: Load crack extension curve for Arcan analyses.

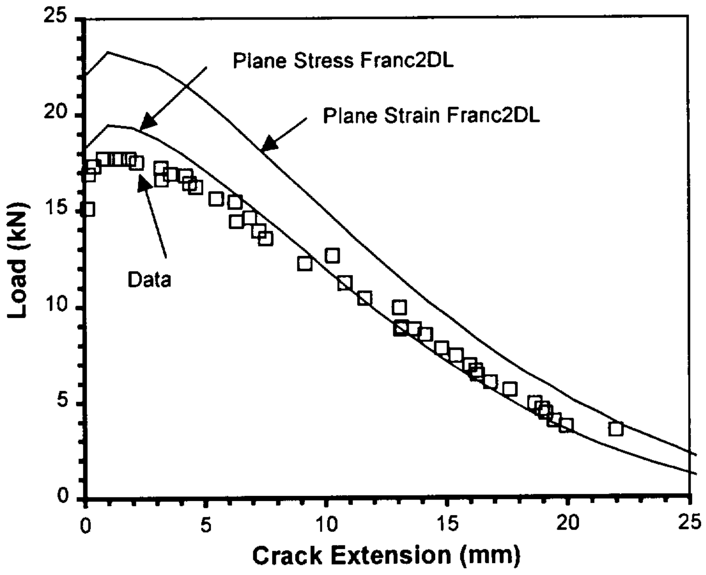

Figure 6.11: Comparison of plane stress and plane strain analyses for Arcan specimen with 30 degree load angle.

Chapter 7

Summary

This chapter presents a summary of this work. Each chapter is summarized, then conclusions are drawn based on experience with the implementation and on results from chapters of example applications. Finally, brief recommendations outline areas for near-term improvement and long-term research.

7.1 Chapter Summaries

Chapter 1 introduced the motivation and context for this work and introduced the crack growth methodology, which served as the outline for the remainder of this work.

In Chapter 2, we discussed fracture and direction criteria that may be appropriate for Mixed-Mode fracture. Energy based fracture integrals have been used extensively in the past in the form of resistance curves, and will continue to be used in the future for known configurations, but their applicability for Mixed-Mode fracture, especially in multiple cracks scenarios, is in question. For this work the fracture criterion implemented was the critical crack tip opening displacement. While this criterion also has limitations and has not been proven widely, it does perform extraordinarily well in the circumstances tested. Similarly, no single theory exists to predict the crack direction. Recent results from the literature indicate that a combined theory of maximum tensile stress and maximum shear stress may predict direction for materials that fail in tension under some loading conditions and in shear under other loading conditions. For this work the maximum tensile stress criterion was implemented. While this criterion will only predict the crack growth direction correctly for materials with loading that causes tensile dominated fracture, implementation was relatively straightforward and has proven robust. Conveniently, for this criterion no special material dependent properties are needed.

Chapter 3 discussed various approaches to elastic-plastic fracture from the literature and describes the two different approaches to fracture implemented: nodal release and automatic remeshing with mapping. The algorithms have been implemented to model elastic-plastic fracture under a number of different circumstances. The nodal release algorithm is specialized to work for either of two different situations: cracking along an edge of symmetry or cracking along a predefined curving crack path. The automatic remeshing algorithm can be used either in a step-by-step manual mode or in fully automatic mode. In fully automatic mode the direction is predicted from maximum tensile stress at the crack tip. Crack tip constraint can be modeled during nodal release using the plane strain core. Specialized algorithms allow multi-site damage during nodal release. Manual remeshing and mapping can be used to merge MSD crack tips when automatic propagation is interrupted by crack tips in close proximity to one another.

In Chapter 4, we discuss the state variable mapping algorithm that maintains the element and nodal solution when remeshing is used to propagate cracks. The inverse isoparametric mapping algorithm has proven robust, accurate, and efficient. The algorithm uses knowledge of the remeshing zone around each crack tip and only performs mapping for these nodes and elements. Test problems show that the mapping time is approximately the same as the remesh time, which is a small fraction of the total analysis time.

Chapter 5 presented analysis results for two different symmetry specimen types: compact tension and middle crack tension. Plane stress and plane strain results do not capture the variable constraint that exists throughout the specimen during fracture. The plane strain core implementation was able to characterize constraint and produced more accurate residual strength analyses. A simple study on constant thickness configurations showed that a single plane strain core height determined by strength comparisons with experimental and three-dimensional data can be used to predict the behavior of a wide variety of other specimen types and configurations. In addition, multi-site damage simulations were accurate for both residual strength and link-up loads when the PSC was included. A second study considered a single configuration for the M(T) and C(T) specimens and varied the specimen thickness. For each thickness of each specimen, the best plane strain core height was found by matching failure load with three-dimensional finite element results. The plane strain core height was not the linear function of thickness, and a plane strain core was necessary even for the thinnest specimen, indicating that crack tip constraint is important even for very thin specimens.

Chapter 6 presented Mixed-Mode analysis results. The results presented show that use of an elastic-plastic material model with a CTOD fracture criterion and maximum tensile stress direction criterion can predict the residual strength and crack path for test specimens with significantly different fracture behavior. The Arcan test results show significant crack curving. The analyses capture this behavior, even in the presence of significant plasticity. The analyses also predict residual strength within an error of approximately 10%. Similarly, the results show that reasonable fracture predictions can be obtained using a well refined mesh, without resorting to special elements at the crack tip. Because the value of critical CTOD used in these analyses was obtained independently and not adjusted in these analyses, the results demonstrate predictive capability for elastic-plastic fracture. It is clear from the results that a plane strain core model to capture crack tip constraint improves the accuracy of the predicted failure loads for the M(T) and C(T) specimens. It is not clear how well this approach will work for a Mixed-Mode growing crack. Equally important is the unknown effect of a constraint model on the criterion used for direction prediction.

7.2 Conclusions

The primary result of this work is an elastic-plastic fracture simulation tool implemented in a relatively general way, such that as new technologies emerge (e.g. fracture or correction criteria), they can be implemented with relative ease. In addition, the software is implemented within a relatively user-friendly framework, such that researchers and practicing engineers can apply the model to realistic problems.

The comparisons of analysis results with experimental data show that the model can produce accurate residual strength and crack path predictions for a variety of specimens and crack configurations. The critical crack tip opening displacement vector proved effective as a fracture criterion for Mixed-Mode analyses. While the maximum tensile stress direction criterion is clearly not applicable in all situations, its simplicity makes it attractive as a general purpose direction criterion for materials that fail under tensile dominated loading conditions. The results also show that a two-dimensional approximation needs some form of constraint model to capture the stress triaxiality near the crack tip and produce the most accurate strength predictions.

7.3 Recommendations for Future Work

In the near-term several improvements to the software would prove useful. First, a plane strain core implementation to capture some measure of constraint during remeshing-mapping analyses could increase the accuracy of residual strength predictions. Care should be taken to investigate the effect of having elements that change from plane stress to plane strain as the core extends. Also, the effects of the core on the local tip stress state should be investigated to ensure that no artificial influence on the direction is introduced. Second, recent advances in criteria that can predict crack growth direction under both tensile and shear dominated situations should be investigated. Finally, the J and T^* integrals may prove to be useful additions to the software. The J_R curve has been a standard in the industry for a number of years and will continue to be used in the future under many situations. The T^*_R curve may in the future prove to have more utility than the J_R curve, once its limitations are better understood.

Another improvement to the software would have long-term benefit to the software as research tool. A crack-face contact model would open up the possibility for applying FRANC2D/L in a variety of circumstances, including:

- explicit modeling of fatigue crack growth on a cycle by cycle basis, where crack face closure and plasticity in the wake is modeled explicitly;
- softening behavior at the crack tip opens of the possibility of modeling elastic-plastic crack growth for materials like concrete, which may have a large process zone;
- crack formation, where the softening behavior associative with void growth might be modeled along the interface.

A final recommendation for future work is to implement a finite strain model. Many high toughness materials exhibit significant blunting with corresponding large strains around a crack tip. Computer models of these materials will require a finite strain model to accurately model fracture.

References

Amstutz, B.A., Sutton, M.A., Dawicke, D.S., and Newman, J.C., Jr., 1995a, "An Experimental Study of CTOD for Mode I/Mode II Stable Crack Growth in Thin 2024-T3 Aluminum Specimens," *Fracture Mechanics: 26th Volume*, ASTM STP 1256.

Amstutz, B.A., Sutton, M.A., Dawicke, D.S., and Boone, M.L., 1995b, "Effects of Mixed Mode I/II Loading and Grain Orientation on Crack Initiation and Stable Tearing in 2024-T3 Aluminum," *Fatigue and Fracture Mechanics: 27th Volume*, ASTM STP 1296.

Anderson, H., 1973, "A Finite Element Representation of Stable Crack Growth," *Journal of the Mechanics and Physics of Solids*, Vol 21, pp. 337-356.

Anderson, T.L., 1995, *Fracture Mechanics, Fundamentals and Applications*, 2nd Ed., CRC Press, Boca Raton.

Bakuckas, J.G., Jr., Tan, T.M., Lau, A.C.W., and Awerbuch, J., 1993, "A Numerical Model for Predicting Crack Path and Modes of Damage in Unidirectional Metal Matrix Composites," *Journal of Reinforced Plastics and Composites*, Vol. 12, March 1993.

Bathe K.J., 1996, *Finite Element Procedures*, Prentice Hall, Englewood Cliffs, NJ.

Brown, S.B., and Song, H., 1993, "Rezoning and Dynamic Substructuring Techniques in FEM Simulations of Welding Processes," *Journal of Engineering for Industry*, Vol. 115, pp. 415-423, November 1993.

Camacho, G.T. and Oritz, M., 1996, "Computational Modeling of Impact Damage in Brittle Materials," *International Journal of Solids and Structures*, Vol.33, No.20-22, pp.2899-2938..

Chao, Y.J. and Liu, S., 1998, "On the Failure of Cracks Under Mixed-Mode Loads," *International Journal of Fracture*, Vol. 87, No. 3, pp. 201-223.

Chavez, P.F., 1983, "Automatic Procedures in Evolutionary Finite Element Calculations: Restoration of Deteriorated Meshes, Data Transfer Between Meshes, and Mesh Refinement," Ph.D. Thesis, Cornell University, Ithaca, New York, January 1983.

Crisfield M.A., 1991, *Non-linear Finite Element Analysis of Solids and Structures*, Wiley, West Sussex, England.

Dalle Donne, C. and Döker, H., 1997, "Plane Stress Crack Resistance Curves of and Inclined Crack under Bi-Axial Loading," *Multi-Axial Fatigue and Deformation Testing Techniques, ASTM STP 1280*, pp. 243-263.

Dawicke, D.S. and Newman, J.C., Jr., 1997, "Evaluation of Fracture Parameters for Predicting Residual Strength of Multi-site Damage," First Joint DoD/FAA/NASA conference on Aging Aircraft, Ogden, Utah, July 8-10.

Dawicke, D.S. and Newman, J.C., Jr., 1998, "Residual Strength Predictions for Multiple Site Damage Cracking Using a Three-Dimensional Finite Element Analysis and a CTOA Criterion," Submitted for Publication in *Fatigue and Fracture Mechanics: 29th Volume, ASTM STP 1321.*

Dawicke, D.S. and Sutton, M.A., 1993, "Crack Tip Opening Angle Measurements and Crack Tunneling Under Stable Tearing in Thin Sheet 2024-T3 Aluminum Alloy," NASA CR-191523.

Dawicke, D.S., 1996, "Residual Strength Predictions Using a CTOA Criterion," FAA-NASA Symposium on Continued Airworthiness of Aircraft Structures, Atlanta, GA, August 1996.

Dawicke, D.S., 1997, Personal communication, NASA Langley Research Center, Hampton, Virginia.

de Koning, A.U., 1977, "A Contribution to the Analysis of Quasi Static Crack Growth in the Sheet Materials," in *Fracture 1977,* Proceedings of the 4th International Conference on Fracture, Vol. 3, pp. 25-31.

Demofonti, G. and Rizzi, L., 1991, "Experimental Evaluation of CTOA in Controlling Unstable Ductile Fracture Propagation," *ESIS Pub. 9*, pp. 693-703.

Deng, X., 1990, "Dynamic Crack Propagation in Elastic-Plastic Solids," Ph.D. Thesis, California Institute of Technology, Pasadena, CA.

Erdogan, F. and Sih, G.C., 1963, "On the Crack Extension in Plates Under Plane Loading and Transverse Shear," *Journal of Basic Engineering*, December, pp. 519-527.

Espinosa, H.D., Emore, G., and Zavattieri, P., 1996, "Computational Modeling of Geometric and Material Nonlinearities with an Application to Impact Damage in Brittle Materials," *Advances in Failure Mechanisms in Brittle Materials*, ASME AMD-Vol. 219, pp. 119-161.

Gerstle, W.H., 1986, "Finite and Boundary Element Modeling of Crack Propagation in Two- and Three-Dimensions using Interactive Computer Graphics," Ph.D. Thesis, Cornell University, Ithaca, NY.

Ghosal, A.K. and Narasmhan, R., 1994, "A Finite Element Analysis of mixed-mode Fracture Initiation by Ductile Failure Mechanisms," *Journal of Mechanics and Physics of Solids*, Vol. 42, No. 6, pp. 953-978.

Gondhalekar, S.R., 1992, "Development of a Software Tool for Crack Propagation analysis in Two-dimensional Layered Structures," Master's Thesis, Department of Mechanical Engineering, Kansas State University, Manhattan, KS.

Habraken, A.M. and Cescotto, S., 1990, "An Automatic Remeshing Technique for Finite Element Simulation of Forming Processes," *International Journal for Numerical Methods in Engineering*, Vol. 30, pp. 1503-1525.

Harris, C.E., 1990, "NASA Aircraft Structural Integrity Program," NASA TM 102637.

Harris, C.E., 1996, NASA Airframe Structural Integrity Working Group Meeting, NASA Langley, Hampton, VA, March 21-22, 1996.

Hill, R., *The Mathematical Theory of Plasticity*, Oxford University Press, London, 1950.

Hom, C.L. and McMeeking, R.M., 1980, "Large Crack Tip Opening in Thin Elastic-Plastic Sheets," *International Journal of Fracture*, Vol. 45, pp. 103-122.

Hughes, T.J.R., 1984, "Numerical Implementation of Constitutive Models: Rate-independent Deviatoric Plasticity," *Theoretical foundation for large-scale computations for nonlinear material behavior* (Mechanics of elastic and inelastic solids; 6), Nemat-Nasser, Asaro, and Hegemier eds., Martinus Nijhoff Publishers, Dordrecht, 1984.

Hutchinson, J.W., 1968, "Singular Behavior at the End of a Tensile Crack Tip in a Hardening Material," *Journal of the Mechanics and Physics of Solids*, 16, pp. 13-31, 1968.

Hutchinson, J.W. and Paris, P.C., 1979, "Stability analysis of J-Controlled Crack Growth," *ASTM STP 668*, pp. 37-64.

Inglis, C.E., 1913,"Stresses in a Plate Due to the Presence of Cracks and Sharp Corners," *Transactions of the Institute of Naval Architects*, Vol. 55, pp. 219-241, 1913.

Irwin, G.R., 1957,"Analysis of Stresses and Strains Near the End of a Crack Traversing a Plate," *Journal of Applied Mechanics*, Vol. 24, pp. 361-364.

James, M.A., 1997, " Residual Strength Calculations for Single and Multiple-Site Damage Cracks," First Joint DoD/FAA/NASA conference on Aging Aircraft, Ogden, Utah, July 8-10.

Kato, K., Lee, N.S., and Bathe, K.J., 1993, "Adaptive Finite Element Analysis of Large Strain Elastic Response," *Computers & Structures*, v 47, n 4/5 pp. 829-855.

Kfouri, A.P. and Brown, M.W., 1995, "A Fracture Criterion for Cracks under Mixed Mode Loading," *Fatigue and Fracture of Engineering Materials and Structures*, Vol. 18, No. 9, pp. 959-969.

Kfouri, A.P, 1996, "Crack Extension under Mixed-Mode Loading in an Anisotropic Mode-Asymmetric Material In Respect of Resistance to Fracture," *Fatigue and Fracture of Engineering Materials and Structures*, Vol. 19, No. 1, pp. 27-38.

Krieg R.D. and Key, S.W., 1976, "Implementation of a time independent plasticity theory into structural computer programs," *Constitutive Equations in Viscoplasticity: Computational and Engineering Aspects*, AMD-20, ed. J. A. Stricklin et al., ASME, New York, pp. 125-138.

Krieg, R.D. and Krieg D.B., 1977, "Accuracies of numerical solution methods for the elastic-perfectly plastic model," *Trans. ASME*, pp. 510-515, November.

Krishnan, S., 1994, "A Finite Element Model of Crack Growth in Layered Structures with Bending," Master's Thesis, Department of Mechanical Engineering, Kansas State University, Manhattan, KS.

Kuang, J.H. and Chen, Y.C., 1997, "The Tip Plastic Energy Applied to Ductile Fracture Initiation under Mixed-Mode Loading," *Engineering Fracture Mechanics*, Vol. 58, No. 1/2, pp. 61-70.

Lee, J., Liebowitz, H., Lee, K., 1996, "The Quest of a Universal Fracture Law Governing the Process of Slow Crack Growths" *Engineering Fracture Mechanics*, Vol. 55, No. 1, pp. 61-83.

Lee, K., Lee, J., Liebowitz, H., 1997, "Finite Element Analysis of the Slow Crack Growth Process in Mixed Mode Fracture," *Engineering Fracture Mechanics*, Vol. 56, No. 4, pp. 551-557.

Lim, I.L., Johnston, I.W., Choi, S.K., and Murti, V., 1992, "Improved Numerical Inverse Isoparametric Mapping Technique for 2D Mesh Rezoning", *Engineering Fracture Mechanics*, Vol. 41, No. 3, pp. 417-435, Feb 1992.

Lim, I.L., 1992, "Fracture Propagation in the Soft Rock," Ph.D. Thesis, Monash University, Australia.

Maccagno, T. and Knott, J., 1989, "The Fracture Behavior of PMMA in Mixed Modes I and II," *Engineering Fracture Mechanics*, Vol. 34, No. 1, pp. 65-86.

Maccagno, T. and Knott, J., 1991, "The Low Temperature Brittle Fracture Behavior of Steel in Mixed Modes I and II," *Engineering Fracture Mechanics*, Vol. 38, No. 2/3, pp. 111-128.

Maccagno, T.M. and Knott, J.F., 1992, "The Mixed Mode I/II Fracture Behaviour of Lightly Tempered HY130 Steel at Room Temperature, " *Engineering Fracture Mechanics*, Vol. 41, No. 6, pp. 805-820.

Maiti, S.K. and Mahanty, D.K., 1990, "Experimental and Finite Element Studies on Mode I and Mixed Mode (I and II) Stable Crack Growth--II. Finite Element Analysis," *Engineering Fracture Mechanics*, Vol. 37, No. 6, pp. 1251-1275.

Malvern, L.E., 1969, *Introduction to the Mechanics of a Continuous Medium*, Prentice Hall.

Maurisch, T.D. and Ortiz, O., 1995, "A Finite Element Study of Chip Formation in High Speed Machining," MED-Vol. 2-1/MH-Vol. 3-1, Manufacturing Science and Engineering, ASME, pp. 245-258.

McMeeking, R.M. and Parks, D.M., 1979, "On Criteria for J-Dominance of Crack Tip Fields in Large-Scale Yielding," *ASTM STP 668*, American Society for Testing and Materials, Philadelphia, pp. 175-194, 1979.

Nakagaki, M., Chen, W.H., and Atluri, S.N., 1979, " A Finite-Element Analysis of Stable Crack Growth – I," *Elastic-Plastic Fracture, ASTM STP 668*, J.D. Landes, J.A. Begley and G.A. Clarke, Eds, American Society for Testing and Materials, pp. 195-213.

Newman, J.C., Jr., 1974, "Finite-Element Analysis of Fatigue Crack Propagation—Including the Effects of Crack Closure," Ph.D. Thesis, Virginia Polytechnic Institute and State University, Blacksburg, VA.

Newman, J.C., Jr., Booth, B.C., and Shivakumar, K.N., 1988, "An Elastic-Plastic Finite-Element Analysis of the *J*-resistance Curve using a CTOD Criterion, " *Fracture Mechanics: Eighteenth Symposium, ASTM STP 945*, D.T. Read and R.P. Reed, Eds., American Society for Testing and Materials, Philadelphia, pp. 665-685.

Newman, J.C., Jr., Dawicke, D.S., and Bigelow, C.A., 1992, "Finite-element Analyses and Fracture Simulation in Thin-Sheet Aluminum Alloy," NASA TM 107662.

Newman, J.C., Jr., Bigelow, C.A., and Shivakumar, K.N., 1993a, "Three-Dimensional Elastic-Plastic Finite-Element Analyses of Constraint Variations in Cracked Bodies, " *Engineering Fracture Mechanics*, Vol. 46, No. 1, pp. 1-13.

Newman, J.C., Jr., Dawicke, D.S., Sutton, M.A., and Bigelow, C.A., 1993b, "A Fracture Criterion for Widespread Cracking in Thin-Sheet Aluminum Alloys," ICAF 17, International Committee on Aeronautical Fatigue, pp. 443-468.

Ortiz, M. and Popov, E.P., 1985, "Accuracy and stability of integration algorithms for elastoplastic constitutive relations," *International Journal for Numerical Methods in Engineering*, Vol. 21, No. 9, pp. 1561-1576.

Ponthot, J.P. and Hogge, M., 1991, "The Use of the Eulerian-Lagrangian FEM in Metal Forming Applications Including Contact and Adaptive Mesh, " *Advances in Finite Deformation Problems in Materials Processing and Structures*, AMD-Vol. 125, ASME.

Potyondy, D.O., 1993, "A Software Framework for Simulating Curvilinear Crack Growth in Pressurized Thin Shells." Ph.D. Thesis, Cornell University, Ithaca, New York.

Rice, J.R., 1968, "A Path Independent Integral and the Approximate Analysis of Strain Concentrations by Notches and Cracks," *ASME Journal of Applied Mechanics*, Vol. 35, pp. 379-386.

Rice, J.R. and Rosengren, G.F., 1968, "Plane Strain Deformation near a Crack tip in a Power-Law Hardening Material," *Journal of the Mechanics and Physics of Solids*, Vol. 16, pp. 13-31.

Roy, S., Dexter, R.J., and Fossum, A.F., 1993, "A Computational Procedure for the Simulation of Ductile Fracture with Large Plastic Deformation," *Engineering Fracture Mechanics*, Vol. 45, No. 2, pp. 277-293.

Saouma, V.E. and Ingraffea, A.R., 1981, "Fracture Analysis of Discrete Cracking," Colloquium on Advanced Mechanics of Reinforced Concrete, International Association of Bridge and Structural engineers, Delft, June 1981, pp. 393-416.

Schreyer, H.L., Kulak, R.F. and Kramer, J. M., 1979, "Accurate numerical solutions for elasto-plastic models," *ASME Journal of Pressure Vessel Technology*, 101, 226-234.

Sekhon, G.S. and Chenot, J.L., 1993, "Numerical Simulation of Continuous Chip formation During Non-Steady Orthogonal Cutting," *Engineering Computations*, Vol. 10, pp. 31-48.

Shan, G.X., Kolednik, O., Stüwe, H.P, and Fischer, D.F.,1992, "A Substitution Method for 3D Elastic-Plastic FE Analysis of Fracture Mechanics Specimens," *Engineering Fracture Mechanics*, Vol. 41, No. 5, pp. 625-633.

Shan, G.X., Kolednik, O., and Fischer, D.F., 1994, "A Numerical Study on the Influence of Geometry Variations on Stable Crack Growth in CT Specimens for Different Materials," *Constraint Effects in Fracture: Theory and Applications, ASTM STP 1244,* Mark Kirk and Ad Bakker Eds., American Society for Testing and Materials, Philadelphia.

Shivakumar, K.N. and Newman, J.C., Jr., 1990, "ZIP3D - An Elastic-Plastic Finite Element Analysis Program for Cracked Bodies," NASA TM-102753.

Simo, J.C. and Taylor, R.L., 1985, "Consistent tangent operators for rate-independent elasto-plasticity," *Computer Methods in Applied Mechanics and Engineering*, Vol. 48, pp. 101-118.

Sneddon, I.N., 1946, "The Distribution of Stress in the Neighborhood of a Crack in an Elastic Solid," *Proceedings, Royal Society of London*, Vol. A-187, pp. 229-260.

Sommer, E. and Aurich, D., 1991, "On the Effect of Constraint on Ductile Fracture," *Proceedings of the European Symposium on Elastic-Plastic Fracture Mechanics*, ESIS/EGF Pub. 9, pp. 141-175.

Sutton, M.A., Zhao, W., Boone, M.L., Reynolds, A.P., and Dawicke, D.S., 1997, "Prediction of crack growth direction for mode I/II loading using small-scale yielding and void initiation/growth concepts," *International Journal of Fracture*, No. 83, pp. 275-290.

Swenson, D.V., 1985, "Modeling Mixed-Mode Dynamic Crack Propagation using Finite Elements," Ph.D. Thesis, Cornell University, Ithaca, NY.

Swift, T., 1993, "Widespread Fatigue Damage Monitoring Issues and Concerns," 5th International Conference on Structural Airworthiness of New and Aging Aircraft."

Wawrzynek, P.A. and Ingraffea, A.R., 1987, "Interactive Finite element analysis of Fracture Processes: An integrated Approach," *Theoretical and Applied Fracture Mechanics*, No. 8, pp. 137-150.

Wells, A.A., 1961, "Application of Fracture Mechanics at and Beyond General Yielding, " *British Welding Journal*, Vol. 11, pp. 563-570.

Westergaard, H.M., 1939, "Bearing Pressures and Cracks," *Journal of Applied Mechanics*, Vol. 6. , pp. 49-53.

Williams, M.L., 1957, "On the Stress Distribution at the base of a Stationary Crack, " *Journal of Applied Mechanics*, Vol. 24, pp. 109-114.

Yamada, T., 1993, "A Rezoning Procedure for Finite element Analysis of Rubber-like Materials," Proceedings of the 5th International Conference on Computing and Building Engineering, ASCE, pp. 327-334.

Equilibrium Equations

In this section we consider the equilibrium of a general body and use the principle of virtual displacements to derive the finite element equations. The derivation follows from Malvern (1969) and Bathe (1996). Figure A.1 shows the body under consideration. The displacement is prescribed on S_u and tractions prescribed on S_f.

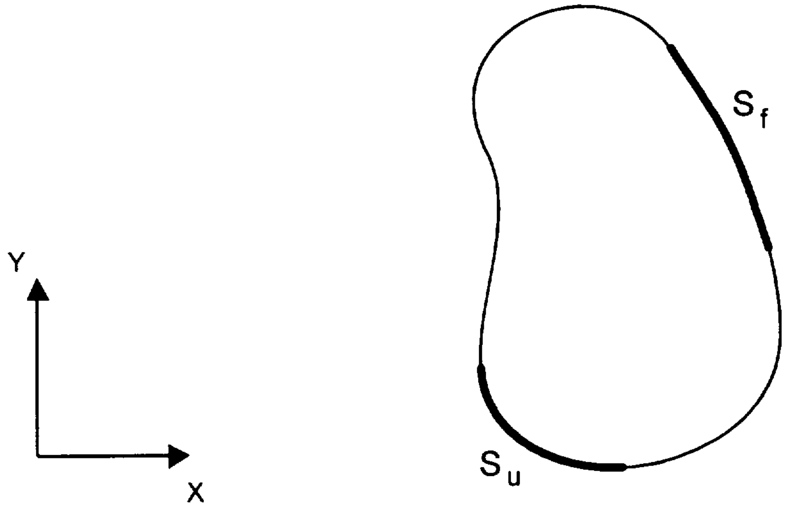

Figure A.1: A body in two-dimensions with prescribed displacements and tractions.

The differential equations that describe the problem are equilibrium:

$$\sigma_{ij,j} + f_i^B = 0, \tag{A.1}$$

throughout the body, with the natural (force) boundary conditions:

$$\sigma_{ij} n_j = f_i^B, \tag{A.2}$$

on S_f, and the essential (displacement) boundary conditions:

$$u_i = u_i^{S_u}, \tag{A.3}$$

on S_u.

We consider now any arbitrary, continuous virtual displacement δu_i satisfying $\delta u_i = 0$ on S_u. Then,

$$\int_V \left(\sigma_{ij,j} + f_i^B\right)\delta u_i \, dV = 0 \tag{A.4}$$

Since δu_i is arbitrary, (A.4) can be satisfied if and only if the term in parenthesis is zero. Using the chain rule:

$$\left(\sigma_{ij}\delta u_i\right)_{,j} = \sigma_{ij,j}\delta u_i + \sigma_{ij}\delta u_{i,j},$$

we have

$$\int_V \left\{(\sigma_{ij}u_i)_{,j} - \sigma_{ij}\delta u_{i,j} + f_i^B \delta u_i\right\} dV = 0. \tag{A.5}$$

Next, using the divergence theorem:

$$\int_V (\sigma_i \delta u_i)_{,j} = \int_S (\sigma_{ij}\delta u_i)\, n_j \, dS,$$

(A.5) can be rewritten as

$$\int_V (-\sigma_{ij}\delta u_{ij} + f_i^B \delta u_i) dv + \int_S (\sigma_{ij}\delta u_i)\, n_j \, dS = 0. \tag{A.6}$$

By introducing the boundary conditions (A.2) and (A.3),

$$\int_V (-\sigma_{ij}\delta u_{i,j} + f_i^B \delta u_i) dV + \int_{S_f} f_i^{S_f} \delta u_i^{S_f} dS = 0. \tag{A.7}$$

Also, because of symmetry of the stress tensor, (σ_{ij}=σ_{ji}), we have,

$$\sigma_{ij}\delta u_{i,j} = \sigma_{ij}\left\{\tfrac{1}{2}(\delta u_{i,j} + \delta u_{j,i}\right\} = \sigma_{ij}\delta\, \varepsilon_{ij}. \tag{A.8}$$

So the statement of virtual displacements becomes,

$$\int_V \sigma_{ij}\delta\, \varepsilon_{ij} dV = \int_V f_i^B \delta u_i dV + \int_{S_f} f_i^{S_f} \delta u_i^{S_f} dS. \tag{A.9}$$

Equation (A.9) is valid for general equilibrium as long as a statically admissible stress distribution is defined, and as long as a kinematically admissible displacement solution is defined. The current work is limited to small strain, small rotation, but materially non-linear static equilibrium. In this case, the current volume corresponds to the initial volume, and all stresses and strains are referred in the initial volume. The standard small strain measure is used:

$$\varepsilon_{ij} = \tfrac{1}{2}\left(u_{i,j} + u_{j,i}\right).$$

We will now derive the governing finite element equations. We begin by discretizing (A.9) in the usual manner for finite elements (Bathe, 1996). First isoparametric interpolation functions for the displacements are defined as:

$$\mathbf{u}^{(m)} = \mathbf{N}^{(m)}\mathbf{U} \tag{A.10}$$

where $\mathbf{N}^{(m)}$ is the displacement interpolation matrix and $\mathbf{U}$ are the element nodal displacements for element m. The strains are interpolated using

$$\boldsymbol{\varepsilon}^{(m)} = \mathbf{B}^{(m)}\mathbf{U} \tag{A.11}$$

where $\mathbf{B}^{(m)}$ is the strain-displacement matrix obtained by the differentiating the displacement interpolation matrix, $\mathbf{N}^{(m)}$.

We can write equation (A.9) in a discretized form for a single element, where the contribution of each element is added to the global system of equations:

$$\int_{V^{(m)}} \delta\boldsymbol{\varepsilon}^{(m)\mathrm{T}}\boldsymbol{\sigma}^{(m)}dV^{(m)} = \int_{S^{(m)}} \delta\mathbf{u}^{S^{(m)}\mathrm{T}}\mathbf{f}^{S^{(m)}}dS^{(m)}, \tag{A.12}$$

where for brevity the body force term has been omitted. Substituting for the virtual strains and displacements,

$$\delta\mathbf{U}^{\mathrm{T}}\left\{\int_{V^{(m)}} \mathbf{B}^{(m)\mathrm{T}}\boldsymbol{\sigma}^{(m)}dV^{(m)}\right\} = \delta\mathbf{U}^{\mathrm{T}}\left\{\int_{S^{(m)}} \mathbf{N}^{(m)}\mathbf{f}^{S^{(m)}}dS^{(m)}\right\}, \tag{A.13}$$

where $\delta\mathbf{U}$ is the variation of the displacement vector for the total domain. Since $\delta\mathbf{U}$ is arbitrary (and dropping the superscript for the element, and still considering only one element):

$$\int_V \mathbf{B}^{\mathrm{T}}\boldsymbol{\sigma}\, dV = \int_S \mathbf{N}\mathbf{f}^S dS. \tag{A.14}$$

A.1 Incremental Equations of Equilibrium

The problems of interest here are commonly called *quasi-static*; that is, there are no inertial effects. However, when nonlinear effects such as plasticity are considered, the solution to the problem may be loading path dependent, and so, dependent on a *pseudo-time.*

We introduce here the notion of time to represent equilibrium at discrete time points (eg. *0, Δt, 2Δt*) where *Δt* is the increment in time. We assume that the full system state has been obtained up to time *t*, and we desire the solution at time *t+Δt*. Typically for quasi-static problems the time increment represents an increment in the loading conditions.

A.1.1 Newton-Raphson Scheme

One approach to solving non-linear finite element equations is the Newton-Raphson iterative scheme. Following the development in Bathe (1996), we can rewrite (A.14) as

$$\mathbf{R}(\mathbf{U}^*) = {}^{t+\Delta t}\mathbf{F}_e(\mathbf{U}^*) - {}^{t+\Delta t}\mathbf{F}_i(\mathbf{U}^*) = \mathbf{0}, \tag{A.15}$$

where ${}^{t+\Delta t}\mathbf{F}_e(\mathbf{U}^*)$ is the external applied force vector, and ${}^{t+\Delta t}\mathbf{F}_i(\mathbf{U}^*)$ is the nodal internal force vector evaluated from the element stresses. At equilibrium $\mathbf{R}(\mathbf{U}^*) = \mathbf{0}$.

If we assume that the previous iterative solution ${}^{t+\Delta t}\mathbf{U}^{(j-i)}$ is available, then a Taylor series expansion gives:

$$\mathbf{R}(\mathbf{U}^*) = \mathbf{R}({}^{t+\Delta t}\mathbf{U}^{(j-i)}) + \left[\frac{\partial \mathbf{R}}{\partial \mathbf{U}}\right]_{{}^{t+\Delta t}\mathbf{U}^{(i-1)}} (\mathbf{U}^* - {}^{t+\Delta t}\mathbf{U}^{(j-1)}) + H.O.T. \tag{A.16}$$

Using (A.15) we can rewrite (A.16) as (neglecting higher-order terms):

$$-\left.\frac{\partial \mathbf{R}}{\partial \mathbf{U}}\right|_{{}^{t+\Delta t}\mathbf{U}^{(i-1)}} (\mathbf{U}^* - {}^{t+\Delta t}\mathbf{U}^{(j-1)}) = {}^{t+\Delta t}\mathbf{F}_e - {}^{t+\Delta t}\mathbf{F}_i^{(j-1)} \tag{A.17}$$

The update equation is:

$$-{}^{t+\Delta t}\mathbf{K}^{(j-1)}\delta\mathbf{U}^{(i)} = {}^{t+\Delta t}\mathbf{F}_e - {}^{t+\Delta t}\mathbf{F}_i^{(j-1)}, \qquad \text{(A.18)}$$

where ${}^{t+\Delta t}\mathbf{K}^{(i-1)}$ is the current tangent stiffness matrix:

$${}^{t+\Delta t}\mathbf{K}^{(i-1)} = \left[\frac{\partial \mathbf{F}_i}{\partial \mathbf{U}}\right]_{{}^{t+\Delta t}\mathbf{U}^{(i-1)}}. \qquad \text{(A.19)}$$

The iterative update to the displacement solution is

$${}^{t+\Delta t}\mathbf{U}^{(i)} = {}^{t+\Delta t}\mathbf{U}^{(i-1)} + \delta\mathbf{U}^{(j)}. \qquad \text{(A.20)}$$

Several variations on the Newton iterative scheme exist. If (A.19) is updated at each iteration the scheme is typically referred to as the full Newton method; if (A.19) is updated periodically, the scheme is typically referred to as the Modified Newton method. If only the initial value of (A.19) is used, the scheme is typically referred to as the initial stress method.

Efficiency concerns usually dictate which of the three is employed. The initial stress method requires many more iterations, but the Full-Newton and Modified-Newton methods require that (A.19) be evaluated and inverted more than once. A trade off usually exists between the convergence rate without updates to (A.19), compared to the cost of reforming and inverting (A.19). For small strain plasticity with no other nonlinearities, such as contact conditions, the initial stress method is usually adequate. The current implementation uses the initial stress method.

A.2 Incremented Iterative Solution

Accurate solutions of the nonlinear finite element equations rely not only on satisfaction of equilibrium, but also on accurate integration of the incremental elastic-plastic stress-strain constitutive relation.

Crisfield (1991) provides a good description of implementing the stress update in terms of either incremental or iterative strains. Essentially, the choice lies in what reference state is used for the incremental update, and how the state variables are managed during the update. Crisfield references several approaches; only two are discussed here, with the most robust and conservative of the two being implemented.

Listing A.1 shows the basic Newton steps for the iterative strain update method, where $\delta\mathbf{p}$ is the iterative displacement computed from the inverse tangent stiffness matrix, $\mathbf{K}_t^{-1}$ and the residual (out-of-balance) load vector $\mathbf{g}$. The iterative strain update $\delta\varepsilon$ is calculated from the iterative displacement update, and the iterative stress update from the iterative strain update. All displacement strain, and stress variables reference the previous iterative state (which is *not* in equilibrium).

Listing A.2 shows the basic Newton steps for the incremental strain update method, where the iterative displacement $\delta\mathbf{p}$ is calculated as before. The algorithm departs here from the previous algorithm, in that the iterative displacement is accumulated into the incremental displacement, $\Delta\mathbf{p}$, which is referred to the previous equilibrium state.

```
1. $\delta\mathbf{p} = -\mathbf{K}_t^{-1}\mathbf{q}$
2. $\delta\varepsilon = \mathbf{B}\delta\mathbf{p}$                    $\delta\boldsymbol{\sigma} = \mathbf{C}_t(\boldsymbol{\sigma})\,\delta\varepsilon$
3. $\boldsymbol{\sigma}_n = \boldsymbol{\sigma}_o + \delta\boldsymbol{\sigma}$                    $\boldsymbol{\sigma}_o = \boldsymbol{\sigma}_n$
4. Repeat 1-3 until convergence
```

Listing A.1: Iterative strain update (Crisfield, 1991).

Then the incremental strains, and incremental stresses can be calculated with respect to the previous equilibrium state. The new trial stress, σ_n, is calculated from the old equilibrium stress, σ_o, and the stress increment referred to the previous equilibrium state, $\Delta\boldsymbol{\sigma}$. Once equilibrium is satisfied the trial stress is saved as the current stress.

```
1. $\delta\mathbf{p} = -\mathbf{K}_t^{-1}\mathbf{q}$                    $\Delta\mathbf{p} = \Delta\mathbf{p} + \delta\mathbf{p}$
2. $\Delta\varepsilon = \mathbf{B}\Delta\mathbf{p}$                    $\Delta\boldsymbol{\sigma} = \mathbf{C}_t(\boldsymbol{\sigma})\,\Delta\varepsilon$
3. $\boldsymbol{\sigma}_n = \boldsymbol{\sigma}_o + \Delta\boldsymbol{\sigma}$
4. Repeat 1-3 until convergence
5. $\boldsymbol{\sigma}_o = \boldsymbol{\sigma}_n$
```

Listing A.2: Incremental strain update (Crisfield, 1991).

Figure 2 shows schematically for a one-dimensional problem a potential effect of using iterative vs. incremental updates. Point A represents a converged equilibrium state. Point B is determined from the first tangential iteration. In Figure 2(a) the second iteration produces point C, since the strain increment was negative, and Point B was used as a reference. In contrast, in Figure 2(b), Point C is correctly determined by using the strain increment referred to Point A, so the negative strain iteration simply reduced the total strain increment.

A.3 Implementation

Bathe (1996) outlines nicely the steps necessary to implement the incremental Newton-Raphson solution scheme. Suppose that at time t equilibrium is established. The stresses ${}^{t}\sigma$, and strains ${}^{t}\varepsilon$, and internal material parameters ${}^{t}\kappa$, are known. Using (A.18), the initial displacement update (iteration i=0), as

$$\delta \mathbf{U}^{(1)} = \left[{}^{t}\mathbf{K}^{(o)}\right]^{-1}\left({}^{t+\Delta t}\mathbf{F}_e - {}^{t+\Delta t}\mathbf{F}_i^{(o)}\right), \tag{A.21}$$

where ${}^{t+\Delta t}\mathbf{F}_e$ is the current external applied load and ${}^{t+\Delta t}\mathbf{F}_i^{(0)} = {}^{t}\mathbf{F}_i^{(n)}$, the converged internal forces from the previous load step at the final convergence iteration (n). The displacent increments are updated using (A.20), and element strain increments are calculated using

$$ {}^{t+\Delta t}\Delta\boldsymbol{\varepsilon}^{(i)} = \mathbf{B}\ {}^{t+\Delta t}\Delta\mathbf{U}^{(i)}. \tag{A.22}$$

For elastic behavior the strains directly give the stresses using the appropriate stress-strain constitutive matrix. For inelastic behavior the stresses must be integrated as

$$ {}^{t+\Delta t}\boldsymbol{\sigma}^{(i-1)} = {}^{t}\boldsymbol{\sigma} + \int_{t}^{t+\Delta t} \delta\boldsymbol{\sigma}^{(i-1)}, \tag{A.23}$$

and the tangent stress-strain matrix ${}^{t+\Delta t}\mathbf{D}^{(i-1)}$ must be evaluated consistent with the stress integration process. The stress integration, equation (A.21), is described in Appendix B.

Once the stresses are updated, the nodal variables are updated using (A.18) as

$$\delta\ {}^{t+\Delta t}\mathbf{U}^{(i)} = \left[{}^{t+\Delta t}\mathbf{K}^{(i-1)}\right]\ {}^{t+\Delta t}\mathbf{R}^{(i-1)} \tag{A.22}$$

$$ {}^{t+\Delta t}\Delta\mathbf{U}^{i} = {}^{t+\Delta t}\Delta\mathbf{U}^{i-1} + {}^{t+\Delta t}\delta\mathbf{U}^{i}. \tag{A.23}$$

The total strains are evaluated as

$$ {}^{t+\Delta t}\boldsymbol{\varepsilon}^{(i)} = \mathbf{B}\left({}^{t+\Delta t}\mathbf{U}^{(i)} + {}^{t+\Delta t}\Delta\mathbf{U}^{(i)}\right). \tag{A.24}$$

The internal forces ${}^{t+\Delta t}\mathbf{F}_i^{(i)}$ are evaluated at the current trial stress state. Evaluating

$$
{}^{t+\Delta t}\mathbf{R}^{(i-1)} = {}^{t+\Delta t}\mathbf{F}_e^{(i)} - {}^{t+\Delta t}\mathbf{F}_i^{(i)} \tag{A.25}
$$

ensures that any residual out-of-balance forces from the previous load step are included in the current iterations, thus preventing drift from the true equilibrium path, as might be experienced using a traditional initial stress formulation.

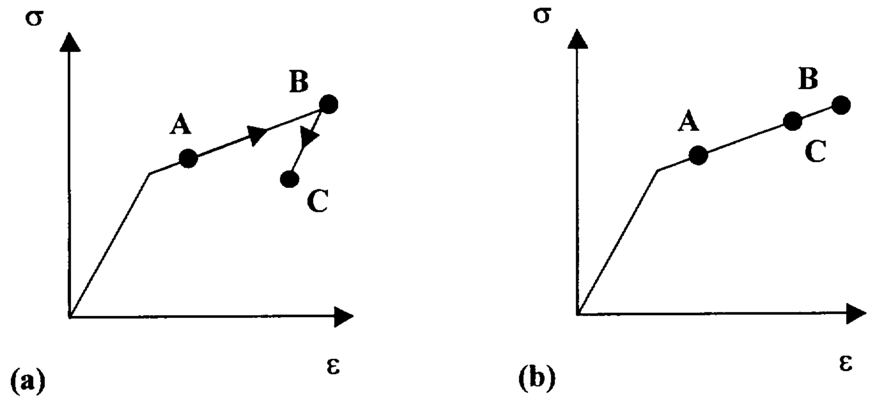

Figure A.2: Schematic of (a) iterative and (b) incremental strain update (Crisfield, 1991).

Appendix B

Plasticity Rate Equations

The formulation of the plasticity rate equations follows in a similar manner to any of a number of finite element texts (Bathe, 1996; Crisfield, 1991). The plasticity rate equations are formulated here for the von Mises yield criterion. The yield function for isotropic strain hardening is:

$$f(\boldsymbol{\sigma}, \varepsilon_{ps}) = \sigma_e - \sigma_o(\varepsilon_{ps}) \tag{B.1}$$

where $\boldsymbol{\sigma}$ is the current stress, ε_{ps} is the effective plastic strain σ_e is the effective, or von Mises stress, and σ_o is the yield stress. The strain rate is linearly decomposed into elastic and plastic parts:

$$\dot{\boldsymbol{\varepsilon}} = \dot{\boldsymbol{\varepsilon}}_e + \dot{\boldsymbol{\varepsilon}}_p \tag{B.2}$$

where $\dot{\boldsymbol{\varepsilon}}_e$ is the elastic strain rate and $\dot{\boldsymbol{\varepsilon}}_p$ is the plastic strain rate. The flow rule is assumed to be associative:

$$\dot{\boldsymbol{\varepsilon}}_p = \dot{\lambda}\frac{\partial f}{\partial \boldsymbol{\sigma}} = \dot{\lambda}\,\mathbf{a} \tag{B.3}$$

The linear constitutive relation for the elastic stress rate is assumed to hold:

$$\dot{\sigma} = \mathbf{D}(\dot{\varepsilon} - \dot{\varepsilon}_p) = \mathbf{D}(\dot{\varepsilon} - \dot{\lambda}\mathbf{a}) \tag{B.4}$$

For isotropic strain hardening the equivalent plastic strain is

$$\varepsilon_{ps} = \int \dot{\varepsilon}_{ps} \tag{B.5}$$

For plastic flow to occur (tangency condition) the stresses must remain on the yield surface:

$$\dot{f} = \frac{\partial f}{\partial \boldsymbol{\sigma}}^{\mathrm{T}} \dot{\boldsymbol{\sigma}} + \frac{\partial f}{\partial \sigma_{o}}^{\mathrm{T}} \frac{\partial \sigma_o}{\partial \varepsilon_{ps}} \dot{\varepsilon}_{ps} \tag{B.6}$$

For the von Mises yield function under plane stress

$$\sigma_o = \left(\sigma_x{}^2 + \sigma_y{}^2 - \sigma_x\,\sigma_y + 3\sigma_{xy}{}^2\right)^{1/2} \tag{B.7}$$

$$\dot{\varepsilon}_{ps} = \tfrac{2}{\sqrt{3}}\left(\dot{\varepsilon}_{px}^2 + \dot{\varepsilon}_{py}^2 + \dot{\varepsilon}_{px}\dot{\varepsilon}_{py} + \tfrac{1}{4}\dot{\gamma}_{pxy}^2\right)^{1/2} \tag{B.8}$$

Now the flow rule becomes

$$\dot{\boldsymbol{\varepsilon}}_p = \dot{\lambda}\frac{\partial f}{\partial \boldsymbol{\sigma}} = \begin{Bmatrix} \\ \dot{\varepsilon}_{py} \\ \dot{\varepsilon}_{pxy} \end{Bmatrix} = \frac{\dot{\lambda}}{2\sigma_e}\begin{Bmatrix} \\ 2\sigma_y - \sigma_x \\ 6\sigma_{xy} \end{Bmatrix} \tag{B.9}$$

Under uniaxial tension, σ_x, $\dot{\varepsilon}_{py} = \dot{\varepsilon}_{pz} = {}^{-}\!1/2\,\dot{\varepsilon}_{px}$, so that there is no plastic volume change; so, $\dot{\varepsilon}_{ps} = \dot{\varepsilon}_{px}$, and $\sigma_e = \sigma_o = \sigma_x$. Consequently, the relationship between σ_o and $\dot{\varepsilon}_{ps}$ can be taken from the uniaxial stress / plastic strain relationship.

$$H' = \frac{\partial \sigma_o}{\partial \varepsilon_{ps}} = \frac{\partial \sigma_o}{\partial \varepsilon_{ps}} = \frac{E_t}{1 - {}^{E_t}\!/_{E}} \tag{B.10}$$

Now the tangency condition is

$$\dot{f} = \frac{\partial f}{\partial \boldsymbol{\sigma}}^{\mathrm{T}} \dot{\boldsymbol{\sigma}} + \frac{\partial f}{\partial \sigma_{\mathrm{o}}}^{\mathrm{T}} \frac{\partial \sigma_o}{\partial \varepsilon_{ps}} \dot{\boldsymbol{\varepsilon}}_{ps} = \mathbf{a}^{\mathrm{T}}\dot{\boldsymbol{\sigma}} - H'\dot{\boldsymbol{\varepsilon}}_{ps} = 0 \tag{B.11}$$

Substituting (B.9) into (B.8) gives

$$\dot{\varepsilon}_{ps} = \dot{\lambda} \tag{B.12}$$

and substituting (B.12) into (B.11) gives

$$f = \mathbf{a}^{\mathrm{T}}\dot{\boldsymbol{\sigma}} - A'\dot{\lambda} \tag{B.13}$$

where $A' = A'(\varepsilon_{ps})$ is substituted for H' and is in general a non-linear hardening modulus that is a function of the plastic strain. Premultiplying (B.4) by $\mathbf{a}^{\mathrm{T}}$ and substituting into (B.13) gives

$$\dot{\lambda} = \frac{\mathbf{a}^{\mathrm{T}}\mathbf{D}\dot{\boldsymbol{\varepsilon}}}{\mathbf{a}^{\mathrm{T}}\mathbf{D}\mathbf{a} + A'} \tag{B.14}$$

and taking into account symmetry in **D**,

$$\dot{\boldsymbol{\sigma}} = \mathbf{D}_{ep}\dot{\boldsymbol{\varepsilon}} = \mathbf{D}\left(\mathbf{I} - \frac{\mathbf{a}\mathbf{a}^{\mathrm{T}}\mathbf{D}}{\mathbf{a}^{\mathrm{T}}\mathbf{D}\mathbf{a} + A'}\right)\dot{\boldsymbol{\varepsilon}} \tag{B.15}$$

This formulation cannot account for the Bauschinger effect induced by cyclic loading. The initial analyses under consideration require only monotonic loading, so the Bauschinger effect will not be introduced. A kinematic hardening model may be introduced at some later time to account for the 'kinematic shift' of the yield surface in this case.

B.1 Integrating the Plasticity Rate Equations

The analyses considered here are for quasi-static conditions and consider no dynamic effects, so the dotted quantities can be considered small changes. The time rate of change relations can then be written in the form $\mathrm{d}\varepsilon = \dot{\varepsilon}\mathrm{d}t$. The other dotted quantities can be considered similarly. For this section, the rate equations will be considered in this incremental form, rather than rate form.

Many algorithms are available for integrating the incremental form of the von Mises constitutive equations. Many are based on what has become known as the generalized trapezoidal rule (Ortiz and Popov, 1985; Crisfield, 1991). From the generalized trapezoidal rule can be derived the pure 'explicit' or 'forward-Euler' scheme, a mid-point algorithm, or an 'implicit' or 'backward-Euler' scheme. Accuracy of the integration algorithm is of prime concern, with efficiency also a concern. Krieg and Krieg (1977), Schreyer, et. al. (1979), Ortiz and Popov (1985), and De Borst and Feenstra (1990) all showed that for large step sizes the backward-Euler scheme is most accurate, and in certain cases is by far the most efficient, since for plane strain with linear hardening the backwards-Euler scheme degenerates into the well know radial return algorithm (Wilkins, 1964; Krieg and Key, 1976). The basic algorithm implemented uses an elastic predictor, normal corrector. Figure B.1 is a schematic of the elastic predictor, normal corrector implemented. The scheme uses the normal at the 'elastic trial point,' B. A first order expansion about point B of the yield function gives:

$$f = f_{\mathrm{B}} + \frac{\partial f}{\partial \boldsymbol{\sigma}}^{\mathrm{T}}\Delta\boldsymbol{\sigma} + \frac{\partial f}{\partial \varepsilon_{\mathrm{ps}}}\Delta\varepsilon_{\mathrm{ps}} = f_{\mathrm{B}} - \Delta\lambda\mathbf{a}_{\mathrm{B}}^{\mathrm{T}}\mathbf{C}\mathbf{a}_{\mathrm{B}} - \Delta\lambda A' \tag{B.16}$$

Solving for $\Delta\lambda$

$$\Delta\lambda = \frac{f_{\mathrm{B}}}{\mathbf{a}_{\mathrm{B}}^{\mathrm{T}}\mathbf{D}\mathbf{a}_{\mathrm{B}} + A'_{\mathrm{B}}} \tag{B.17}$$

Then the stresses at **C** are given by

$$\boldsymbol{\sigma}_{\mathrm{C}} = \boldsymbol{\sigma}_{\mathrm{B}} - \Delta\lambda \mathbf{D}\mathbf{a}_{\mathrm{B}} \tag{B.18}$$

For the 3-D (or plane strain or axisymmetric) von Mises with linear hardening, (B.18) corresponds to the radial-return algorithm, which is a special form of the backward-Euler algorithm. For non-linear hardening, or for plane stress, the stress at $\boldsymbol{\sigma}_{\mathrm{C}}$ will not necessarily lie on the yield surface, and iterations are required to satisfy the consistency condition.

The backward-Euler return implemented here comes from Crisfield (1991). A simple statement of the equation, referring to Figure B.1 is:

$$\boldsymbol{\sigma}_{\mathrm{C}} = \boldsymbol{\sigma}_{\mathrm{B}} - \Delta\lambda \mathbf{D}\mathbf{a}_{\mathrm{C}} \tag{B.19}$$

where $\boldsymbol{\sigma}_{\mathrm{B}}$ is the elastic trial stress and the initial value for $\boldsymbol{\sigma}_{\mathrm{C}}$ comes from the value in (B.18). An iterative method is required to solve equation (B.19), since the normal at the trial position B will not necessarily equal the final normal. A Newton type iterative scheme is implemented, where the residual vector of stresses, **r**, is written as:

$$\mathbf{r} = \sigma - \left(\sigma_{\mathrm{B}} - \Delta\lambda \mathbf{D}\mathbf{a}_{\mathrm{C}}\right) \tag{B.20}$$

and iterations reduce the residual to (almost) zero. The final stresses σ should satisfy the yield criterion, $f = 0$.

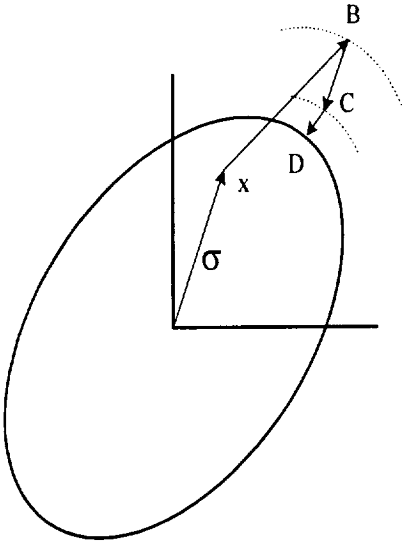

Figure B.1: Elastic predictor, normal return with correction to the yield surface for plane stress.

With the trial stresses σ_B kept fixed, a truncated Taylor series expansion is applied to produce a new residual, $\mathbf{r}_n$ as:

$$\mathbf{r}_n = \mathbf{r}_o + \dot{\boldsymbol{\sigma}} + \dot{\lambda}\mathbf{D}\mathbf{a} + \Delta\lambda\mathbf{D}\frac{\partial \mathbf{a}}{\partial \boldsymbol{\sigma}}\dot{\boldsymbol{\sigma}} \tag{B.21}$$

where $\dot{\sigma}$ is the change in σ and $\dot{\lambda}$ is the change in $\Delta\lambda$. Setting $\mathbf{r}_n$ to zero gives

$$\dot{\boldsymbol{\sigma}} = -\left(\mathbf{I} + \Delta\lambda\mathbf{D}\frac{\partial \mathbf{a}}{\partial \boldsymbol{\sigma}}\right)^{-1}\left(\mathbf{r}_o + \dot{\lambda}\mathbf{D}\mathbf{a}\right) = -\mathbf{Q}^{-1}\mathbf{r}_o - \dot{\lambda}\mathbf{Q}^{-1}\mathbf{D}\mathbf{a} \tag{B.22}$$

Also, a truncated series expansion on the yield function gives

$$f_n = f_{co} + \frac{\partial f}{\partial \boldsymbol{\sigma}}^{T}\dot{\boldsymbol{\sigma}} + \frac{\partial f}{\partial \varepsilon_{ps}}\dot{\varepsilon}_{ps} = f_{co} + \mathbf{a}_C^{T}\dot{\boldsymbol{\sigma}} - A'\dot{\lambda} = 0 \tag{B.23}$$

Solving for $\dot{\lambda}$ from (A 22) and (A 23) and dropping the subscript C gives

$$\dot{\varepsilon}_{ps} = \dot{\lambda} = \frac{f_o - \mathbf{a}^{T}\mathbf{Q}^{-1}\mathbf{r}_o}{\mathbf{a}^{T}\mathbf{Q}^{-1}\mathbf{D}\mathbf{a} + A'} \tag{B.24}$$

Substituting (B.24) into (B.22) gives the iterative change in the stress, and (B.24) is the iterative change in effective plastic strain. It is worth noting here that at each iteration the yield function is evaluated at $f_o = f_o(\varepsilon_{ps_B} + \Delta\varepsilon_{ps})$ and the hardening at $A' = A'(\varepsilon_{ps_B} + \Delta\varepsilon_{ps})$, where $\Delta\varepsilon_{ps}$ is the accumulated change in ε_{ps} from point B. The term $\partial\mathbf{a} / \partial\boldsymbol{\sigma}$ is conveniently derived as follows from the yield equation:

$$f = \sigma_e - \sigma_o = \left(\sigma_e^2\right)^{1/2} - \sigma_o \tag{B.25}$$

$$\frac{\partial f}{\partial \boldsymbol{\sigma}} = \mathbf{a} = \frac{1}{2\sigma_e}\frac{\partial\left(\sigma_e^2\right)}{\partial\boldsymbol{\sigma}} - \sigma_o \tag{B.26}$$

$$\frac{\partial \mathbf{a}}{\partial \boldsymbol{\sigma}} = \frac{1}{2\sigma_e}\frac{\partial^2\left(\sigma_e^2\right)}{\partial\boldsymbol{\sigma}^2} - \frac{1}{\sigma_e}\mathbf{a}\mathbf{a}^{\mathrm{T}} \tag{B.27}$$

B.2 Consistent Tangent Modulus

The current implementation of the equilibrium iterations uses the initial stiffness matrix in the modified Newton-Raphson scheme. If a full Newton scheme is required for accelerated convergence a tangent modular matrix that is fully consistent with the backward-Euler integration algorithm can significantly improve convergence. Simo and Taylor (1985) derived a tangent modular matrix that is fully consistent with the backward-Euler integration algorithm. Standard techniques would use the modular matrix of (B.15), which is inconsistent with the backward-Euler algorithm, and as such, does not provide the quadratic convergence associated with the Newton-Raphson method. More recently Crisfield (1991) derived a consistent tangent modular matrix based on the above equations for integrating the plasticity rate equations. This derivation begins with the expression for the backward-Euler algorithm:

$$\boldsymbol{\sigma} = \boldsymbol{\sigma}_{\mathrm{B}} - \Delta\lambda\mathbf{D}\mathbf{a} \tag{B.28}$$

where we drop the suffix C for the current configuration, but the suffix B is kept to indicate the elastic trial stress. Differentiation of (B.28) gives

$$\dot{\boldsymbol{\sigma}} = \mathbf{D}\dot{\boldsymbol{\sigma}} - \dot{\lambda}\mathbf{D}\mathbf{a} - \Delta\lambda\mathbf{D}\frac{\partial\mathbf{a}}{\partial\boldsymbol{\sigma}}\dot{\boldsymbol{\sigma}} \tag{B.29}$$

The last term of equation (B.29) is omitted from the derivation of the standard tangent modular matrix in (B.15). Now, from (B.29) we have

$$\dot{\boldsymbol{\sigma}} = \left(\mathbf{I} + \Delta\lambda\mathbf{D}\frac{\partial\mathbf{a}}{\partial\boldsymbol{\sigma}}\right)^{-1}\mathbf{D}\left(\dot{\boldsymbol{\varepsilon}} - \dot{\lambda}\mathbf{a}\right) = \mathbf{Q}^{-1}\mathbf{D}\left(\dot{\boldsymbol{\varepsilon}} - \dot{\lambda}\mathbf{a}\right) = \mathbf{R}\left(\dot{\boldsymbol{\varepsilon}} - \dot{\lambda}\mathbf{a}\right) \tag{B.30}$$

where the **Q** matrix appeared before in (B.22).

For $\dot{f}$ to remain on the yield surface it's value should be zero, so from (B.6) and (B.30)

$$\dot{f} = \mathbf{a}^{\mathrm{T}}\dot{\sigma} - A'\dot{\lambda} = \mathbf{a}^{\mathrm{T}}\mathbf{R}\dot{\varepsilon} - \dot{\lambda}\mathbf{a}^{\mathrm{T}}\mathbf{R}\mathbf{a} = 0 \tag{B.31}$$

Solving for $\dot{\lambda}$ and substituting into (B.30) gives

$$\dot{\sigma} = \mathbf{D}_{\mathrm{ct}}\dot{\varepsilon} = \left(\mathbf{R} - \frac{\mathbf{R}\mathbf{a}\mathbf{a}^{\mathrm{T}}\mathbf{R}^{\mathrm{T}}}{\mathbf{a}^{\mathrm{T}}\mathbf{R}\mathbf{a} + A'}\right)\dot{\varepsilon} \tag{B.32}$$

where account of the symmetry of **R** has been taken in deriving equations (B.32).

Appendix C

Plasticity Verification

This example demonstrates a number of FRANC2D/L features for a materially-nonlinear analysis, including the von Mises material model with linear isotropic hardening and nonproportional loading. A thin tube is first stressed in tension to the point of yielding and is then twisted under constant axial stress. A single material point is sufficient to model the problem. Figure C.1 shows the loading path.

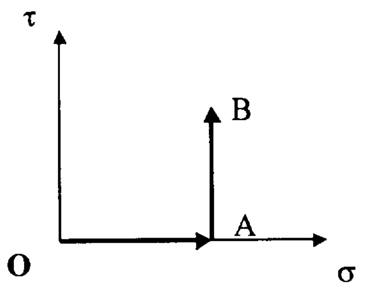

Point	σ	τ
O	0.0	0.0
A	26.25	0.0
B	26.25	24.0

Figure C.1: Loading path for the tension torsion example.

For linear isotropic hardening the Hill (1950) plasticity book gives the exact solution for the axial and shear strains as:

$$\varepsilon = \frac{Y_o}{2H'}\ln\left(1+\frac{3\tau^2}{Y_o^2}\right)+\frac{Y_o}{E} \tag{C.1}$$

$$\gamma = \frac{3}{H'}\left[\tau-\frac{Y_o}{\sqrt{3}}\tan^{-1}\left(\frac{\tau\sqrt{3}}{Y_o}\right)\right]+\frac{\tau}{G} \tag{C.2}$$

where Y_o is the yield stress in tension, E is Young's Modulus, H' is the plastic modulus, and G is the elastic shear modulus for $\nu = 0.3$.

Since a single material point is sufficient to model the problem, only one Q8 element in a single layer is necessary for a FRANC2D/L model. Figure C.2 shows the material properties used, and Figure C.3 shows the applied boundary conditions. The loads were applied in two separate load cases. Then load factors were used to scale the loads. The tensile load factor was set to 26.25 and the shear load factor to 0.0, then equilibrium was established. Next the tensile load factor was set to 0.0 (load held constant, no increment) and the shear load factor was slowly incremented to apply the twist under constant tension.

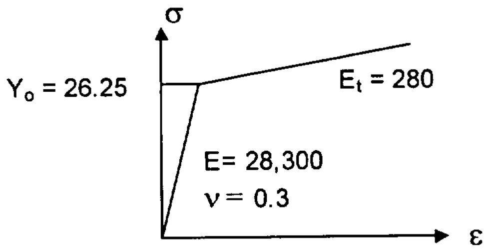

Figure C.2: Material properties for the tension torsion example.

Figure C.4 shows the exact strain path and FRANC2D/L results for selected applied loads. The results show that the FRANC2D/L plasticity model is capable of accurate results.

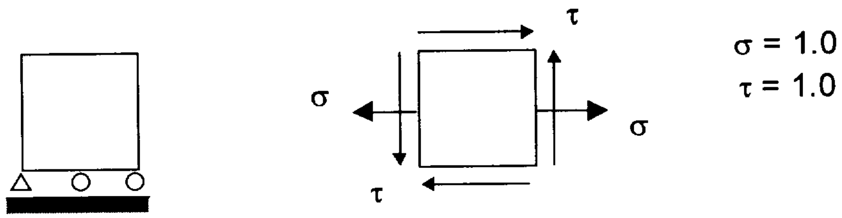

Figure C.3: Fixity and loading conditions. Shear loads and axial loads are in different load cases to facilitate non-proportional loading.

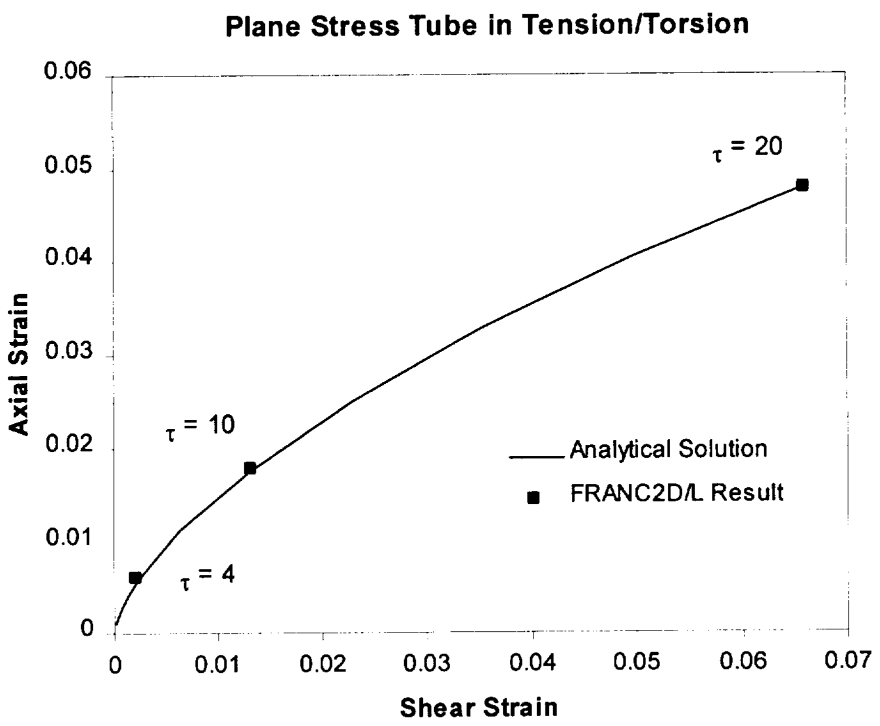

Figure C.4: Comparison of selected FRANC2D/L results with exact results.

Appendix D

Elastic-Plastic Validation

Modeling elastic-plastic fracture requires an accurate description of strains in the process zone. Newman et al. (1992) compared elastic-plastic finite element analysis results with experimental results for a blunt-notch specimen. These specimens were similar to M(T) specimens, except that a small hole was drilled at the end of the saw cut, and the holes polished to help prevent premature fracture.

Figure D.1 shows the geometry of the specimen, and Figure D.2 shows the finite element idealization. Only ¼ of the specimen was modeled by using symmetry along the horizontal and vertical center-lines of the specimen. Displacement control boundary conditions were applied along the top edge of the model. Table D.1 contains the analysis material properties for 2024-T3 aluminum, and Table D.2 contains the multi-linear stress-strain curve used in the von Mises yield model.

Table D.1: Analysis Material Properties

Young's Modulus	10350 Ksi
Poisson's Ratio	0.3
Thickness	0.09 inch
Yield Stress	50 Ksi

Figure D.3 is a contour plot of the von Mises stress near the failure load. The plot shows the extent of yielding in the model. Figure D.4 shows the applied stress against notch-root displacement for the test and for the FRANC2D/L simulation. Displacements were measured at both notch roots using displacement gages. The FRANC2D/L results show excellent agreement with the experimental measurements, indicating that the small strain software is capable of simulating the relatively large-scale plasticity experienced by the test specimen.

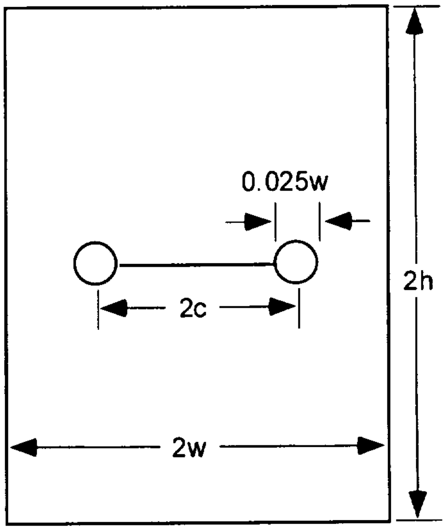

Figure D.1: Schematic of blunt notch specimen (w = 10 in, h = 12 in, c = 1.875 in).

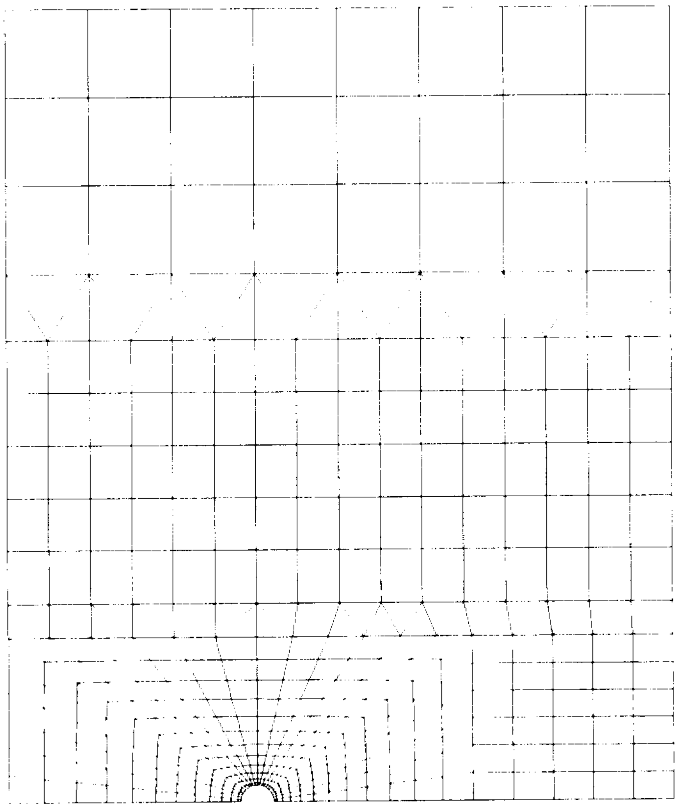

Figure D.2: Finite element idealization of blunt notch specimen.

Table D.2: Uniaxial stress-strain curve.

Stress (Ksi)	Strain
0.0	0.0
50.0	0.00483
56.5	0.015
62.5	0.04
68.5	0.1
71.0	0.16
1.0	0.2

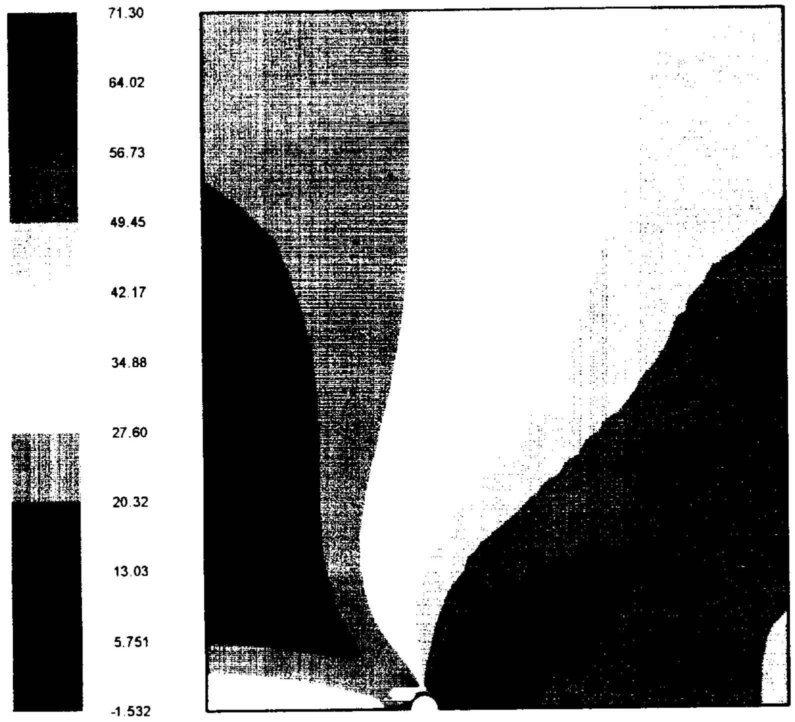

Figure D.3: Contour plot of von Mises stress (ksi).

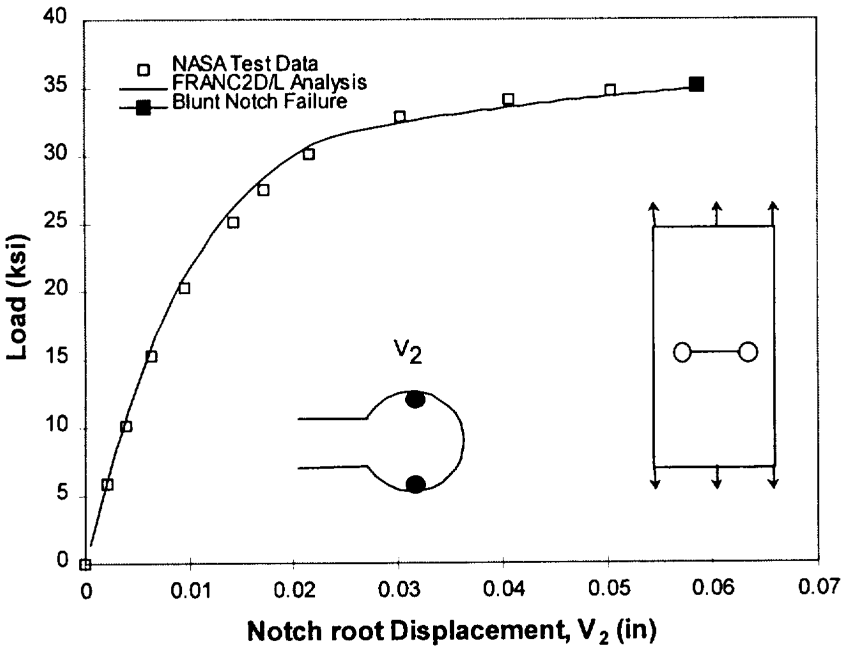

Figure D.4: Blunt notch configuration and results.